

HEATING AND COOLING MECHANISMS FOR THE THERMAL MOTION OF  
AN OPTICALLY LEVITATED NANOPARTICLE

A Dissertation

Submitted to the Faculty

of

Purdue University

by

Troy Seberson

In Partial Fulfillment of the

Requirements for the Degree

of

Doctor of Philosophy

December 2020

Purdue University

West Lafayette, Indiana

**THE PURDUE UNIVERSITY GRADUATE SCHOOL**  
**STATEMENT OF DISSERTATION APPROVAL**

Dr. Francis Robicheaux, Chair

Department of Physics

Dr. Qi Zhou

Department of Physics

Dr. Laura Pyrak-Nolte

Department of Physics

Dr. Tongcang Li

Department of Physics

**Approved by:**

Dr. John Finley

Head of the Department of Physics

## ACKNOWLEDGMENTS

I would like to express my deep gratitude to Professor Robicheaux, my advisor, for bringing me into his circle and mentoring me. The skills, wisdom, and guidance he has given me has helped shape me into what I am today.

I also thank Professor Pyrak-Nolte and Professor Zhou for being my thesis committee members. A special thanks to my committee member and co-advisor, Professor Li, who I have been blessed to learn from as well.

Thank you to my colleagues and collaborators Peng Ju, Jaehoon Bang, Jonghoon Ahn, Zhujing Xu, Xingyu Gao, Xiao Wang, Akilesh Venkatesh, Hyunwoo Lee, and Zhong Wan. I am grateful for the many friends I have my made during this journey; a treasured appreciation for Marius Radu, Srinath Shiv Kumar, Shivam Gupta, Tyler Sutherland, David Blasing, Nicole Sykora, Xiaoling Wang, Alia Azmat, Adithan Kathirgamaraju, Sara Metti, and James Nakamura. Thanks to my friends and family for their enduring love and support, specifically Charles Seberon, Sherry Seberon, Yani Tan, Ben Enger, and Lars Gjersvik.

## TABLE OF CONTENTS

	Page
LIST OF TABLES . . . . .	vi
LIST OF FIGURES . . . . .	vii
ABSTRACT . . . . .	xiii
1. INTRODUCTION . . . . .	1
2. LIGHT INTERACTION WITH DIELECTRICS . . . . .	5
2.1 The Lippmann-Schwinger Equation . . . . .	5
2.2 Rayleigh scattering . . . . .	7
2.3 Rayleigh-Gans Scattering . . . . .	10
2.4 Scattered fields in the far-zone . . . . .	11
2.5 Interaction energy and forces . . . . .	13
3. TRANSLATIONAL MOTION . . . . .	15
3.1 The Gradient Force . . . . .	15
3.2 The Scattering Force . . . . .	17
3.3 Measuring the particle displacement . . . . .	18
4. ROTATIONAL MOTION . . . . .	23
4.1 Classical dynamics . . . . .	24
4.2 Quantum dynamics . . . . .	30
4.3 Measuring the particle orientation . . . . .	34
5. DAMPING AND NOISE . . . . .	39
5.1 Gas collisions . . . . .	39
5.2 Translational shot noise . . . . .	40
5.2.1 Semi-classical Rayleigh shot noise . . . . .	41
5.2.2 Rayleigh shot noise heating rate . . . . .	42
5.2.3 Quantum Rayleigh shot noise heating rate . . . . .	45
5.2.4 Mie scattering . . . . .	46
5.2.5 Focused Gaussian Beam . . . . .	48
5.3 Rotational Rayleigh shot noise . . . . .	53
6. METHODS OF COOLING THE MOTION . . . . .	57
6.1 Parametric feedback cooling the rotational motion of nanodumbbells . . . . .	58
6.1.1 Linear polarization . . . . .	60
6.1.2 Elliptical polarization . . . . .	64
6.1.3 Experimental signatures . . . . .	68

	Page
6.1.4 Discussion of heating and noise . . . . .	69
6.1.5 Conclusion . . . . .	70
6.2 Experimentally cooling the rotational motion of nanodumbbells . . . . .	71
6.3 Sympathetically cooling a magnetic nanoparticle . . . . .	76
6.3.1 Toy model . . . . .	76
6.3.2 Model of the system . . . . .	78
6.3.3 Simulations of the full system . . . . .	85
6.3.4 Conclusion . . . . .	90
6.4 Dynamics and cooling of levitated disks . . . . .	91
6.4.1 Approximate Analytical Potential Energy . . . . .	93
6.4.2 Numerical Evaluation of the Forces and Torques . . . . .	99
6.4.3 Dynamics . . . . .	107
6.4.4 Conclusion . . . . .	110
7. SUMMARY AND OUTLOOK . . . . .	112
REFERENCES . . . . .	116
PUBLICATIONS . . . . .	128

## LIST OF TABLES

Table	Page
6.1 Relevant properties of the three species of atoms and their Doppler parameters. From left to right: the atom mass, magnetic moment, decay rate, Doppler line, and Doppler temperature. . . . .	85
6.2 Frequencies for a silica disks of radius $a = 200$ nm and thickness $T = \lambda/(40n)$ for two beam waists $w_0 = 2, 3 \mu\text{m}$ . The disk has dimensions that are reduced by a factor of ten from the $a = 2 \mu\text{m}$ , $T = \lambda/(4n)$ disks. A fixed total power of 100 mW is used for the calculations. The number of points used to compose the disk was $N = 37488$ and the thickness of the disk was 4 points. . . . .	102

## LIST OF FIGURES

Figure	Page
3.1 (a) Picture of an actual silica nanosphere trapped in the focus of a laser beam. Image taken from [44]. (b) Model of the system. A nanosphere (blue) is trapped and oscillates about the focus of a Gaussian laser beam (red) traveling in the $z$ -direction and polarized in the $x$ -direction (yellow).	15
3.2 Illustration of the measurement procedure. The scattered light (yellow) from the nanoparticle (blue) is homodyned with the laser beam and the resulting signal is incident upon a quadrant photodetector. A measurement of the displacement $x_0$ from the focus is performed by subtracting the sections (A+B)-(C+D) while for a measurement in the $y$ direction (A+C)-(B+D).	19
3.3 (a) Time trace of the experimentally measured position observing the oscillatory behavior. Picture taken from [23]. (b) Power spectral density of measured $x, y, z$ positions from Ref. [56].	21
4.1 Scanning electron microscope image of actual silica nanodumbbells used in the experiments of Ref. [56]. Photo credit to the same reference.	23
4.2 (a) A nanodumbbell with center of mass confined to the origin is allowed to rotate. The particle has the lowest energy when its long axis ( $z'''$ -axis) aligns with the laser's electric field polarized in the lab frame $x$ -direction. (b) The definition of the Euler angles $\alpha, \beta, \gamma$ shown in the $z$ - $y'$ - $z''$ convention. For small angle rotations, the coordinate $\alpha = 0 + \xi$ describes rotations near the lab frame $x$ -axis in the $x$ - $y$ plane and $\beta = \pi/2 - \eta$ describes rotations near the lab frame $x$ -axis in the $x$ - $z$ plane. The coordinate $\gamma$ describes rotations about the $z'' = z'''$ axis with $\gamma(t) \approx \omega_3 t$ . For visual clarity, the $x'', y'', x''', y'''$ axes have been omitted from the figure.	25
4.3 Trajectory of the nanoparticle's $z'''$ -axis, projected on the lab frame $y$ - $z$ plane found by simulating the full equations of motion and using linear polarization. Here, $Z/2R = \cos(\beta)$ , $Y/2R = \sin(\beta) \sin(\alpha)$ define the location of the $z'''$ -axis; in the small angle limit $Z/2R \approx \eta$ , $Y/2R \approx \xi$ . The particle's long axis moves in two joint motions, one describing libration and the other describing precession about the polarization axis.	30

Figure	Page	
4.4	Illustration of the measurement procedure for measuring the orientation. A Gaussian beam is incident upon a symmetric-top particle at an angle $\alpha$ with respect to the polarization axis. The scattered light and outgoing laser light interfere to produce a total electric field $E_{\text{total}}$ . The signal then enters a polarized beam splitter where it is split into two polarizations $E_+$ and $E_-$ . The two signals exiting the beam splitter are incident upon their respective detectors and are subtracted from one another to obtain a signal proportional to the angle $\alpha$ . . . . .	35
4.5	Power spectral density of a nanodumbbell's measured position and orientation (labeled <i>Tor</i> , standing for torsional motion, in the figure) [56]. . . . .	37
5.1	Shot noise heating rate for each degree of freedom relative to the rate in the Rayleigh limit for diamond at laser wavelength (a) $\lambda = 1550$ nm (b) $\lambda = 1064$ nm (c) $\lambda = 532$ nm and silica at wavelength (d) $\lambda = 1550$ nm (e) $\lambda = 1064$ nm (f) $\lambda = 532$ nm. For each plot, the relative heating rate is shown for the $x$ (blue dotted line), $y$ (orange dashed line), and $z$ (green dot-dashed line) degree of freedom, as well as the total heating rate (red solid line). Here, the incident plane wave is polarized in the $x$ and traveling in the $z$ direction. The relative heating rate is reduced in each degree of freedom for silica. The non-linear behavior of Mie scattering can be seen near $r = 200$ nm in diamond with a resonance occurring at $\lambda = 1064$ nm. The index of refraction for silica is $n_s = 1.45$ for $\lambda = 1550$ nm and $\lambda = 1064$ nm while $n_s = 1.46$ for $\lambda = 532$ nm. The index of refraction for diamond is $n_d = 2.39$ for $\lambda = 1550$ nm and $\lambda = 1064$ nm while $n_d = 2.425$ for $\lambda = 532$ nm. . . . .	43
5.2	Comparison of the total shot noise heating rate using Mie and Rayleigh scattering for a silica nanoparticle ( $n_s = 1.46$ for $\lambda = 532$ nm) under plane wave illumination. For radii $r < 50$ nm the Mie calculation shares the same $r^3$ dependence as the Rayleigh expression. For larger radii, the non-linear Mie calculation yields significantly less total heating. . . . .	47
5.3	Contour surface plots of the shot noise heating rate for each degree of freedom relative to the rate in the Rayleigh limit for silica ( $n = 1.45$ ) at laser wavelengths $\lambda = 1550$ nm (top row) and $\lambda = 1064$ nm (bottom row). The heating rates for each degree of freedom ( $x, y, z$ ) are shown in the first, second, and third column respectively. The colorbar on the far right is a scale for the ratio between the numerically calculated shot noise heating, Eq. (5.24), and the Rayleigh expression for that degree of freedom. As expected for small NA and radius the shot noise in each degree of freedom agrees well with the Rayleigh expression. . . . .	50

Figure	Page	
6.1	(a) A nanodumbbell with center of mass confined to the origin is allowed to rotate. The particle has the lowest energy when its long axis ( $z'''$ -axis) aligns with the laser's electric field polarized in the lab frame $x$ -direction. (b) The definition of the Euler angles $\alpha$ , $\beta$ , $\gamma$ shown in the $z$ - $y'$ - $z''$ convention. For small angle rotations, the coordinate $\alpha = 0 + \xi$ describes rotations near the lab frame $x$ -axis in the $x$ - $y$ plane and $\beta = \pi/2 - \eta$ describes rotations near the lab frame $x$ -axis in the $x$ - $z$ plane. The coordinate $\gamma$ describes rotations about the $z'' = z'''$ axis with $\gamma(t) \approx \omega_3 t$ . For visual clarity, the $x''$ , $y''$ , $x'''$ , $y'''$ axes have been omitted from the figure. . . . .	59
6.2	Trajectory of the nanoparticle's $z'''$ -axis, projected on the lab frame $y$ - $z$ plane found by simulating the full equations of motion and using linear polarization. Here, $Z/2R = \cos(\beta)$ , $Y/2R = \sin(\beta) \sin(\alpha)$ define the location of the $z'''$ -axis; in the small angle limit $Z/2R \approx \eta$ , $Y/2R \approx \xi$ . (a) The particle's long axis moves in two joint motions, one describing libration and the other describing precession about the polarization axis. (b) Final trajectory of the long axis after parametric feedback cooling. The motion has reduced to pure precession. . . . .	60
6.3	(a) Energy of the four quadratic degrees of freedom versus time under parametric feedback cooling during a single trajectory. The energy plateaus to a nonzero value as the nanoparticle circles the polarization axis. (b) Distribution of initial energies used before parametric feedback cooling. The distribution follows the blue line, a Maxwell-Boltzmann distribution with four quadratic degrees of freedom at a temperature of 300 K. (c) Distribution of energies following parametric feedback cooling with linear polarization. The distribution has a mean of 312 K and is similar to the blue line, a Maxwell-Boltzmann distribution with two quadratic degrees of freedom at a temperature of 300 K. The final energies are taken as the last data point in runs similar to that of (a). (d) Final energy distribution of the nanoparticle following feedback cooling with elliptical polarization for $\theta = \frac{4\pi}{32}$ . Each distribution in this figure is composed of 12,000 runs implemented with a cooling strength $\chi = 10^7$ s/m <sup>2</sup> . . . . .	62

Figure	Page
<p>6.4 Plots showing the dependence of the cooling strength, <math>\chi</math>, in (a) and the frequency separation of <math>\omega_\eta</math> and <math>\omega_\xi</math> in (b) on the cooling rate, <math>\langle P \rangle_{\xi\dot{\xi}+\eta\dot{\eta}}</math>. (a) Intermittently increasing the cooling strength <math>\chi</math> during a single cooling process for a fixed electric field strength (<math>\theta = \frac{4\pi}{32}</math>). Each dip corresponds to an abrupt increase in the value of <math>\chi</math>. At <math>t = 0</math>, the cooling process starts with <math>\chi = 10^7</math> s/m<sup>2</sup>. Beginning with <math>t = 3</math> ms, <math>\chi</math> is increased every 1 ms by a factor of ten, ending with <math>10^{12}</math> s/m<sup>2</sup>. (b) Average energy after feedback cooling versus <math>\theta</math> showing the dependence of the frequency separation between <math>\omega_\eta</math> and <math>\omega_\xi</math> on the cooling rate <math>\langle P \rangle_{\xi\dot{\xi}+\eta\dot{\eta}}</math>. The points are averages of 1000 calculated energies following feedback cooling for a fixed simulation time of 80 ms and cooling strength <math>\chi = 10^7</math> s/m<sup>2</sup>. . . . .</p>	67
<p>6.5 Power spectral densities of a <math>p_y</math> measurement before and after feedback cooling for (a) linear polarization and (b) elliptical polarization. Feedback cooling using linear polarization eliminates one peak, shifting the remaining peak to a normal mode frequency and reducing the motion to pure precession. Feedback cooling under elliptical polarization reduces both peaks in magnitude, and shifts them toward the normal mode frequencies found in the small angle approximation. . . . .</p>	68
<p>6.6 Illustration of the experimental setup in Ref. [77] in (a) and the power spectral densities obtained for the <math>x, y, z, \alpha, \beta</math> degrees of freedom of a dumbbell with radius 85 nm. In the setup, there are a total of 4 lasers. The power with the greatest intensity, the trapping laser (red), is focused by a NA=0.85 objective, traveling in the <math>z</math> direction and polarized in the <math>x</math> direction. The remaining 3 lasers are cooling lasers (green and orange). The cooling laser traveling in the <math>x</math> and polarized in the <math>y</math> direction provides force feedback on the translational <math>x</math> degree of freedom. The cooling lasers traveling in the <math>y</math> and <math>-z</math> directions are meant to cool the <math>y</math> and <math>z</math> degrees of freedom, respectively. The <math>y</math> and <math>z</math> cooling lasers simultaneously cool the <math>\beta</math> and <math>\alpha</math> degrees of freedom, respectively. This is achieved by tilting the polarizations of each rotational cooling laser roughly 10 degrees with respect to the equilibrium axis of <math>\beta</math> and <math>\alpha</math>, the <math>x</math> axis. The <math>y</math> and <math>z</math> cooling lasers power is then modulated at two frequencies, one translational and one rotational. For the power spectral densities in (b), the two normal modes of <math>\alpha</math> and <math>\beta</math> can be seen with wide distributions, corresponding to continuously fluctuating <math>\omega_3</math> due to scattering with the gas molecules. . . . .</p>	72

Figure	Page
6.7 (a)(b) Experimental power spectral densities of the $\alpha$ and $\beta$ degrees of freedom following the cooling procedure for a $R = 85$ nm dumbbell. The PSD's are snapshots at two different times, showing how the fluctuation of $\omega_3$ affects the exact position of the normal modes at any given time. (c)(d) Simulation PSD's using the parameters in the experiment. From (c), the coupling for (a) was found to be $\omega_c/2\pi = 17$ kHz and from (d), the value of $\omega_c/2\pi$ is 115 kHz. . . . .	73
6.8 (a) Normalized frequency fluctuations $\omega_y(t)/\langle\omega_y(t)\rangle$ , $\omega_+(t)/\langle(\omega_+(t)+\omega_-(t))/2\rangle$ , $\omega_-(t)/\langle(\omega_+(t) + \omega_-(t))/2\rangle$ at low pressure $3 \times 10^{-3}$ Torr showing stable translational motion and large fluctuations for the rotational coordinates. Note the anti-correlation between the $\omega_{\pm}$ modes. (b) Normalized frequency fluctuations at high pressure, 5 Torr. (c) Correlations between the translational, rotranslational, and rotational DOF. The normal modes of the orientational DOF are anti-correlated due to the coupling with the spin about the nanodumbbell's symmetry axis. . . . .	74
6.9 Power spectral densities of the orientational degrees of freedom, (a) $\alpha$ and (b) $\beta$ . The PSD before cooling is in blue, the PSD after cooling is in red, and the noise floor in green. In (a) the broad peak at 300 K is reduced to the two normal mode peaks with an estimated temperature of 10 K. In (b) the $\beta$ DOF has been cooled to a point where the signal is below the noise floor. . . . .	75
6.10 (a) Energy versus time of particle 1 and 2 while on resonance. (b) Energy versus time for 1 particle in trap 1 coupled to 4 non-interacting particles in trap 2. As Eq. (6.27) predicts, the exchange frequency increases by $\sqrt{N} = 2$ compared to (a). . . . .	78
6.11 Illustration of the proposed model. A ferromagnetic nanosphere is trapped at the focus of a Gaussian beam. The oscillation frequency for the nanoparticle in the $y$ direction is $\omega_p$ . A cloud of $N$ atoms a distance $y_0$ away are trapped in a separate, far red-detuned dipole trap oscillating at frequency $\omega_a$ in the $y$ direction. An external magnetic field $\vec{B}_{\text{ext}}$ orients the magnetic moments of the nanoparticle and atoms. . . . .	79
6.12 (a) Nanoparticle cooling rate versus the number of atoms in the atom cloud. The rate is linearly proportional to the number of atoms and increases for species with larger magnetic moment $\mu_a$ as predicted by Eq. (3.11). Only atom numbers that produced a statistically significant cooling rate were plotted. (b) Kinetic energy of the nanoparticle versus time for $N = 10^4$ dysprosium atoms and fit to a decaying exponential. From the fit, $\gamma$ was extracted and used to plot (a). . . . .	87

Figure	Page
6.13 Coordinate system in the lab frame $(x, y, z)$ and the particle frame $(x''', y''', z''')$ . The disk's symmetry axis is aligned with the particle frame $z'''$ axis. The disk's center of mass as measured from the lab frame $\vec{r}_0$ is shown in red. The location to a point on the thin disk is given by the polar coordinates $(\rho', \phi')$ in the particle frame which are shown in purple. . . . .	94
6.14 Frequencies obtained using the DDA for silica disks ( $n=1.45$ ) of radius $a = 2 \mu\text{m}$ and thickness $T = \lambda/(4n)$ for varying beam waist. Frequencies are shown for the (a) $x$ , (b) $y$ and $z$ , (c) $\theta_y$ and $\theta_z$ degrees of freedom and the coupling constants in (d). A fixed total power of 100 mW is used for the calculations. For each calculation the disk was composed of $N = 299744$ points with a thickness of 8 points. . . . .	103
6.15 Frequencies obtained using the DDA for silicon nitride disks ( $n=2.0$ ) of radius $a = 2 \mu\text{m}$ and thickness $T = \lambda/(4n)$ for varying beam waist. Frequencies are shown for the (a) $x$ , (b) $y$ and $z$ , (c) $\theta_y$ and $\theta_z$ degrees of freedom and the coupling constants in (d). A fixed total power of 100 mW is used for the calculations. For each calculation the disk was composed of $N = 569984$ points with a thickness of 8 points. . . . .	104
6.16 Frequencies obtained for a $a = 2 \mu\text{m}$ silica disk using DDA for varying number of points that the disk was composed of relative to the frequency obtained using 299744 points, $\omega_{i,0}$ . The legend describes the various frequencies for the $x, y, z, \theta_y, \theta_z$ degrees of freedom as well as the $\omega_1, \omega_2$ coupling frequencies. The data points along the $x$ -axis are 4680, 15804, 37488, and 299744 points. Comparing the left and rightmost data points in the figure shows that using 64 times more points changes the frequencies by less than 2%. . . . .	106
6.17 Example trajectories of the (a) $\theta_y$ , (b) $\theta_z$ , and (c) $x$ degrees of freedom as well as (d) the power spectral density of the axial motion ( $x$ ) for a $a = 2 \mu\text{m}$ silica disk in a $w_0 = 3 \mu\text{m}$ waist trap. The influence of the second order coupling term produces several amplitude modulations at different frequencies, but the disk remains stable. The frequencies of modulation in the $x$ degree of freedom can be seen in the power spectral density. Note that the rotational amplitudes remain in the $\sim \text{mrad}$ range, justifying the small angle approximation. . . . .	108

## ABSTRACT

Seberson, Troy PhD, Purdue University, December 2020. Heating and Cooling Mechanisms for the Thermal Motion of an Optically Levitated Nanoparticle . Major Professor: Dr. Francis Robicheaux.

Bridging the gap between the classical and quantum regimes has consequences not only for fundamental tests of quantum theory, but for the relation between quantum mechanics and gravity. The field of levito-dynamics provides a promising platform for testing the hypotheses of the works investigating these ideas. By manipulating a macroscopic particle's motion to the scale of its ground state wavefunction, levito-dynamics offers insight into the macroscopic-quantum regime.

Ardent and promising research has brought the field of levito-dynamics to a state in which these tests are available. Recent work has brought a mesoscopic particle's motion to near the ground state. Several factors of decoherence are limiting efficient testing of these fundamental theories which implies the need for alternative strategies for achieving the same goal. This thesis is concerned with investigating alternative methods that may enable a mesoscopic particle to reach the quantum regime.

In this thesis, three theoretical proposals are studied as a means for a mesoscopic particle to reach the quantum regime as well as a detailed study into one of the most important factors of heating and decoherence for optical trapping. The first study of cooling a particle's motion highlights that the rotational degrees of freedom of a levitated symmetric-top particle leads to large harmonic frequencies compared to the translational motion, offering a more accessible ground state temperature after feedback cooling is applied. An analysis of a recent experiment under similar conditions is compared with the theoretical findings and found to be consistent.

The second method of cooling takes advantage of the decades long knowledge of atom trapping and cooling. By coupling a spin-polarized, continuously Doppler

cooled atomic gas to a magnetic nanoparticle through the dipole-dipole interaction, motional energy is able to be removed from the nanoparticle. Through this method, the particle is able to reach near its quantum ground state provided the atoms are at a temperature below the nanoparticle ground state temperature and the atom number is sufficiently large.

The final investigation presents the dynamics of an optically levitated dielectric disk in a Gaussian standing wave. Though few studies have been performed on disks both theoretically and experimentally, our findings show that the stable couplings between the translational and rotational degrees of freedom offer a possibility for cooling several degrees of freedom simultaneously by actively cooling a single degree of freedom.

## 1. INTRODUCTION

Does quantum mechanics apply on macroscopic scales? As size of the system increases, quantum phenomena seem to disappear. While quantum behavior is routinely observed for atoms, molecules, and in nanostructures at very low temperatures, everyday macroscopic objects that surround us are observed to obey classical physics. Yet there is no fundamental reason that larger objects should not also obey quantum mechanics. The Schrodinger equation places no bounds on the size of the system under study. The Heisenberg uncertainty relation is also not implausibly violated. With little experimental verification of this reality, perhaps there is some scaling limit beyond which quantum mechanics does not apply.

Answering this question would have several implications in the fields of physics, such as potentially bridging the gap between general relativity and quantum mechanics [1,2]. What gravitational field is generated by an object in a spatial superposition? Since everyday objects appear to always be in one state, manipulating larger quantum mechanical objects would help further our understanding of the universe and how matter and energy interact [3-5]. Do the smallest particles live in a world with a different set of laws, or can we identify a classical-to-quantum transition in order to solve 'the measurement problem'?

These ideas are being put to the test at the forefront of the research performed in the field of levitated optomechanics (more generally, levito-dynamics), where mesoscopic particles are levitated and their motion manipulated by external forces such as light. In its simplest form, mesoscopic particles are levitated and harmonically trapped in all motional degrees of freedom. Energy can subsequently be removed from the motion in order to bring the oscillator to its motional ground state. Evidence for the generation of a superposition of spatial harmonic oscillator states would

provide a platform for testing the outstanding questions related to macroscopic quantum mechanics and gravity's relation to quantum mechanics [6–12].

Other micromechanical systems in optomechanics such as microchip resonators offer similar applications [13] and have been able to attain low occupation numbers below  $\bar{n} = 1$  [14, 15] due to their GHz resonance frequencies and strong coupling to light. However, these systems require cryogenic cooling or phononic band gaps to suppress their intrinsic decoherence and improve quality factors since they are directly coupled to their environment [16]. Optically levitated nanoparticles are isolated from rigid structures, eliminating this source of decoherence, and can achieve quality factors  $Q > 10^9$  [17].

Three dimensional trapping of a 5  $\mu\text{m}$  glass particle in air was first demonstrated in 1997 using optical tweezers [18]. However, the field of levitated optomechanics began growing rapidly following 2010 when new research gave insight that trapped particles follow Brownian motion and the equipartition theorem. In the same year, nanoparticles were trapped and coupled to Fabry Perot cavities, and their motion was manipulated for cooling [19–25]. The trapping of particles in optical tweezers, cavities, and ion traps is now well understood and readily performed experimentally [26].

The next feat is to perfect the cooling mechanism(s) that brings a mesoscopic particle to its motional quantum ground state. The most widely used and successful methods thus far are cold damping (force feedback), parametric feedback cooling, and cooling by coherent scattering. Force and parametric feedback cooling requires precise measurement of the particle's motion in order to provide feedback to the cooling system procedure and is systematically limited by noise [27]. Nonetheless, force feedback in an electrical-optical hybrid trap has realized a mean occupation number of  $\bar{n} = 4$  [28]. While current research aims to reduce the level of noise [29, 30], cooling by coherent scattering has proven to be the most effective method [31–33]. Utilizing an optical tweezer to place a silica nanosphere at the location of maximal coupling to an optical cavity ( $\lambda/8$ ), cooling by coherent scattering has recently been shown (2020) to bring the particle from room temperature to near its ground state,

$\bar{n} < 1$ , in one degree of freedom [34]. Reaching lower temperatures is currently limited by the scattering of gas molecules in the vacuum chamber, and is expected to be reduced in order to perform quantum experiments on the macroscopic particle [35–37].

This thesis is concerned with providing alternative cooling schemes for cooling a levitated nanoparticle’s motion as well as giving more detailed insight into cooling impediments. Though ground state cooling has been achieved in one dimension, the same milestone has yet to be reached in two or more degrees of freedom. Alternative cooling schemes pave the way for potentially lower occupation numbers, cooling in several degrees of freedom, noise reduction/elimination, easier implementation with available hardware, among other advantages. A levitated particle also has use as a force, torque, and charge sensor for various applications such as detection of gravitational waves, measuring fractional charges in bulk matter, the Casimir effect, and vacuum friction [38–48]. It is conducive for the particle’s motion to be below room temperature for most, but not all [48], precise sensing applications.

This thesis is organized as follows. In Ch. 2, the fundamentals associated with a dielectric particle’s interaction with light is presented. The concepts and equations are some of the building blocks of levitated optomechanics and will be of use in later chapters.

Chapter 3 provides the basic formulation for a dielectric particle’s translational dynamics in the Rayleigh regime. The conservative optical gradient force, required for trapping, and the dissipative scattering force due to radiation pressure are calculated. The procedure for measuring the particle’s motion in real time is also provided.

Chapter 4 is concerned with the rotational dynamics of a rigid, symmetric-top Rayleigh particle. Similar to Ch. 3, the process for measuring the rotational degrees of freedom is also outlined.

Although levitated particles are not in direct physical contact with their environment, they are not immune to decoherence and heating. The main sources of noise and heating in a levitated optomechanical setup, gas collisions and laser shot-noise, are discussed in Ch. 5.

Four different methods for cooling the motion of a mesoscopic dielectric particle are described in Ch. 6. Three theoretical proposals for cooling both translational and rotational dynamics are provided and an analysis of one experiment that cooled the rotational and translational motion simultaneously. The first theoretical method involves cooling the rotational degrees of freedom of a symmetric-top particle in the Rayleigh regime using parametric feedback cooling. The second investigates sympathetic cooling a magnetic nanoparticle via magnetic interaction with a cold, spin-polarized atomic gas. The third studies the dynamics of disks outside of the Rayleigh regime and briefly shows that ro-translational couplings offer the possibility of sympathetic cooling several degrees of freedom. The experimental section discusses the results found in an investigation that cooled three translational and two rotational degrees of freedom simultaneously using the content found in this thesis.

Lastly, Ch. 7 gives a summary and outlook for the future of levito-dynamics.

## 2. LIGHT INTERACTION WITH DIELECTRICS

This chapter is dedicated to outlining the fundamentals and underpinnings associated with a dielectric interaction with an electromagnetic field. There are different approaches which one could take to reach the conclusions in this chapter and here a formal scattering approach will be taken. Since levitated optomechanics is primarily concerned with single frequency laser beams, in what follows all electric and magnetic fields are assumed to have a time dependence of the form  $\vec{\psi}(r, t) = \vec{\psi}(r) \exp(-i\omega t)$  where  $\omega = ck$ ,  $c$  is the speed of light, and  $k = 2\pi/\lambda$  is the wavenumber. Throughout this thesis,  $\epsilon_0$  is the permittivity of free space. For this chapter non-magnetic, linear dielectrics are assumed so that the electric responses will be the main interest. Lastly, for this chapter matrices and tensors will be represented by bold symbols,  $\mathbf{A}$ , and vectors will be represented with top arrows,  $\vec{A}$ .

### 2.1 The Lippmann-Schwinger Equation

Consider an electric field  $\vec{E}_{\text{inc}}(r)$  traveling in the  $\vec{k}$  direction incident upon a dielectric particle of arbitrary shape located in vacuum or air,  $\epsilon = 1$ . The particle is described by a dielectric tensor  $\epsilon$  which in general is dependent on the location inside the particle  $\vec{r}$ . The solution for the resultant electric field due to scattering from the particle  $\vec{E}(\vec{r}) = \vec{E}_{\text{inc}}(\vec{r}) + \vec{E}_{\text{scatt}}(\vec{r})$  is governed by Maxwell's equations. As the dielectric is considered to contain no free charges the solution at a point in space  $\vec{r} = r\hat{r}$  is given by the Helmholtz equation

$$(\nabla^2 - k^2\epsilon) \vec{E}(\vec{r}) = 0. \quad (2.1)$$

The incident field is already known to obey Maxwell's equations both in the particle and in the background with permittivity  $\epsilon = 1$

$$(\nabla^2 - k^2) \vec{E}_{\text{inc}}(\vec{r}) = 0, \quad (2.2)$$

and the goal is to find a solution for the scattered wave  $\vec{E}_{\text{scatt}}(\vec{r})$ . Writing Eq. (2.1) in terms of the susceptibility tensor  $\chi = (\epsilon - \mathbf{1})$ ,

$$(\nabla^2 - k^2) \vec{E}_{\text{scatt}}(\vec{r}) = k^2 \chi \vec{E}(\vec{r}). \quad (2.3)$$

With the aid of the dyadic Greens function for electric dipoles  $\mathbf{G}(\vec{r}, \vec{r}')$  satisfying

$$(\nabla^2 - k^2) \mathbf{G}(\vec{r}, \vec{r}') = \mathbf{1} \delta^3(\vec{r} - \vec{r}'), \quad (2.4)$$

with  $\delta^3(\vec{r} - \vec{r}')$  the delta function, the scattered field is found to be

$$\vec{E}_{\text{scatt}}(\vec{r}) = k^2 \int d^3 r' \mathbf{G}(\vec{r}, \vec{r}') \chi \vec{E}(\vec{r}'), \quad (2.5)$$

where the integration is taken over the volume of the dielectric. Physically Eq. (2.4) and its solution describes the radiated field at  $\vec{r}$  due to three orthogonal point dipole sources located at  $\vec{r}'$ . Equation (2.5) then describes the scattered field due to the point dipoles that make up the dielectric. The solution for the outgoing Green's function for point dipoles can be shown to be [49, 50]

$$\mathbf{G}(\vec{r}, \vec{r}') = \left( \mathbf{1} + \frac{1}{k^2} \nabla \nabla \right) \frac{e^{ik|\vec{r}-\vec{r}'|}}{4\pi|\vec{r}-\vec{r}'|} \quad (2.6)$$

$$= \left\{ \left( \frac{3}{k^2|\vec{R}|^2} - \frac{3i}{2k|\vec{R}|} - 1 \right) \hat{R}\hat{R} + \left( 1 + \frac{i}{k|\vec{R}|} - \frac{1}{k^2|\vec{R}|^2} \right) \mathbf{1} \right\} \frac{e^{ik|\vec{R}|}}{4\pi|\vec{R}|}, \quad (2.7)$$

where  $\nabla$  is evaluated with respect to  $r$  and  $\vec{R} = \vec{r} - \vec{r}' = |\vec{R}|\hat{R}$ . The scattered field is

$$\vec{E}_{\text{scatt}}(\vec{r}) = \frac{k^2}{4\pi} \left( \mathbf{1} + \frac{1}{k^2} \nabla \nabla \right) \int d^3 r' \frac{e^{ik|\vec{R}|}}{|\vec{R}|} \chi \vec{E}(\vec{r}'), \quad (2.8)$$

giving the total field as

$$\vec{E}(\vec{r}) = \vec{E}_{\text{inc}}(\vec{r}) + \frac{k^2}{4\pi\epsilon_0} \left( \mathbf{1} + \frac{1}{k^2} \nabla \nabla \right) \int d^3 r' \frac{e^{ik|\vec{R}|}}{|\vec{R}|} \vec{P}(\vec{r}'), \quad (2.9)$$

where the polarization vector  $\vec{P}(\vec{r}) = \epsilon_0 \chi \vec{E}(\vec{r})$  was introduced. The outgoing scattered wave given by Eq. (2.8) completes the exact solution to the scattering problem, Eq. (2.9), which is a version of the Lippmann-Schwinger equation for classical electrodynamics. The equation is generally quite difficult to solve as it is recursive in  $\vec{E}(\vec{r}')$  and involves complicated integrals over the volume of the dielectric. To solve Eq. (2.8) requires approximations or numerical techniques. In the special case of a spherical object the fields can be found exactly through an expansion in spherical waves known as Mie scattering [51, 52]. Fortunately, the majority of particles used in levitated optomechanics are smaller than the wavelength of light impinging on the particle allowing the dominant interaction to be described by particles in the Rayleigh regime. Most, but not all, of the situations that will be encountered in this thesis are under this assumption and from here we will proceed to find an approximate solution to Eq. (2.9) that will be relevant to the following chapters. It will be noted when the Rayleigh limit is no longer satisfied and methods for the solution will be outlined in the applicable chapter.

## 2.2 Rayleigh scattering

The simplest and most widely used approximation is the Rayleigh approximation named after Lord Rayleigh [53]. In this approximation the particle is considered to be a point dipole which is valid when the particle size is small compared to the wavelength,  $a \ll \lambda$ . The spatial variation of the electric field over the particle is then negligible for any  $\vec{E}_{\text{inc}}(\vec{r})$  and electrostatics may be used to find  $\vec{E}(\vec{r}')$  inside the particle. With the definitions of the polarization vector  $\vec{P}(\vec{r}) = \epsilon_0 \chi \vec{E}_{\text{inc}}(\vec{r})$ , dipole moment  $\vec{p} = \int \vec{P}(\vec{r}') d^3 r'$ , and applying  $|\vec{r} - \vec{r}'| = r$  to Eq. (2.8), the scattered field for a dipole is

$$\vec{E}_{\text{scatt}}(\vec{r}) = \frac{k^2}{4\pi\epsilon_0} \left( \mathbf{1} + \frac{1}{k^2} \nabla \nabla \right) \frac{e^{ikr}}{r} \vec{p} \quad (2.10)$$

$$= \frac{e^{ikr}}{4\pi\epsilon_0} \left\{ \frac{k^2}{r} [\vec{p} - (\hat{r} \cdot \vec{p}) \hat{r}] + [3\hat{r}(\hat{r} \cdot \vec{p}) - \vec{p}] \left( \frac{1}{r^3} - \frac{ik}{r^2} \right) \right\}. \quad (2.11)$$

Equation (2.11) may also be found in Ref. [49]. The first term in Eq. (2.11) is  $\propto 1/r$  and describes the scattered electric field in the far-field  $kr \gg 1$  whereas the near-zone is dominated by the  $1/r^3$  in the second term. The scattering in earth's atmosphere is predominantly described by Rayleigh scattering as the Sun's rays scatter off of air molecules. In the Rayleigh limit, the scattered field  $\propto \lambda^{-2}$  and the intensity  $\propto \lambda^{-4}$  showing that higher frequency light scatters significantly more than lower frequency light. This dependence on the wavelength is responsible for the blue color of earth's sky.

From Maxwell's equations one can also obtain the scattered magnetic field

$$\vec{B}_{\text{scatt}}(\vec{r}) = \frac{k^2}{4\pi Z_0} (\hat{r} \times \vec{p}) \frac{e^{ikr}}{r} \left( 1 - \frac{1}{ikr} \right), \quad (2.12)$$

where  $Z_0 = \sqrt{\epsilon_0/\mu_0}$  is the impedance of free space. In this approximation, besides the polarization, the form of the incident field did not need to be stated. So long as  $a \ll \lambda$  the electric field is effectively a constant across the particle. While this regime appears limited in its applicability for many applications, fortunately, this regime is often encountered in levitated optomechanics with typical laser wavelengths  $\lambda = 1550, 1064$  nm, particle radii of  $a \sim 100$  nm or less, and particle indexes of  $n \sim 2$ . Thus, while there is room for higher order terms their contributions are small and the physics is dominated by the dipole moment.

This approximation still retains the possibility for anisotropy in the particle's induced polarization and therefore information about the particle's shape is still relevant. Consequently, information about its orientation can also be obtained. Orientational information is located in the susceptibility tensor and therefore the dipole moment  $\vec{p}$ . This is important since particles of various shapes can be trapped such as rods, ellipsoids, dumbbells, and anisotropic particles [39, 54–56] each with different dynamics.

The dipole moment is often written in terms of the complex polarizability tensor  $\alpha = \epsilon_0 V \chi = \alpha' + i\alpha''$ , where  $V$  is the volume of the particle, since it gives a direct relation to the incident field  $\vec{p} = \alpha \vec{E}_{\text{inc}}$ . Valid for the Rayleigh approximation, the

elements of the polarizability tensor are determined in electrostatics by finding the electric fields inside of the particle and deducing the dipole moment. This can be done analytically for a finite number of shapes and in general must be computed numerically [57]. For time dependent fields the polarizability is frequency dependent owing to the frequency dependent relative permittivity  $\epsilon(\omega)$ . Further, in the same way that a charged particle radiates due to the acceleration caused by scattering, a process called 'radiation reaction', a polarized particle also experiences this phenomena [49, 58]. For a dipole of arbitrary shape the effect can be included in its complex polarizability as [58–60]

$$\alpha_j = \frac{\alpha_j^0}{1 - ik^3\alpha_j^0/6\pi\epsilon_0}, \quad (2.13)$$

where  $\alpha_j^0$  is the non-retarded polarizability along the eigen-directions of the polarizability tensor,  $j = (x, y, z)$ . The complex part of the polarizability,  $\alpha''$ , is associated with light absorption by the particle. However, from Eq. (2.13) even for perfectly non-absorbing particles  $\alpha'' = 0$ , the radiative reaction still term produces a non-zero imaginary term.

The shapes that will be of interest in later chapters are spheres and ellipsoid-like particles for which analytical expressions are available [53]. Spheres are the most convenient shape due to their symmetry, giving equal polarizability in each dimension  $\alpha_j^0 = \alpha$ . The polarizability of a sphere of radius  $a$  is

$$\alpha^0 = 4\pi\epsilon_0 a^3 \frac{\epsilon - 1}{\epsilon + 2} = 3\epsilon_0 V \frac{\epsilon - 1}{\epsilon + 2}. \quad (2.14)$$

For a prolate spheroid with the longest dimension in the  $z$ -direction having length  $a$  while the lengths in the  $x$  and  $y$  directions are  $b, c$  ( $b = c$ ), the polarizabilities are

$$\alpha_z^0 = 4\pi\epsilon_0 abc \frac{\epsilon - 1}{3 + 3L_z(\epsilon - 1)}, \quad (2.15)$$

$$\alpha_{x,y}^0 = 4\pi\epsilon_0 abc \frac{\epsilon - 1}{3 + 3L_x(\epsilon - 1)}, \quad (2.16)$$

with

$$L_z = \frac{1 - e^2}{e^2} \left( -1 + \frac{1}{2e} \ln \frac{1+e}{1-e} \right), \quad e^2 = 1 - \frac{b^2}{a^2}, \quad (2.17)$$

$$L_x = \frac{1 - L_z}{2}. \quad (2.18)$$

The general form of the  $L_i$  is in terms of integrals [53] and differ depending on the particle shape. For a sphere,  $L_z = L_x = 1/3$ , reducing Eqs. (2.15) and (2.16) to Eq. (2.14).

### 2.3 Rayleigh-Gans Scattering

When the Rayleigh approximation is insufficient, the next approach which is able to capture higher order effects due to finite-sized particles is Rayleigh-Gans scattering. Rayleigh-Gans scattering is valid in the regime  $ka|n - 1| \ll 1$  where  $n$  is the index of refraction and  $a$  is the size of the particle [52]. This is a constraint on the overall change of the fields over the particle in both magnitude and direction. Specifically, the  $|n - 1|$  in the restriction requires fairly transparent media. However, it does allow for the finite extension of the particle to be accounted for whereas Rayleigh scattering does not. So long as the distance at which the field is evaluated is large compared with the particles size, we can write  $|\vec{R}| \approx r - \hat{r} \cdot \vec{r}'$  in the phase of Eq. (2.8) and  $|\vec{R}| \approx r$  in the denominator

$$\vec{E}_{\text{scatt}}(\vec{r}) = \frac{k^2}{4\pi} \left( \mathbf{1} + \frac{1}{k^2} \nabla \nabla \right) \frac{e^{ikr}}{r} \int d^3r' e^{-i\vec{k} \cdot \vec{r}'} \chi \vec{E}(r'). \quad (2.19)$$

Depending on the situation the  $\frac{1}{k^2} \nabla \nabla \approx -\hat{r} \hat{r}$  for  $r \gg r'$ . The remaining integral in Eq. (2.19) is called the shape function and provides information about how the finite extent of the particle affects the scattering. It can be computed analytically for spheres, and for rods and disks when at least one dimension satisfies the Rayleigh limit  $ka \ll 1$  [52, 61–64].

## 2.4 Scattered fields in the far-zone

Although the full form for the scattered field is difficult to solve in general, much information about the scattering process can be learned by looking at particular limits in Eq. (2.8). Far away from the scatterer  $k|\vec{R}| \gg 1$ ,  $kr \gg 1$  the computational complexity is far reduced. In this limit Eq. (2.7) can be rewritten as

$$\mathbf{G}(\vec{r}, \vec{r}') \approx (\mathbf{1} - \hat{r}\hat{r}') \frac{e^{ikr}}{4\pi r} e^{-ik(\hat{r}\cdot\vec{r}')} \quad (2.20)$$

where the substitution  $|\vec{R}| \approx r - \hat{r} \cdot \vec{r}'$  was made in the exponential and  $|\vec{R}| \approx r$  for all other  $|\vec{R}|$ . The scattered electric field in the far-zone is

$$\vec{E}_{\text{scatt}}(\vec{r}) \approx \frac{e^{ikr}}{r} \frac{k^2}{4\pi} (\mathbf{1} - \hat{r}\hat{r}') \int d^3r' e^{-ik(\hat{r}\cdot\vec{r}')} \chi \vec{E}(\vec{r}') \quad (2.21)$$

$$= \frac{e^{ikr}}{r} \vec{F}(\vec{k}, \vec{k}'), \quad (2.22)$$

where  $\vec{F}(\vec{k}, \vec{k}')$  is the unnormalized vector scattering amplitude

$$\vec{F}(\vec{k}, \vec{k}') = \frac{k^2}{4\pi} (\mathbf{1} - \hat{r}\hat{r}') \int d^3r' e^{-ik(\hat{r}\cdot\vec{r}')} \chi \vec{E}(\vec{r}'). \quad (2.23)$$

The scattered field is written in the form of Eq. (2.22) to highlight that the radial dependence gives outgoing spherical waves. Information about the angular dependence of the fields as well as the properties of the scatterer are contained in the scattering amplitude.

The far-fields are useful for determining the power radiated by the particle in a certain direction. Using the time averaged Poynting vector,  $\vec{S}$ , the power radiated into the direction of observation  $\hat{r}$  per area is

$$\begin{aligned} \frac{dP}{dA} &= \hat{r} \cdot \vec{S} \\ &= \frac{1}{2} \hat{r} \cdot \text{Re} \left( \vec{E} \times \vec{H}^* \right) \\ &= \frac{1}{2Z_0} |\vec{E}|^2, \end{aligned} \quad (2.24)$$

for a TEM wave. From Eq. (2.22) the radial dependence on the power can already be seen to scale as  $1/r^2$ . It is then more valuable to look at the power per solid angle  $dP/d\Omega$

$$\frac{dP}{dA} = \frac{1}{r^2} \frac{dP}{d\Omega} \rightarrow \frac{dP}{d\Omega} = \frac{|\vec{F}|^2}{2Z_0}. \quad (2.25)$$

The outgoing scattered light may take two polarization directions  $\hat{\xi}$ , each of which is perpendicular to the direction of propagation in the far field limit. Examining the power delivered per solid angle for a particular polarization is done through

$$\left(\frac{dP}{d\Omega}\right)_\xi = \frac{|\hat{\xi} \cdot \vec{F}(\vec{k}, \vec{k}')|^2}{2Z_0}. \quad (2.26)$$

An important expression known as the differential scattering cross section,  $d\sigma/d\Omega$ , quantifies the fraction of incident light scattered into the solid angle  $d\Omega$ . It is defined as the ratio between the scattered power per solid angle and incident power per area

$$\left(\frac{d\sigma}{d\Omega}\right) = \left(\frac{dP_{\text{scatt}}}{d\Omega}\right) / \left(\frac{dP_{\text{inc}}}{dA}\right) \quad (2.27)$$

$$= \sum_j |\hat{\xi}_j \cdot \hat{f}(\vec{k}, \vec{k}')|^2, \quad (2.28)$$

where the sum is taken over both outgoing polarization directions and the normalized scattering amplitude was introduced,  $\vec{f}(\vec{k}, \vec{k}') = \vec{F}(\vec{k}, \vec{k}')/|\vec{E}_{\text{inc}}|$ . It is a probability density for scattering in a particular direction. Explicitly, light propagating in the spherical  $\hat{k}_f = \hat{r}$  direction allows  $\hat{\xi}_1 = \hat{\theta}$  and  $\hat{\xi}_2 = \hat{\phi}$  as one possible choice of outgoing polarizations and thus

$$\left(\frac{d\sigma}{d\Omega}\right) = |\hat{\theta} \cdot \vec{f}(\vec{k}, \vec{k}')|^2 + |\hat{\phi} \cdot \vec{f}(\vec{k}, \vec{k}')|^2. \quad (2.29)$$

The total cross section  $\sigma = \int (d\sigma/d\Omega) d\Omega$  has the dimensions of area and is the proportionality constant for the total scattered power by the particle for a given incident intensity,  $P_{\text{scatt}} = I_{\text{inc}}\sigma$ .

Using the scattered far-field expression for isotropic Rayleigh particles in Eq. (2.11), the differential scattering cross section for Rayleigh particles can be com-

puted. For incident light traveling in  $\hat{z}$  and polarized in the  $\hat{x}$ ,  $\hat{y}$ , or unpolarized directions

$$\left(\frac{d\sigma}{d\Omega}\right)_x = \left(\frac{k^2\alpha}{4\pi\epsilon_0}\right)^2 [\cos^2\theta \cos^2\phi + \cos^2\phi], \quad (2.30)$$

$$\left(\frac{d\sigma}{d\Omega}\right)_y = \left(\frac{k^2\alpha}{4\pi\epsilon_0}\right)^2 [\cos^2\theta \sin^2\phi + \sin^2\phi], \quad (2.31)$$

$$\left(\frac{d\sigma}{d\Omega}\right)_* = \left(\frac{k^2\alpha}{4\pi\epsilon_0}\right)^2 \frac{1}{2} [\cos^2\theta + 1], \quad (2.32)$$

$$(2.33)$$

respectively. Regardless of the polarization choice,

$$\sigma = \left(\frac{8\pi}{3}\right) \left(\frac{k^2\alpha}{4\pi\epsilon_0}\right)^2. \quad (2.34)$$

## 2.5 Interaction energy and forces

The discussion thus far has been focused on the scattered fields from a particle. The incident and scattered fields that reside within the particle have energy and are necessarily coupled to the particle. The light-matter coupling is what gives rise to the forces that levitated optomechanics is concerned with. The time averaged interaction energy is [65]

$$U_{\text{int}} = \frac{1}{4} \int d^3r' \vec{P}(\vec{r}')^* \cdot \vec{E}(\vec{r}'), \quad (2.35)$$

where the integral is over the volume of the particle and  $*$  denotes the complex conjugate. The force is then found through  $\vec{F} = -\nabla U_{\text{int}}$ . For Rayleigh particles, the force can be split into two components: a conservative gradient force which is responsible for trapping

$$\vec{F}_{\text{grad}} = \frac{\alpha'}{4} \nabla [\vec{E}^* \cdot \vec{E}], \quad (2.36)$$

and a non-conservative scattering force

$$\vec{F}_{\text{scatt}} = \omega\mu_0\alpha''\vec{S} - i\frac{\alpha''}{4} \left[ \nabla \times (\vec{E} \times \vec{E}^*) \right], \quad (2.37)$$

where  $\vec{S}$  is the time average Poynting vector and the last term in Eq. (2.37) is relevant for fields with nonzero angular momentum. The net optical force is then

$$\vec{F} = \vec{F}_{\text{grad}} + \vec{F}_{\text{scatt}}. \quad (2.38)$$

The equations above will be computed and examined more closely in the following chapter.

Alternatively, the incident and scattered fields computed from Eq. (2.8) together with the Maxwell Stress tensor [49]

$$T_{ij} = \epsilon_0 \left[ E_i E_j + c^2 B_i B_j - \frac{1}{2} \left( |\vec{E}|^2 + c^2 |\vec{B}|^2 \right) \delta_{ij} \right], \quad (i, j) = (x, y, z), \quad (2.39)$$

can be used to obtain the net optical forces and torques

$$\vec{F} = \oint \mathbf{T} \cdot \hat{n} dS, \quad (2.40)$$

$$\vec{\tau} = \oint \mathbf{M} \cdot \hat{n} dS, \quad (2.41)$$

where  $\mathbf{M} = -\mathbf{T} \times \vec{r}$  and the integral is over a specified closed surface enclosing the particle.

Lastly, the scattering force can be calculated in another view by considering the momentum that is transferred from the photons to the particle

$$\vec{F}_{\text{scatt}} = J_p \int \left( \frac{d\sigma}{d\Omega} \right) \Delta \vec{p} d\Omega, \quad (2.42)$$

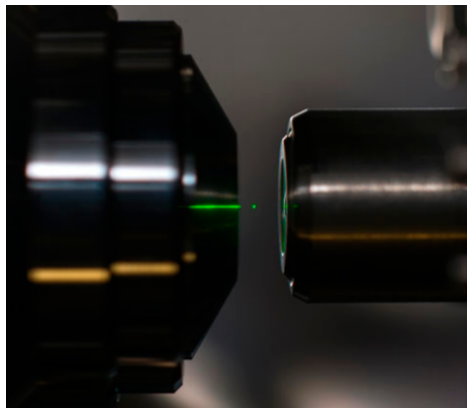
where  $J_p = I_0/\hbar\omega$  is the photon flux and  $\Delta p = \hbar k [(1 - \cos(\theta)) \hat{z} + \sin(\theta)\hat{\rho}]$  is the momentum transfer function for a photon initially propagating in the  $\hat{z}$  direction.

Each method for computing the forces necessarily gives equivalent results. Nonetheless, given a problem at hand, it is useful to look at the scenario from several perspectives.

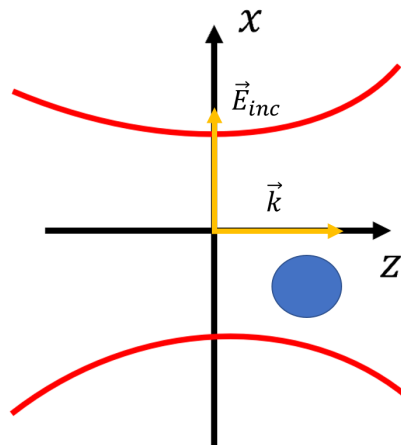
### 3. TRANSLATIONAL MOTION

This chapter presents the well known translational dynamics of a dielectric nanosphere in the focus of a Gaussian beam as well as the common methods of measuring the motion.

#### 3.1 The Gradient Force



(a)



(b)

Figure 3.1. (a) Picture of an actual silica nanosphere trapped in the focus of a laser beam. Image taken from [44]. (b) Model of the system. A nanosphere (blue) is trapped and oscillates about the focus of a Gaussian laser beam (red) traveling in the  $z$ -direction and polarized in the  $x$ -direction (yellow).

This section will demonstrate how a focused laser beam is able to yield three dimensional translational trapping of a dielectric nanosphere of radius  $R \ll \lambda$ , mass

$M$ , and polarizability  $\alpha$ . The procedure can be generalized for arbitrary particle shape. In levitated optomechanical experiments the particle is trapped near the focus of a tightly focused laser beam. The simplest and most common description of the beam at the focus is the (0,0) mode of a Gaussian beam. Consider a Gaussian laser beam traveling in the  $\vec{k} = \frac{2\pi}{\lambda} \hat{z}$  direction and polarized in the  $\hat{E}_{\text{inc}} = \hat{x}$  direction as in Fig. 3.1(b). The electric field incident on the nanosphere is [66]

$$\vec{E}_{\text{inc}} = E_0 \frac{\omega_0}{\omega(z)} e^{\frac{-\rho^2}{\omega^2(z)}} e^{i(kz + \frac{k\rho^2}{2R(z)} - \psi(z))} \hat{x}. \quad (3.1)$$

The Gaussian beam is defined with  $(x, y, z) = (0, 0, 0)$  to be the center of the focus and  $\omega_0$  the beam waist,  $\omega(z) = \omega_0 \sqrt{1 + (z/z_R)^2}$  with  $z_R = \pi\omega_0^2/\lambda$  the Rayleigh range,  $\rho^2 = x^2 + y^2$ ,  $k = 2\pi/\lambda$ ,  $R(z) = z[1 + (z_R/z)^2]$ , and  $\psi(z) = \arctan(z/z_R)$ . From Eq. (2.35), the potential energy of the nanosphere is given by

$$\begin{aligned} U &= -\frac{1}{4} \vec{p}^* \cdot \vec{E}_{\text{inc}} \\ &= -\frac{1}{4} \alpha E_0^2 \frac{\omega_0^2}{\omega^2(z)} e^{\frac{-2\rho^2}{\omega^2(z)}} \end{aligned} \quad (3.2)$$

where  $\vec{p} = \alpha \vec{E}_{\text{inc}}$  is the electric dipole moment of the nanosphere. The conservative force due to the field, Eq. (2.36), is

$$\vec{F}_{\text{grad}} = -\alpha E_0^2 \left[ \frac{1}{\omega_0^2 (1 + z^2/z_R^2)^2} \right] \begin{pmatrix} x \\ y \\ \frac{z\omega_0^2}{2z_R^2} - \frac{z\rho^2}{(z^2 + z_R^2)} \end{pmatrix} e^{\frac{-2\rho^2}{\omega^2(z)}}. \quad (3.3)$$

It is seen that the forces in the  $x$  and  $y$  directions are identical and attractive while the force in  $z$  is repulsive only for large transverse motion and weakly focused beams ( $\omega_0/z_R = \text{NA}$ , where NA is the numerical aperture of the lens used to focus the beam). As trapping is desired rather than a repulsive interaction, a strongly focused beam is used in practice. Considering a highly focused laser, the nanosphere is located near

the center of the focus and the approximations  $\exp(-2\rho^2/\omega^2(z)) \approx 1 - 2\rho^2/\omega_0^2$  and  $(1 + (z/z_R)^2)^{-1} \approx 1 - z^2/z_R^2$  may be made to give

$$\vec{F}_{\text{grad}} \approx -\alpha E_0^2 \begin{pmatrix} x/\omega_0^2 \\ y/\omega_0^2 \\ z/2z_R^2 \end{pmatrix}. \quad (3.4)$$

Equation (3.4) reveals that the particle will undergo simple harmonic motion about the focal point. The frequencies of oscillation are

$$\omega_x^2 = \frac{\alpha E_0^2}{M} \frac{1}{\omega_0^2}, \quad (3.5)$$

$$\omega_z^2 = \frac{\alpha E_0^2}{M} \frac{1}{2z_R^2}. \quad (3.6)$$

Note that the frequencies do not depend on the radius of the particle, but only on the density  $\rho$  and dielectric constant  $\epsilon$  since  $\omega_i^2 \propto F_i/M \propto \alpha/M$  and  $\alpha$  and  $M$  are both proportional to volume.

To give a sense of typical sizes commonly seen in levitated optomechanics, Eqs. (3.5) and (3.6) will be evaluated here. Using laser parameters  $P = 200$  mW,  $\lambda = 1550$  nm, and  $\text{NA} = 0.6$  together with a silica nanosphere of density  $\rho = 2000$  kg/m<sup>3</sup>, and dielectric constant  $\epsilon = 2.1$  ( $\alpha = 4.94 \times 10^{-33}$  C<sup>2</sup>m/N,  $M = 1.05 \times 10^{-18}$  kg) gives  $\omega_{x,y}/2\pi = 158$  kHz and  $\omega_z/2\pi = 67$  kHz. In practice,  $\omega_{x,y}/2\pi$  are typically in the 50 – 200 kHz range while  $\omega_z/2\pi \sim 10 - 100$  kHz and typical radii of the particles range from  $R = 50$  nm – 1  $\mu\text{m}$ .

### 3.2 The Scattering Force

As Ashkin first observed [67], the momentum of light from the laser pushes a particle away from the focus in the axial direction through radiation pressure. To determine the approximate size of this translational displacement, consider a laser with intensity  $I_0$ , power  $P_0$ , and wavevector  $\vec{k} = \frac{2\pi}{\lambda} \hat{z}$  incident on a dumbbell of radius

$R$  and polarizability  $\alpha = \alpha' + i\alpha''$  (see Sec. 2.2). The average scattering force from Eqs. (2.37) or (2.42) gives

$$\vec{F}_{\text{scatt}} \approx \alpha'' E_0^2 k \left(1 - \frac{1}{z_R k}\right) \hat{z}, \quad (3.7)$$

to first order. The scattering force is proportional to the imaginary part of the polarizability,  $\alpha''$ . Recall from Sec. 2.2 that the imaginary component of the polarizability is non-zero even for non-absorbing particles. Radiation pressure is dominant in the axial degree of freedom. The next order terms exist for all degrees of freedom, but are quadratic in the displacement and therefore negligible for most practical purposes.

The distance by which the particle is displaced from the focus of the beam,  $z_d$ , can be estimated by using the equations of motion to first order with the nanoparticle in its equilibrium position

$$m\ddot{z} = 0 = -m\omega_z^2 z_d + F_{\text{scatt},z}, \quad (3.8)$$

yielding

$$\frac{z_d}{z_R} = 2 \frac{\alpha''}{\alpha'} (kz_R - 1), \quad (3.9)$$

relative to the Rayleigh range,  $z_R$ . Using the same values as in Sec. 3.1,  $z_d/z_R = 0.1$  or about 150 nm for a  $R = 100$  nm sphere.

### 3.3 Measuring the particle displacement

A fundamental component in levitated optomechanics is the ability to track the motion of a particle in real time. Because of the small size of the relatively transparent particle the intensity of scattered light is small and difficult to detect. The technique often employed to detect the position makes use of the interference between the laser beam and the scattered light off of the nanoparticle and is called homodyning [22, 23, 68–71]. Following a condensing and focusing lens, the combined signal is incident upon a photodetector split into four equal segments, known as a quadrant photodetector. To obtain the position  $x$  of the particle relative to the center of the

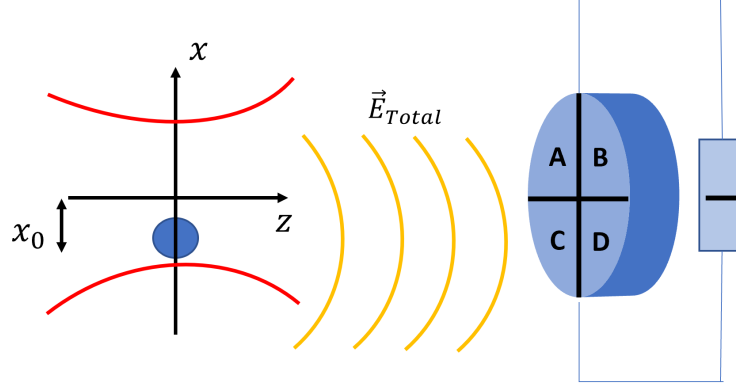


Figure 3.2. Illustration of the measurement procedure. The scattered light (yellow) from the nanoparticle (blue) is homodyned with the laser beam and the resulting signal is incident upon a quadrant photodiode. A measurement of the displacement  $x_0$  from the focus is performed by subtracting the sections  $(A+B)-(C+D)$  while for a measurement in the  $y$  direction  $(A+C)-(B+D)$ .

focal point the signals in the two leftmost quadrants are subtracted from the two rightmost quadrants. This scheme gives a signal proportional to the displacement  $x_0$ . The signal is then Fourier transformed to give a power spectral density which allows the experimental determination of the translational frequencies, Eqs. (3.5) and (3.6). The illustration of the setup can be seen in Fig. 3.3.

Consider again the Gaussian beam given by Eq. (3.1) incident upon a nanosphere located at  $\vec{r}^j = x_0\hat{x}$ . The incident light polarizes the nanoparticle inducing a dipole moment  $\vec{p} = \alpha\vec{E}_{\text{inc}}(x_0, 0, 0) \approx \alpha E_0\hat{x}$ . The scattered light for a dipole in the far field is (Sec. 2.2)

$$\vec{H}_p = \frac{ck^2}{4\pi}(\hat{R} \times \vec{p})\frac{e^{ikR}}{R}, \quad (3.10)$$

$$\vec{E}_p = Z_0\vec{H} \times \hat{R}, \quad (3.11)$$

where  $\vec{R} = \vec{r} - \vec{r}^j = \langle x - x_0, y, z \rangle$ ,  $\vec{r}$  is in the direction of observation,  $Z_0$  is the impedance of free space, and the subscript  $p$  stands for the particle. Ignoring the effects of the lenses for the moment, the signal reaches a photodiode located at

$\langle 0, 0, L \gg z_R \rangle$  with its planar surface parallel to the  $x - y$  plane. In terms of the Poynting vector, the signal is

$$\begin{aligned} \vec{S} &= \frac{1}{2} \text{Re} \left[ \vec{E}_{\text{Total}} \times \vec{H}_{\text{Total}}^* \right] \\ &= \frac{1}{2} \text{Re} \left[ (\vec{E}_p \times \vec{H}_{\text{inc}}^*) + (\vec{E}_{\text{inc}} \times \vec{H}_p^*) + (\vec{E}_p \times \vec{H}_p^*) + (\vec{E}_{\text{inc}} \times \vec{H}_{\text{inc}}^*) \right], \end{aligned} \quad (3.12)$$

where  $\vec{H}_{\text{inc}} = \frac{1}{\mu_0 c} (\vec{E}_{\text{inc}} \cdot \hat{x}) \hat{y}$ . The first two terms in Eq. (3.12) are the homodyne terms while the last two play no role in the measurement since the scattered intensity is very small compared to the incident light and the outgoing incident power adds an overall constant independent of the particle position. A photodetector reads the intensity of the incoming beam which are the components parallel to its surface. Thus, the only component needed from the Poynting vector is  $\vec{S} \cdot \hat{z}$ . Evaluating the homodyne terms in the Poynting vector and taking the dot product gives

$$\vec{S} \cdot \hat{z} = \frac{1}{2} \text{Re} \left[ AB \left( 1 - \frac{(x - x_0)x}{R^2} \right) + AB^* \left( \frac{y}{R} \right) \right] \quad (3.13)$$

where  $A = \frac{\alpha E_0^2 \omega_0}{\omega(L)R} \frac{ck^2}{4\pi} e^{-\rho^2/\omega^2(L)}$  and  $B = e^{ikR} e^{-i(kL + \frac{k\rho^2}{2R(L)} - \psi(L))}$ . Integrating over the entire detector and subtracting the two leftmost quadrants from the rightmost quadrants gives the power

$$P_x = \int_0^\infty \int_{-\infty}^\infty (\vec{S} \cdot \hat{z}) dy dx - \int_{-\infty}^0 \int_{-\infty}^\infty (\vec{S} \cdot \hat{z}) dy dx. \quad (3.14)$$

In order to evaluate the integrals some approximations must be made. First, the length  $L$  is at least on the centimeter scale while the dimensions of the photodiode  $x, y$  are  $\sim$  mm and the particle displacement  $x_0 \sim$  nm. Expanding the relative distance vector  $\vec{R}$  in  $B$  to second order

$$\begin{aligned} B &= \exp \left( i \left( kR - kL - k\rho^2/2R(L) + \psi(L) \right) \right) \\ &\approx \exp \left( i \left( -\frac{kxx_0}{L} + \pi/2 \right) \right) \end{aligned} \quad (3.15)$$

where the approximation  $\psi(L) = \arctan(L/z_R) \approx \pi/2$ , known as the Gouy phase shift [72], was made. The main idea of this measurement can be seen in Eq. (3.15)

as the interference has brought information about the displacement within the phase. Further expanding the denominators in  $A$  to first order  $\omega(L) \approx \omega_0 L/z_R$  and  $R \approx L$  yields

$$\vec{S} \cdot \hat{z} \approx \left( \frac{\alpha E_0^2 z_R}{2L^2} \right) \left( \frac{ck^2}{4\pi} \right) e^{-\rho^2/\omega^2(L)} \left( \frac{kxx_0}{L} \right) \left[ 1 - \left( \frac{y}{L} \right) \right]. \quad (3.16)$$

Performing the Gaussian integrals in Eq. 3.14 using Eq. 3.16 gives

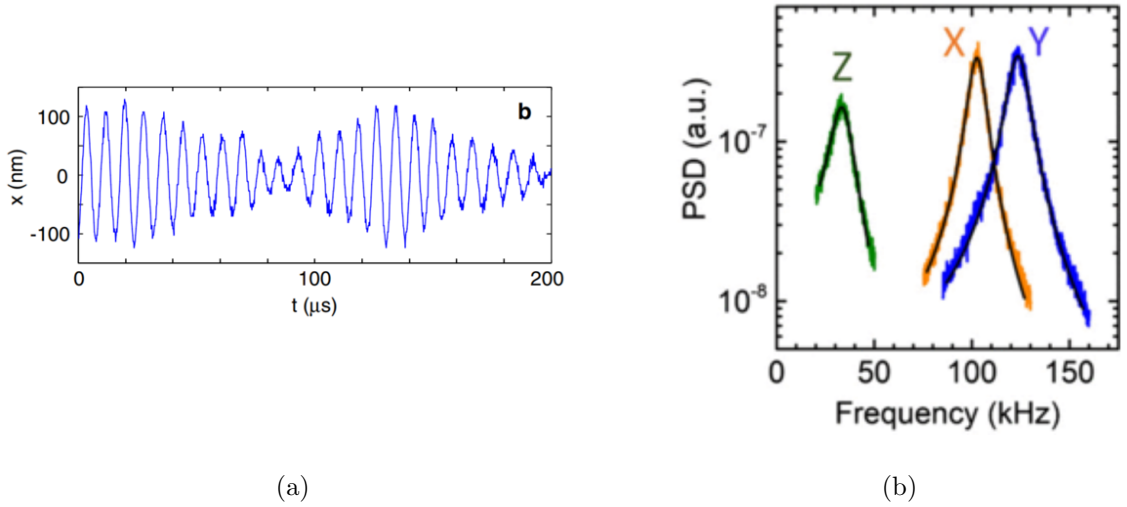


Figure 3.3. (a) Time trace of the experimentally measured position observing the oscillatory behavior. Picture taken from [23]. (b) Power spectral density of measured  $x, y, z$  positions from Ref. [56].

$$P_x \approx \left( \frac{2\alpha PNA^3}{\pi^{5/2}\epsilon_0\lambda^4} \right) x_0, \quad (3.17)$$

in terms of the experimentally tunable power, numerical aperture, and wavelength of the beam. This simplified measurement calculation results in a signal that is directly proportional to the displacement to first order. Figure 3.3(a) shows a plot of the experimentally measured position of a nanosphere from [23]. This was only possible through the Gouy phase shift of  $\pi/2$  seen in Eq. (3.15). A measurement of the displacement  $y_0$  is performed in the same manner by subtracting the upper and lower most quadrants of the photodetector. The displacement  $z_0$  is measured differently than the transverse motions. One method for measuring  $z_0$  is by subtracting the

signals between two detectors placed a distance  $z$  away from one another, but will not be calculated here [73–75]. Here the effects of the lenses [66] were safely neglected as they introduce higher order terms that include all three displacements  $x_0, y_0, z_0$  scaled by the various length scales of the system. For larger, non-Rayleigh particles, the higher order terms may need to be considered.

## 4. ROTATIONAL MOTION

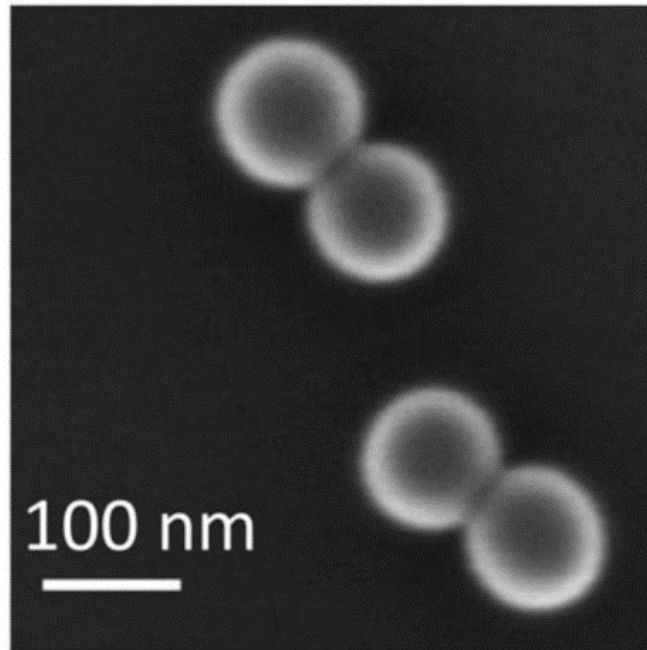


Figure 4.1. Scanning electron microscope image of actual silica nanodumbbells used in the experiments of Ref. [56]. Photo credit to the same reference.

This chapter examines the rotational dynamics of a dielectric nanodumbbell in the focus of a Gaussian beam as well as the methods of measuring the motion. Much of this work may be found in our paper [76]. The term *libration* (also known as *torsional* motion) will be used in the following sections and stands for harmonic rotational oscillations in a particular plane.

A sphere is symmetric with respect to rotations which in effect produces no rotational potential energy. Only non-spherical particles experience a torque in a linearly polarized beam. While the translational motion in Sec. 3.1 is fairly intuitive, ro-

tational dynamics can become complicated for generally anisotropic particles. The simplest shape with a nonzero torque is a nanorod with two principal moments of inertia equal  $I_x = I_y$  and the moment of inertia about the symmetry axis negligible  $I_x \gg I_z \approx 0$ . The dynamics of a nanorod are relatively simple and amount to libration about the laser polarization axis [54, 59]. One of the next simplest shapes that produces a nonzero torque is a symmetric top defined by having two principal moments of inertia the same  $I_x = I_y$  with relation to the third moment  $I_x \neq I_z \neq 0$ . Recently, the torsional motion of a nanodumbbell was measured [56] and cooled [77]. A theoretical analysis of the dynamics for particles of this shape was missing until our publication. For this reason and for the purpose of what follows in Chap. 6, the symmetric-top particle of choice for the analysis below will be a nanodumbbell.

#### 4.1 Classical dynamics

Consider a nanodumbbell optically trapped in a laser field. The particle's center of mass is fixed at the origin so that only rotations are considered. The nanodumbbell is composed of two spheres each with mass  $M_s$  and radius  $R$ . The spheres are aligned along the  $z'''$ -axis and touching at the origin, where the triple prime indicates the particle frame coordinate system (see Fig. 4.2). It is a symmetric top with principal moments of inertia  $I_x = I_y = \frac{14}{5}M_s R^2$  and  $I_z = \frac{4}{5}M_s R^2$ . The laser beam is linearly polarized along the lab frame  $x$  direction and propagating in the  $z$  direction with a wavelength  $\lambda \gg R$ . As in Sec. 3.1, the nanodumbbell is treated as a point dipole with  $\vec{E}_{\text{inc}} = E_0 \hat{x}$ , the electric field polarizing the dumbbell, having no spatial dependence due to the small size of the dumbbell.

The rotational dynamics are governed by the classical equations of motion described by the Euler angles  $(\alpha, \beta, \gamma)$  [78, 79] in the  $z$ - $y'$ - $z''$  convention. To transform from the lab  $(x, y, z)$  frame to the particle  $(x''', y''', z''')$  body frame, three rotation transformations are made. First, a rotation about the lab frame  $z$ -axis through an angle  $\alpha$  is performed,  $(x, y, z) \rightarrow (x', y', z' = z)$ . Then, a rotation about the  $y'$ -axis

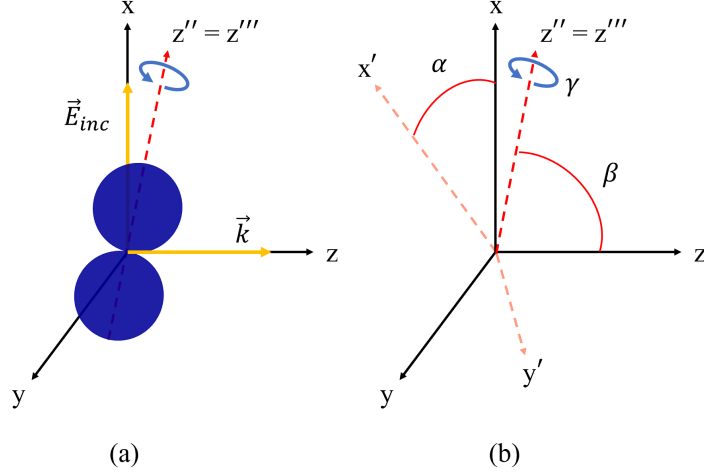


Figure 4.2. (a) A nanodumbbell with center of mass confined to the origin is allowed to rotate. The particle has the lowest energy when its long axis ( $z'''$ -axis) aligns with the laser's electric field polarized in the lab frame  $x$ -direction. (b) The definition of the Euler angles  $\alpha$ ,  $\beta$ ,  $\gamma$  shown in the  $z$ - $y'$ - $z''$  convention. For small angle rotations, the coordinate  $\alpha = 0 + \xi$  describes rotations near the lab frame  $x$ -axis in the  $x$ - $y$  plane and  $\beta = \pi/2 - \eta$  describes rotations near the lab frame  $x$ -axis in the  $x$ - $z$  plane. The coordinate  $\gamma$  describes rotations about the  $z'' = z'''$  axis with  $\gamma(t) \approx \omega_3 t$ . For visual clarity, the  $x'', y'', x''', y'''$  axes have been omitted from the figure.

is made through an angle  $\beta$ ,  $(x', y', z') \rightarrow (x'', y'' = y', z'')$ . Finally, a rotation about the  $z''$ -axis is made through an angle  $\gamma$ ,  $(x'', y'', z'') \rightarrow (x''', y''', z''' = z'')$ . In this configuration, each Euler angle has an intuitive definition for small amplitude oscillations;  $\alpha$  defines libration in the  $x$ - $y$  plane,  $\beta$  defines libration in the  $x$ - $z$  plane, and  $\gamma$  corresponds to angles of rotation about the  $z'''$ -axis.

The rotation matrix  $\vec{R}$  in terms of the Euler angles in the  $z$ - $y'$ - $z''$  convention is

$$\vec{R} = \vec{R}_{z''} \vec{R}_{y'} \vec{R}_z, \quad (4.1)$$

and

$$\overset{\leftrightarrow}{R}_z = \begin{pmatrix} \cos \alpha & \sin \alpha & 0 \\ -\sin \alpha & \cos \alpha & 0 \\ 0 & 0 & 1 \end{pmatrix}, \quad (4.2)$$

$$\overset{\leftrightarrow}{R}_{y'} = \begin{pmatrix} \cos \beta & 0 & -\sin \beta \\ 0 & 1 & 0 \\ \sin \beta & 0 & \cos \beta \end{pmatrix}, \quad (4.3)$$

$$\overset{\leftrightarrow}{R}_{z''} = \begin{pmatrix} \cos \gamma & \sin \gamma & 0 \\ -\sin \gamma & \cos \gamma & 0 \\ 0 & 0 & 1 \end{pmatrix}. \quad (4.4)$$

The kinetic and potential energies are

$$K = \frac{1}{2}I_x(\omega_1^2 + \omega_2^2) + \frac{1}{2}I_z\omega_3^2, \quad (4.5)$$

$$\begin{aligned} U &= -\frac{1}{4}\vec{p} \cdot \vec{E}_{\text{inc}} \\ &= -\frac{1}{4}(\alpha_z - \alpha_x)E_0^2 \cos^2(\alpha) \sin^2(\beta), \end{aligned} \quad (4.6)$$

where

$$\begin{aligned} \vec{p} &= \overset{\leftrightarrow}{R} \overset{\leftrightarrow}{\alpha}_0 \overset{\leftrightarrow}{R} \vec{E}_{\text{inc}} \\ &= E_0 \begin{pmatrix} (\alpha_z - \alpha_x) \cos^2(\alpha) \sin^2(\beta) \\ (\alpha_z - \alpha_x) \sin^2(\beta) \cos(\alpha) \sin(\alpha) \\ (\alpha_z - \alpha_x) \cos(\beta) \sin(\beta) \cos(\alpha) \end{pmatrix} \\ &\equiv \langle p_x, p_y, p_z \rangle, \end{aligned} \quad (4.7)$$

is the nanodumbbell polarization vector in the lab frame,  $\overset{\leftrightarrow}{\alpha}_0$  is the diagonal polarizability matrix with the  $\alpha_j$  ( $j = x, y, z$ ) [53, 59] the polarizabilities for an ellipse in the particle frame ( $\alpha_x = \alpha_y$ ) and are not to be confused with the coordinate  $\alpha$ . The body frame angular velocities are given by

$$\omega_1 = \dot{\beta} \sin(\gamma) - \dot{\alpha} \sin(\beta) \cos(\gamma), \quad (4.8)$$

$$\omega_2 = \dot{\beta} \cos(\gamma) + \dot{\alpha} \sin(\beta) \sin(\gamma), \quad (4.9)$$

$$\omega_3 = \dot{\alpha} \cos(\beta) + \dot{\gamma} = \text{const.} \quad (4.10)$$

It should be noted that as a consequence of the nanodumbbell's symmetry, the angular momentum about the nanoparticle's symmetry axis,  $I_z\omega_3$ , is a constant of the motion [Eq. (4.10)]. Constant terms in Eqs. (4.6) and (4.7) have been omitted as they do not affect the particle's rotational dynamics. The full equations of motion for the three angles  $\alpha, \beta, \gamma$  are found through the Lagrangian giving

$$\ddot{\alpha} = -2\dot{\alpha}\dot{\beta} \cot(\beta) + \dot{\beta} \csc(\beta) \frac{I_z}{I_x} \omega_3 - \frac{1}{I_x \sin^2(\beta)} \left( \frac{\partial U}{\partial \alpha} \right), \quad (4.11)$$

$$\ddot{\beta} = \sin(\beta) \left( \dot{\alpha}^2 \cos(\beta) - \dot{\alpha} \frac{I_z}{I_x} \omega_3 \right) - \frac{1}{I_x} \left( \frac{\partial U}{\partial \beta} \right), \quad (4.12)$$

$$\dot{\gamma} = \omega_3 - \dot{\alpha} \cos(\beta). \quad (4.13)$$

The attractive potential, Eq. (4.6), causes the particle to oscillate about the polarization axis in two joint motions (see Fig. 4.1). The two motions are most easily seen when the equations are written under a small angle approximation. It is energetically favorable for the particle's long axis ( $z'''$ -axis) to align with the electric field and is therefore localized near the lab frame  $x$ -axis. This corresponds to  $\alpha$  nearing towards zero or  $\pi$ , and  $\beta$  near  $\pi/2$ . Allowing the two coordinates to make small oscillations about the  $x$ -axis,  $\alpha \rightarrow 0 + \xi$   $\beta \rightarrow \frac{\pi}{2} - \eta$ , with  $\xi, \eta$  small, the equations of motion to first order become

$$\begin{aligned} \ddot{\xi} &= \left[ -\frac{\omega^2}{2} \sin(2\xi) - \omega_c \dot{\eta} \sec(\eta) + 2\dot{\eta} \dot{\xi} \tan(\eta) \right] \\ &\approx -\omega^2 \xi - \omega_c \dot{\eta}, \end{aligned} \quad (4.14)$$

$$\begin{aligned} \ddot{\eta} &= \cos(\eta) \left[ -\omega^2 \sin(\eta) \cos^2(\xi) + \omega_c \dot{\xi} - \dot{\xi}^2 \sin(\eta) \right] \\ &\approx -\omega^2 \eta + \omega_c \dot{\xi}, \end{aligned} \quad (4.15)$$

where  $\omega^2 = \frac{1}{2}(\alpha_z - \alpha_x)E_0^2/I_x$  and  $\omega_c = (I_z/I_x)\omega_3$ . The first term on the right hand side of Eqs. (4.14) and (4.15) amounts to harmonic oscillations (libration) about the polarization axis due to the trapping potential which has been seen before in [80, 81]. The second term containing  $\omega_c$  couples the four DOF and is responsible for precession about the  $x$ -axis. The precession is a consequence of the nonzero angular momentum about the symmetry axis,  $I_z\omega_3$ . Precession has recently been seen for anisotropic

particles in an elliptically polarized beam [55], but with  $\alpha$  precessing around the lab frame  $z$ -axis with  $\beta$  roughly fixed. As in the case for thin nanorods, the motion reduces to pure libration in the limit  $I_z \rightarrow 0$ . The equation of motion for  $\gamma$  is not directly affected by the potential and largely evolves with time as  $\gamma(t) \approx \omega_3 t$  in the small angle approximation (see Eq.(4.13)).

The transformation of the  $z'''$ -axis into the lab frame,  $\hat{r}_{z'''} = \overset{\leftrightarrow}{R} \hat{z}'''$ , determines the location of the tip in the  $(x, y, z)$  coordinate system,

$$\hat{r}_{z'''} = \begin{pmatrix} \sin(\beta) \cos(\alpha) \\ \sin(\beta) \sin(\alpha) \\ \cos(\beta) \end{pmatrix} \approx \begin{pmatrix} 1 \\ \xi \\ \eta \end{pmatrix}, \quad (4.16)$$

where in the last step the small angle approximation was made. It is seen that  $\xi$  and  $\eta$  play the role of the  $y$  and  $z$  coordinates defining the location of the tip of the nanodumbbell. By introducing a vector that specifies the projection of the  $z'''$ -axis on the  $y$ - $z$  plane,  $\vec{\rho}_{z'''} = \langle 0, \xi, \eta \rangle$ , it is possible to combine Eqs. (4.10), (4.11),

$$\ddot{\vec{\rho}}_{z'''} = -\omega^2 \vec{\rho}_{z'''} - \dot{\vec{\rho}}_{z'''} \times \vec{\omega}_c, \quad (4.17)$$

where  $\vec{\omega}_c = \omega_c \hat{x} = (I_z/I_x) \omega_3 \hat{x}$ . The last term in Eq. (4.17) has the familiar form of the force on a charged particle in a magnetic field. The two joint motions now become clear as a combination of harmonic oscillations in a static pseudo-magnetic field. Thus, as long as  $\omega_c$  is nonzero, the full dynamics of the nanoparticle must be described as a combination of libration and precession, as opposed to just libration. For a nanodumbbell at room temperature,  $T = 300$  K, the average value of  $\omega_c/2\pi \sim \sqrt{k_B T I_z} / (2\pi I_x) \sim 10$  kHz, where  $k_B$  is the Boltzmann constant. While  $\omega/2\pi \sim 100$  kHz – 1 MHz  $\gg \omega_c/2\pi$ , the coupling that results due to the  $\sim 10$  kHz frequency is a resolvable feature in the power spectral density and is a non-negligible effect when considering parametric feedback cooling, as will be discussed in Chap. 6.

The librational frequency  $\omega$  scales with the radius as  $\omega^2 \sim 1/R^2$  suggesting that a particle of smaller size is beneficial for ground state cooling. However, the polarizability and moment of inertia scale as  $\alpha_j \sim R^3$ ,  $I_j \sim R^5$  implying that the particle will

be less confined and more unstable in the optical trap as the size decreases. In effect, a smaller radius will be more likely to escape the trap and will produce a broader power spectral density. Further,  $\omega_c \sim 1/R^{5/2}$  showing that as the size of the particle decreases the precessional phenomenon is more pronounced.

Equations (4.14) and (4.15) admit two normal modes,

$$\xi(t) = A_+ \cos(\omega_+ t + \delta_+) + A_- \cos(\omega_- t + \delta_-), \quad (4.18)$$

$$\eta(t) = A_+ \sin(\omega_+ t + \delta_+) - A_- \sin(\omega_- t + \delta_-), \quad (4.19)$$

with  $\omega_{\pm} = \frac{1}{2}(\Omega \pm \omega_c)$ ,  $\Omega = \sqrt{4\omega^2 + \omega_c^2}$ , and the  $A_{\pm}$ ,  $\delta_{\pm}$  determined by initial conditions. Each mode circles the polarization axis at a particular frequency with the (+) mode advancing clockwise and the (-) mode counterclockwise. The superposition of the two modes results in the libration and precession mentioned above. Thus, as will be discussed in Chap. 6, the power spectral density of  $\xi$  or  $\eta$  should exhibit two peaks at  $\omega_{\pm}$ .

Since the coordinates  $\alpha$  and  $\beta$  completely describe the location of the nanodumbbell's tip projected on the lab frame axes, it is possible to track the rotational evolution about the polarization axis while simulating the full equations of motion. Figure 4.1 plots the  $z'''$ -axis projection on the lab frame  $z$ - $y$  plane (i.e.  $Z/2R = \cos(\beta)$ ,  $Y/2R = \sin(\beta)\sin(\alpha)$ ) is plotted versus time. Note that in the small angle limit  $Z/2R \approx \eta$ ,  $Y/2R \approx \xi$ ). The particle's tip undergoes fast oscillations enveloped in a slower precession motion about the  $x$ -axis, qualitatively consistent with the dynamics seen in the small angle approximation.

In summary, the nanoparticle oscillates about the polarization axis as a superposition of two precessional modes resulting in a combination of libration and precession motions. The librational motion is due to the laser field's potential while precession arises from the nonzero spin of the nanoparticle about its symmetry axis. The equations of motion describing the location of the tip of the nanoparticle in the small angle approximation are seen to have the same form as a charged particle in a harmonic oscillator potential and a static magnetic field.

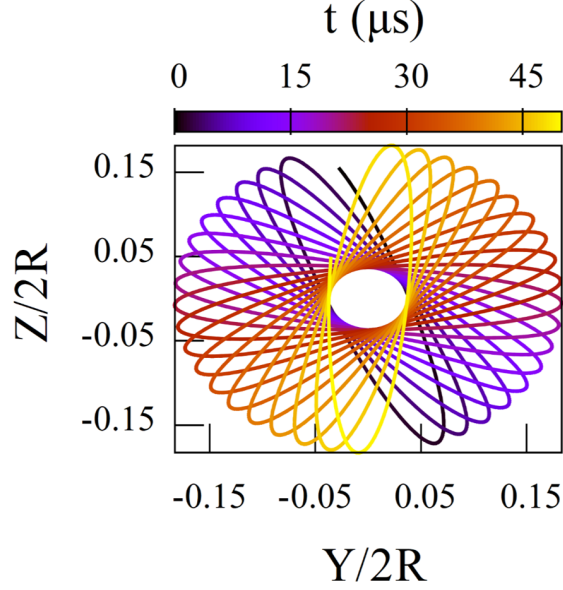


Figure 4.3. Trajectory of the nanoparticle's  $z'''$ -axis, projected on the lab frame  $y$ - $z$  plane found by simulating the full equations of motion and using linear polarization. Here,  $Z/2R = \cos(\beta)$ ,  $Y/2R = \sin(\beta) \sin(\alpha)$  define the location of the  $z'''$ -axis; in the small angle limit  $Z/2R \approx \eta$ ,  $Y/2R \approx \xi$ . The particle's long axis moves in two joint motions, one describing libration and the other describing precession about the polarization axis.

## 4.2 Quantum dynamics

The quantum translational dynamics are fairly straightforward as they describe uncoupled harmonic oscillators in three dimensions. The quantum rotational dynamics of Sec. 4.1 are more interesting due to the combination of precession and libration. This section will investigate the quantum rotational dynamics for linearly polarized light incident on a nanodumbbell in the  $z$ - $y'$ - $z''$  convention. First, the wavefunction will be solved for using the time independent Schrodinger equation. Secondly, the Hamiltonian is composed of cononical variables which allows one to rewrite it in terms of the raising and lowering operators  $a_i^\dagger, a_i$  and transform to a Fock basis  $|n_i, n_j\rangle$ .

The time independent Schrodinger equation is

$$\mathbf{H}\Psi(\alpha, \beta, \gamma) = E\Psi(\alpha, \beta, \gamma) \quad (4.20)$$

with the Hamiltonian  $\mathbf{H} = \mathbf{K}_R + \mathbf{U}_R$ . The rotational kinetic and potential energy are given by [82]

$$\mathbf{K}_R = -\frac{\hbar^2}{2I_x} \left[ \frac{\partial^2}{\partial \beta^2} + \cot(\beta) \frac{\partial}{\partial \beta} + \left( \frac{I_x}{I_z} + \cot^2(\beta) \right) \frac{\partial^2}{\partial \gamma^2} + \frac{1}{\sin^2(\beta)} \frac{\partial^2}{\partial \alpha^2} - \frac{2 \cos(\beta)}{\sin^2(\beta)} \frac{\partial^2}{\partial \alpha \partial \gamma} \right], \quad (4.21)$$

$$\begin{aligned} \mathbf{U}_R &= -\frac{1}{4}(\alpha_z - \alpha_x) E_0^2 \cos^2 \alpha \sin^2 \beta \\ &= -U_0 \cos^2 \alpha \sin^2 \beta. \end{aligned} \quad (4.22)$$

To begin, define the dimensionless quantities  $\varepsilon = -2EI_x/\hbar^2$  and  $W = -2I_x\mathbf{U}_R/\hbar^2 = W_0 \cos^2 \alpha \sin^2 \beta$ . A solution of the form  $\Psi(\alpha, \beta, \gamma) = A(\alpha, \beta)C(\gamma)/\sqrt{\sin \beta} \equiv AC/\sqrt{\sin \beta}$  allows removal of the first derivative of  $\beta$  in Eq. (4.21) and the differential equation becomes

$$\left[ \frac{A_{\beta\beta}}{A} + \frac{1}{2}(\cot^2 \beta + 1) + \frac{C_{\gamma\gamma}}{C} \left( \frac{I_x}{I_z} + \cot^2 \beta \right) + \frac{A_{\alpha\alpha}}{A \sin^2 \beta} - \frac{A_\alpha C_\gamma}{AC} \left( \frac{2 \cos \beta}{\sin^2 \beta} \right) \right] + W = \varepsilon, \quad (4.23)$$

where the notation  $A_\beta$  will stand for the derivative  $\frac{\partial}{\partial \beta} A$  and  $A_{\beta\beta} \equiv \frac{\partial^2}{\partial \beta^2} A$ . Performing the operation  $\frac{\partial^2}{\partial \alpha \partial \gamma}$  to both sides of Eq. (4.23) gives the relation  $\frac{C_\gamma}{C} = \text{const.}$  yielding

$$C(\gamma) = C_0 e^{i\lambda\gamma} \quad (4.24)$$

where  $\lambda = 0, \pm 1, \pm 2, \dots$  is an integer constrained by the condition  $C(\gamma) = C(\gamma + 2\pi)$  and  $C_0$  is a constant. With the  $\gamma$  dependence accounted for, the differential equation may be solved for using the small angle approximation used in Sec. 4.1. Allowing  $\alpha \rightarrow 0 + \xi$ ,  $\beta \rightarrow \frac{\pi}{2} - \eta$  produces to second order

$$\left[ \frac{A_{\eta\eta}}{A} + \frac{A_{\xi\xi}}{A} - 2i\lambda\eta \frac{A_\xi}{A} - \lambda^2 \eta^2 \right] - W_0 (\eta^2 + \xi^2) = \varepsilon - W_0 + \lambda^2 \frac{I_x}{I_z} - \frac{1}{2}. \quad (4.25)$$

Making the gauge transformation  $\Psi'(\xi, \eta, \gamma) \rightarrow \exp(i\lambda\xi\eta/2)\Psi(\xi, \eta, \gamma)$  and inserting into Eq. (4.25) brings

$$\left[ \frac{\partial^2}{\partial \eta^2} + \frac{\partial^2}{\partial \xi^2} \right] + i\lambda \left( \xi \frac{\partial}{\partial \eta} - \eta \frac{\partial}{\partial \xi} \right) - \left( W_0 + \frac{\lambda^2}{4} \right) (\xi^2 + \eta^2) = \varepsilon - W_0 + \lambda^2 \frac{I_x}{I_z} - \frac{1}{2}, \quad (4.26)$$

which we rewrite as

$$\left(\frac{\hat{p}_\eta^2 + \hat{p}_\xi^2}{2I_x}\right) + \left(\frac{\lambda\hbar}{2I_x}\right)\hat{L}_x + \bar{U}_0(\xi^2 + \eta^2) = (\varepsilon_0 - \varepsilon_\gamma), \quad (4.27)$$

which has the familiar form of a harmonically trapped charged particle in a static magnetic field. Comparing Eqs. (4.26) and (4.27), it is visible that  $\hat{p}_\eta = -i\hbar\frac{\partial}{\partial\eta}$  plays the role of the momentum in  $\eta$  (similarly for  $\xi$ ),  $\hat{L}_x = -i\hbar\left(\xi\frac{\partial}{\partial\eta} - \eta\frac{\partial}{\partial\xi}\right)$  is the angular momentum about the  $x$ -axis,  $\bar{U}_0 = U_0 + \lambda^2\hbar^2/(8I_x)$  is a shifted harmonic potential energy, and the constants  $\varepsilon_0 = E + U_0$  and  $\varepsilon_\gamma = \frac{\hbar^2}{2I_x}\left(\lambda^2\frac{I_x}{I_z} - \frac{1}{2}\right)$  determine the total energy and energy associated with the spin  $\gamma$ .

To complete the solution to Eq. (4.26) it is easiest to move to polar coordinates with  $\xi = \rho \cos \phi$ ,  $\eta = \rho \sin \phi$ ,  $\rho^2 = \eta^2 + \xi^2$ ,  $\phi = \arctan(\eta/\xi)$ , and  $\hat{L}_x = -i\hbar\frac{\partial}{\partial\phi}$ . The ansatz  $A(\xi, \eta) \rightarrow A(\rho, \phi) = \exp(im\phi)R(\rho)/\sqrt{\rho}$  reveals  $m = 0, \pm 1, \pm 2, \dots$  as an integer and Eq. (4.26) becomes

$$-\frac{\hbar^2}{2I_x}\left[\frac{R_{\rho\rho}}{R} - \frac{1}{\rho^2}\left(m^2 - \frac{1}{4}\right) - \lambda m\right] + \bar{U}_0\rho^2 = (\varepsilon_0 - \varepsilon_\gamma). \quad (4.28)$$

The differential equation is now fully determined by the solution for  $R(\rho)$ . The solution is found with  $R(\rho) = \rho^{|m|+1/2}\exp(-\rho^2q/2)L_j^{(|m|)}(\rho^2q)$  where  $q^2 = 2\bar{U}_0I_x/\hbar^2$  and  $L_n^k(x)$  is the associated Laguerre polynomial. The complete, normalized wavefunction and eigenenergies in the small angle approximation are

$$\Psi'_{j,m,\lambda}(\rho, \phi, \gamma) \approx \sqrt{\frac{q}{\pi}} \frac{j!}{(j+|m|)!} e^{i\lambda(\gamma+\rho^2\sin(2\phi)/4)} e^{im\phi} (\rho^2q)^{|m|/2} e^{-\rho^2q/2} L_j^{(|m|)}(\rho^2q). \quad (4.29)$$

$$E = \left(\frac{\hbar^2}{2I_x}\right) \left[\lambda\left(\lambda\frac{I_x}{I_z} + m\right) - \frac{1}{2}\right] + \hbar\bar{\omega}(1 + |m| + 2j) - U_0 \quad (4.30)$$

$$\lambda = 0, \pm 1, \pm 2, \pm 3, \dots \quad m = 0, \pm 1, \pm 2, \pm 3, \dots \quad j = 0, 1, 2, 3, \dots \quad (4.31)$$

where the frequency  $\bar{\omega} = \left(\frac{2U_0}{I_x} + \left(\frac{\lambda\hbar}{2I_x}\right)^2\right)^{1/2}$ . The integers  $j, m, \lambda$  are the quantum numbers associated with the coordinates  $\rho, \phi, \gamma$ , respectively. Noting that  $L_z = \hbar\lambda$

while  $\omega^2 = 2U_0/I_x = \frac{1}{2}(\alpha_z - \alpha_x)E_0^2/I_x$  and  $\omega_c = L_z/I_x$  from the previous section we can reexamine Eq. (4.30) after neglecting the constant factors,

$$\begin{aligned} E &= \frac{L_z^2}{2I_z} + \hbar \left[ \bar{\omega} (|m| + 2j) + \frac{m\omega_c}{2} \right] \\ &= \frac{L_z^2}{2I_z} + \hbar |m| \left[ \left( \omega^2 + \frac{\omega_c^2}{4} \right)^{1/2} \pm \frac{\omega_c}{2} \right] + 2\hbar \bar{\omega} j \\ &= \frac{L_z^2}{2I_z} + \hbar |m| \omega_{\pm} + 2\hbar \bar{\omega} j \end{aligned} \quad (4.32)$$

Equation (4.32) shows the energy of the particle while trapped in the linearly polarized beam broken into familiar analogues from the previous section where the classical dynamics were explored. The first term is the kinetic energy due to the spin about the particle's symmetry axis. Comparing with the normal mode frequencies found in Eqs. (4.18) and (4.19)  $\omega_{\pm} = \sqrt{\omega^2 + \omega_c^2/4} \pm \omega_c/2$ , the second term shows oscillations in the  $\phi$  coordinate which accounts for precession about the laser polarization axis. The last term shows simple harmonic motion for the two coordinates  $\eta, \xi$  with equal frequencies of rotation, equivalent to libration.

It is also possible to recast the problem in a Fock basis  $|n_i, n_j\rangle$  with the Hamiltonian in terms of raising and lowering operators. Introducing the raising and lowering operators

$$a_j = \left( \sqrt{\frac{I_x \bar{\omega}}{2\hbar}} x_j + \frac{ip_j}{\sqrt{2I_x \bar{\omega} \hbar}} \right), \quad a_j^\dagger = \left( \sqrt{\frac{I_x \bar{\omega}}{2\hbar}} x_j - \frac{ip_j}{\sqrt{2I_x \bar{\omega} \hbar}} \right), \quad (4.33)$$

$$(4.34)$$

$$x_j = \sqrt{\frac{\hbar}{2\bar{\omega} I_x}} (a_j + a_j^\dagger), \quad p_j = i\sqrt{\frac{I_x \bar{\omega} \hbar}{2}} (a_j^\dagger - a_j) \quad (4.35)$$

where the subscript  $j = (\xi, \eta)$  as well as  $x_j = (\xi, \eta)$  and  $p_j = (I_x \dot{\xi}, I_x \dot{\eta})$ . Using Eq. (4.26), the Hamiltonian transforms to

$$\mathbf{H} = \hbar \bar{\omega} \left[ a_\xi^\dagger a_\xi + a_\eta^\dagger a_\eta + 1 \right] + \left( \frac{i\lambda \hbar^2}{4I_x} \right) \left[ \{a_\xi, a_\eta^\dagger\} - \{a_\eta, a_\xi^\dagger\} \right] \quad (4.36)$$

with  $\{A, B\}$  denoting the anti-commutator. Further transforming into the mode basis  $|n_+, n_-\rangle$  through the mode raising and lowering operators

$$a_{\pm} = \frac{1}{\sqrt{2}} (a_{\xi} \pm ia_{\eta}), \quad a_{\pm}^{\dagger} = \frac{1}{\sqrt{2}} (a_{\xi} \mp ia_{\eta}) \quad (4.37)$$

$$a_{\xi} = \frac{1}{\sqrt{2}} (a_+ + a_-), \quad a_{\xi}^{\dagger} = \frac{1}{\sqrt{2}} (a_+^{\dagger} + a_-^{\dagger}) \quad (4.38)$$

$$a_{\eta} = \frac{i}{\sqrt{2}} (a_- - a_+), \quad a_{\eta}^{\dagger} = \frac{-i}{\sqrt{2}} (a_+^{\dagger} - a_-^{\dagger}) \quad (4.39)$$

$$(4.40)$$

returns the Hamiltonian

$$\mathbf{H} = \hbar\bar{\omega} [a_+^{\dagger}a_+ + a_-^{\dagger}a_- + 1] + \left(\frac{\lambda\hbar^2}{2I_x}\right) [a_-^{\dagger}a_- - a_+^{\dagger}a_+], \quad (4.41)$$

with energy eigenvalues

$$\begin{aligned} \mathbf{H}|n_+, n_-\rangle &= \left[ \hbar\bar{\omega} (n_+ + n_- + 1) + \left(\frac{\lambda\hbar^2}{2I_x}\right) (n_- - n_+) \right] |n_+, n_-\rangle \\ &= (\varepsilon_0 - \varepsilon_{\gamma}) |n_+, n_-\rangle. \end{aligned} \quad (4.42)$$

Comparing Eq. (4.42) with Eq. (4.30) shows the relation between the wavefunction in the position basis and the states in the  $|n_+, n_-\rangle$  representation by finding  $n_+ + n_- = |m| + 2j$  and  $m = n_- - n_+$ . These relations show that the  $n_{\pm}$  modes represent the precessional modes found in Sec. 4.1. The two modes compete with one another as the (+) advances clockwise around the polarization axis and the (-) counterclockwise. If each mode has equal energy,  $m = 0$ , resulting in no precession and pure libration. Alternatively, if one mode has no energy, say  $n_+ = 0$ , then  $m = n_-$  and the relation  $n_+ + n_- = |m| + 2j$  requires  $j = 0$ , resulting in pure precession.

### 4.3 Measuring the particle orientation

It is possible to determine the orientation of the nanoparticle with respect to  $\alpha$  and  $\beta$  through different types of measurements. A common method of measuring  $\alpha$  libration [54,56,83,84] is to first send the forward scattered light from the nanoparticle

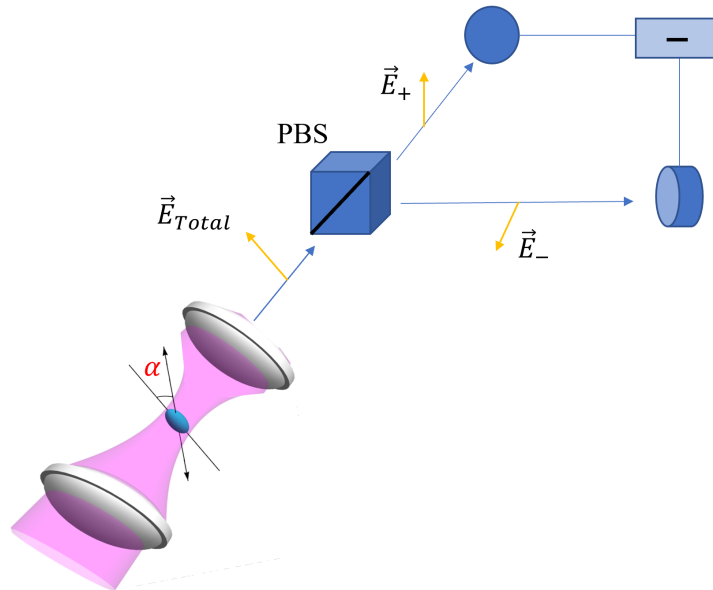


Figure 4.4. Illustration of the measurement procedure for measuring the orientation. A Gaussian beam is incident upon a symmetric-top particle at an angle  $\alpha$  with respect to the polarization axis. The scattered light and outgoing laser light interfere to produce a total electric field  $E_{total}$ . The signal then enters a polarized beam splitter where it is split into two polarizations  $E_+$  and  $E_-$ . The two signals exiting the beam splitter are incident upon their respective detectors and are subtracted from one another to obtain a signal proportional to the angle  $\alpha$ .

and the laser beam through a  $45^\circ$  polarized beamsplitter (PBS). The light exits the PBS in two different directions with orthogonal polarizations. A measurement is obtained by reading the signal of each polarization state on a photodetector and taking the difference between the two signals. The illustration of this procedure is depicted in Fig. 4.4. This section will demonstrate the validity of this measurement procedure in its ability to measure an angle of libration as well as calculate a possible method for measuring the second angle of libration. The method follows similarly to that of Sec. 3.3. The derivation was first seen in our paper in Ref. [76].

To determine what is measured in the above procedure, consider a Gaussian laser beam incident on the dumbbell from Eq. (3.1) in Sec. 3.1. The scattered light is

again determined by the electric and magnetic fields for a dipole in the far field (Sec. 2.2)

$$\vec{H}_p = \frac{ck^2}{4\pi} (\hat{r} \times \vec{p}) \frac{e^{ikr}}{r}, \quad (4.43)$$

$$\vec{E}_p = Z_0 \vec{H} \times \hat{r}, \quad (4.44)$$

where  $\vec{r}$  is in the direction of observation and  $\vec{p}$  is given by Eq. (4.3). After exiting a collimating lens [66], the light is split by a 45° PBS. The transverse components of the electric field exiting the PBS are

$$\vec{E}_+(x, y) = \frac{1}{\sqrt{2}} (E_x(x, y) + E_y(x, y)) \hat{e}_+, \quad (4.45)$$

$$\vec{E}_-(x, y) = \frac{1}{\sqrt{2}} (E_y(x, y) - E_x(x, y)) \hat{e}_-, \quad (4.46)$$

where  $E_{x,y}$  are the  $x$  and  $y$  components of the total electric field following the collimating lens and  $\hat{e}_\pm$  designate the two split polarization states after the PBS. The magnetic field undergoes a similar transformation. A measurement is performed by taking the difference between the two signals measured at their respective detectors

$$P_{45^\circ} = \int_{-\infty}^{\infty} \int_{-\infty}^{\infty} (\vec{S}_+ \cdot \hat{z} - \vec{S}_- \cdot \hat{z}) dy dx, \quad (4.47)$$

where  $\vec{S}_\pm = \frac{1}{2} \text{Re}[\tilde{\vec{E}}_\pm \times \tilde{\vec{H}}_\pm^*]$  is the Poynting vector. Performing the integration gives a homodyne term that is proportional to the  $y$ -component of the polarizability from Eq. (4.3)

$$P_{45^\circ} \propto p_y \propto \sin^2(\beta) \cos(\alpha) \sin(\alpha). \quad (4.48)$$

Considering that the particle undergoes small oscillations the small angle approximation may be made,  $\alpha \rightarrow 0 + \xi$  and  $\beta \rightarrow \frac{\pi}{2} - \eta$ ,

$$p_y \propto \cos^2(\eta) \cos(\xi) \sin(\xi) \approx \xi, \quad (4.49)$$

which is the angle describing the extent to which the nanoparticle's long axis has deviated from the polarization axis in the  $x$ - $y$  plane.

It is also (theoretically) possible to measure the other angle of libration  $\eta$ . A second transverse laser perpendicular from the first may be used using the same procedure

above, or, instead, using the split detection measurement (the method used to track the transverse translational motion in Sec. 3.3). Following the collimating lens, the split detection measurement is performed and the homodyne term is examined

$$P_x = \int_0^\infty \int_{-\infty}^\infty (\vec{S} \cdot \hat{z}) dydx - \int_{-\infty}^0 \int_{-\infty}^\infty (\vec{S} \cdot \hat{z}) dydx \quad (4.50)$$

$$\propto p_z \propto \cos(\beta) \sin(\beta) \cos(\alpha) \approx \eta,$$

which is the angle describing the extent to which the nanoparticle's long axis has deviated from the polarization axis in the  $x$ - $z$  plane. Thus, both angles can be detected. Note that it is not possible to measure  $\gamma$  directly using these methods since it is not contained within the polarization vector in Eq. (4.3).

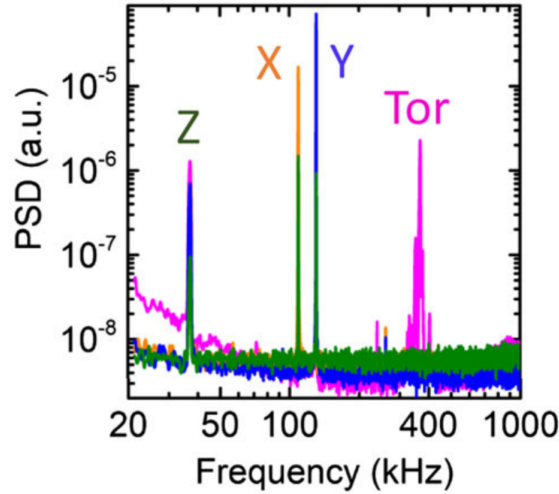


Figure 4.5. Power spectral density of a nanodumbbell's measured position and orientation (labeled *Tor*, standing for torsional motion, in the figure) [56].

Interestingly, whereas the detection of translational motion relies on the  $\pi/2$  Gouy phase shift from  $\psi(z)$  in Eq. (3.1) [75], for a nanoparticle centered at the origin, the Gouy phase shift hinders detection of rotational motion. The homodyne terms in the Poynting vector evaluated far from the nanoparticle are left purely imaginary

and require the imaginary part of the polarizability for orientational detection. The imaginary part of the polarizability is usually smaller than the real part [59, 60] for the types of particles used in levitated optomechanics and is two orders of magnitude smaller for a  $R = 85$  nm amorphous silica dumbbell in a  $\lambda = 1550$  nm laser field.

However, the signal may become real, and therefore larger in magnitude, if the particle is not centered at the origin, but pushed away from the focus by the laser beam in the axial direction through radiation pressure. Section 3.2 estimated the magnitude of this displacement to be approximately  $z_d/z_R \sim 0.1$  for a silica sphere. For a nanodumbbell with the same parameters,  $z_d/z_R \sim 0.14$ . This ratio becomes important for measurements as  $e^{iz_d/z_R} \sim (1 + iz_d/z_R)$  is a prefactor in the polarizability matrix when considering  $\psi(z)$  in Eq. (3.1), effectively reducing the measured signal by this ratio.

## 5. DAMPING AND NOISE

The analyses thus far have neglected sources of noise and damping. However, real experiments encounter unavoidable laser shot noise, gas collisions, measurement uncertainty, experimental noise, decoherence due to blackbody radiation, among others, for both translations and rotations. This section describes the effects of two of the most important environmental considerations for a particle trapped in the focus of a laser beam: gas collisions and laser shot noise.

### 5.1 Gas collisions

The gas molecules scattering off of a levitated nanoparticle has been studied extensively [19, 26, 85, 86]. Collisions of a particle with the surrounding gas can be described with the Langevin equations [19, 87, 88]

$$\dot{v}_i(t) \propto -\Gamma_i v_i(t) + \zeta_i(t), \quad (5.1)$$

$$\dot{\pi}_i(t) \propto -\Gamma_i \pi_i(t) + \Upsilon_i(t), \quad (5.2)$$

where  $v_i = (\dot{x}, \dot{y}, \dot{z})$ ,  $\pi_i = (\dot{\alpha}, \dot{\beta}, \dot{\gamma})$ ,  $\Gamma_i$  is the damping rate, and  $\zeta(t)$  and  $\Upsilon_i(t)$  are Wiener processes (stochastic noise). Equations (5.1) and (5.2) describe Brownian motion with mean reversion around zero. The first term provides frictional damping and the second gives force fluctuations due to scattering with the surrounding air molecules. As the gas is composed of free atoms at temperature  $T$ , they obey a Maxwell-Boltzmann distribution. With the scattering assumed uncorrelated,  $\zeta(t)$  is a Gaussian random number with a mean of zero and standard deviation  $\sqrt{2k_B T \Gamma / M dt}$ , where  $dt$  is a step in time.  $\Upsilon_i(t)$  similarly has a mean of zero and standard deviation  $\sqrt{2k_B T \Gamma / I_i dt}$  with  $I_i$  the moment of inertia.

At ambient pressures, the particle dynamics are dominated by these forces. For a sphere with radius  $R$  and density  $\rho$  in a rarefied gas is [39, 89]

$$\Gamma = \frac{6\pi\eta R}{\rho \left(\frac{4}{3}\pi R^3\right)} \frac{0.619}{0.619 + \text{Kn}} (1 + c_K), \quad (5.3)$$

where  $\eta$  is the viscosity of air,  $\text{Kn} = s/R$  is the Knudsen number with  $s$  the mean free path of air, and  $c_K = 0.31\text{Kn}/(0.785 + 1.152\text{Kn} + \text{Kn}^2)$ . From pressures of 760, 1, and  $10^{-3}$  Torr the damping is of the order  $10^3$ ,  $10^1$ , and  $10^0$  Hz for a micron sized sphere [22]. As the pressure in the vacuum chamber decreases  $< \sim 1$  Torr, the collisions become less frequent and less of an influence on the nanoparticle [23]. At low pressures where  $\text{Kn} \gg 1$ , the damping is proportional to pressure. The surrounding environment is then described by the free molecular flow regime [5, 56, 85, 90].

## 5.2 Translational shot noise

A particle trapped in the focus of a laser experiences continual scattering from the incident photons which results in radiation pressure as well as motional heating. The effect of radiation pressure was calculated in previous sections. Motional heating due to photon scattering is called shot noise heating and affects the translational dynamics as well as the rotational dynamics for a nonspherical particle. As the field of levitated optomechanics nears an era where nanoparticles are able to be cooled near their motional ground state [31, 33, 34, 91], the effects of heating and noise become essential to understand and quantify. Whereas heating and damping from the surrounding gas may become a negligible effect for sufficiently low pressures, laser shot noise is an inescapable factor of consideration for particles with low motional occupation numbers. This section gives a detailed description of the phenomenon of laser shot noise heating for various scenarios in levitated optomechanics and can also be found in our paper [92].

### 5.2.1 Semi-classical Rayleigh shot noise

The derivation of the translational shot noise follows from Ref. [93] which was originally calculated for atoms in a far red-detuned dipole trap. Consider the scattering of a single photon with wavenumber  $\vec{k}_i = k\hat{k}_i$  off a particle with initial momentum  $m\vec{v}_i$ . In the regime  $|\vec{v}_i| \ll c$ , after the scattering event the photon has final momentum  $\hbar\vec{k}_f \approx (\hbar k)\hat{k}_f$  and the particle has final momentum  $m\vec{v}_f$ . From conservation of momentum,

$$\vec{v}_f = \vec{v}_i + \frac{\hbar}{m} (\vec{k}_i - \vec{k}_f). \quad (5.4)$$

The change in energy for the component  $j = (x, y, z)$  is

$$\begin{aligned} \Delta E_j &= \frac{1}{2}m (v_{fj}^2 - v_{ij}^2) \\ &= \varepsilon \left( \hat{k}_{ij}^2 + \hat{k}_{fj}^2 - 2\hat{k}_{ij}\hat{k}_{fj} \right) + \hbar k \left( \hat{k}_{ij} - \hat{k}_{fj} \right) v_{ij}, \end{aligned} \quad (5.5)$$

with  $\varepsilon = \frac{\hbar^2 k^2}{2m}$ . The change in energy of the particle then depends on the initial photon propagation direction  $\hat{k}_i$  as well as the scattered direction  $\hat{k}_f$ . The above equations are accurate for a free particle, but are also valid for harmonically bound particles if the scattering takes place on time scales much shorter than the oscillation frequency.

The probability for the photon to scatter into a solid angle  $d\Omega$  is

$$P(\hat{k}_f)d\Omega = \frac{1}{\sigma} \left( \frac{d\sigma}{d\Omega} \right) d\Omega, \quad (5.6)$$

where  $d\sigma/d\Omega$  is the differential scattering cross section for the particle and  $\int P(\hat{k}_f)d\Omega = 1$ . The average change in energy  $\langle \Delta E_j \rangle$  of the particle following the scattering event is found through

$$\langle \Delta E_j \rangle = \int_{\Omega} P(\hat{k}_f) \Delta E_j d\Omega. \quad (5.7)$$

To evaluate Eq. (5.7), the particle is taken to be a sphere that is oscillating in a harmonic potential. The incident photon is traveling in the  $\hat{k}_i = \hat{z}$  direction and polarized in the  $\hat{E}_{\text{inc}} = \hat{x}$  direction. Immediately, the contribution from the last term in Eq. (5.5) goes to zero,  $\langle \hbar k (\hat{k}_{ij} - \hat{k}_{fj}) v_{ij} \rangle = 0$ , since  $\langle \vec{v} \rangle = 0$  for harmonic

oscillation. Looking at the change in energy in each direction explicitly, Eq. (5.7) is rewritten as

$$\langle \Delta E_x \rangle = \varepsilon \int_{\Omega} P(\hat{k}_f) (\sin \theta \cos \phi)^2 d\Omega, \quad (5.8a)$$

$$\langle \Delta E_y \rangle = \varepsilon \int_{\Omega} P(\hat{k}_f) (\sin \theta \sin \phi)^2 d\Omega, \quad (5.8b)$$

$$\langle \Delta E_z \rangle = \varepsilon \int_{\Omega} P(\hat{k}_f) (1 - \cos \theta)^2 d\Omega, \quad (5.8c)$$

where spherical coordinates were used to define the outgoing wave,  $\hat{k}_{fx} = \sin \theta \cos \phi$ ,  $\hat{k}_{fy} = \sin \theta \sin \phi$ ,  $\hat{k}_{fz} = \cos \theta$ . To complete Eq. (5.8) the differential scattering cross section for the particle must be determined. In the subsections below the energy delivered to a particle in the Rayleigh and Mie regimes are computed. Note that from Eq. (5.8) the total energy delivered to a particle

$$\langle \Delta E \rangle = \sum_j \langle \Delta E_j \rangle = 2\varepsilon \left( 1 - \int_{\Omega} P(\hat{k}_f) \cos \theta d\Omega \right), \quad (5.9)$$

is always greater than zero with a maximum of  $4\varepsilon$ .

### 5.2.2 Rayleigh shot noise heating rate

For an incident monochromatic plane wave polarized in the  $\hat{E}_{\text{inc}} = \hat{x}$  direction, the differential scattering cross section for a dipole with moment  $\vec{p} = \alpha \vec{E}_{\text{inc}}$ , index of refraction  $n$ , and radius  $r$  in the Rayleigh regime  $kr|n - 1| \ll 1$  is (Sec. 2.4 )

$$\left( \frac{d\sigma}{d\Omega} \right) = \left( \frac{k^2 \alpha}{4\pi \epsilon_0} \right)^2 \sum_j |\hat{\xi}_j \cdot \hat{E}_{\text{inc}}|^2, \quad (5.10)$$

yielding

$$P(\hat{k}_f) = \left( \frac{3}{8\pi} \right) [\cos^2 \theta \cos^2 \phi + \sin^2 \phi], \quad (5.11)$$

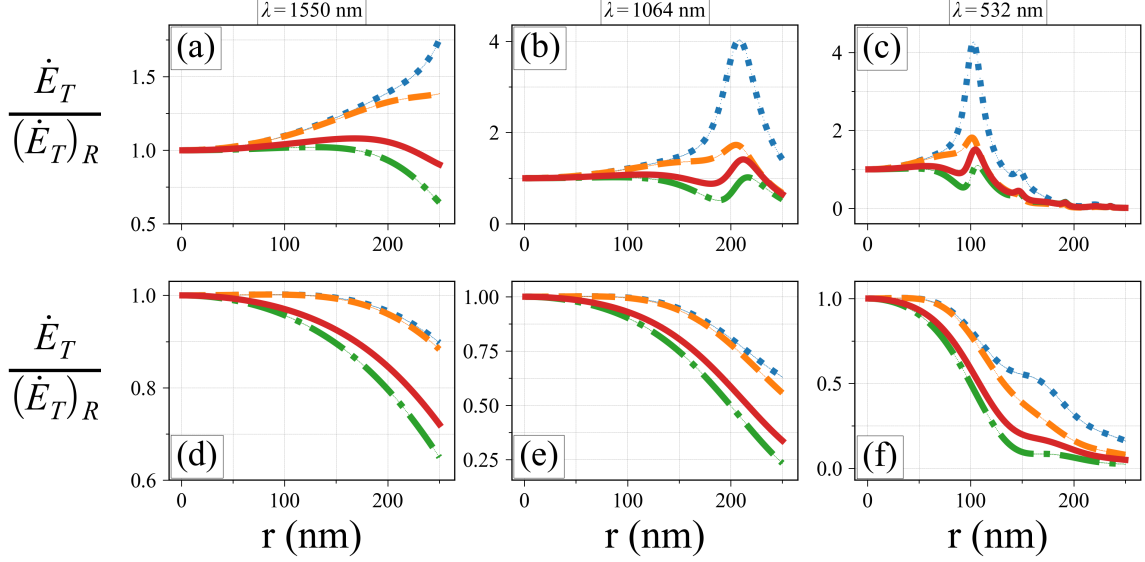


Figure 5.1. Shot noise heating rate for each degree of freedom relative to the rate in the Rayleigh limit for diamond at laser wavelength (a)  $\lambda = 1550$  nm (b)  $\lambda = 1064$  nm (c)  $\lambda = 532$  nm and silica at wavelength (d)  $\lambda = 1550$  nm (e)  $\lambda = 1064$  nm (f)  $\lambda = 532$  nm. For each plot, the relative heating rate is shown for the  $x$  (blue dotted line),  $y$  (orange dashed line), and  $z$  (green dot-dashed line) degree of freedom, as well as the total heating rate (red solid line). Here, the incident plane wave is polarized in the  $x$  and traveling in the  $z$  direction. The relative heating rate is reduced in each degree of freedom for silica. The non-linear behavior of Mie scattering can be seen near  $r = 200$  nm in diamond with a resonance occurring at  $\lambda = 1064$  nm. The index of refraction for silica is  $n_s = 1.45$  for  $\lambda = 1550$  nm and  $\lambda = 1064$  nm while  $n_s = 1.46$  for  $\lambda = 532$  nm. The index of refraction for diamond is  $n_d = 2.39$  for  $\lambda = 1550$  nm and  $\lambda = 1064$  nm while  $n_d = 2.425$  for  $\lambda = 532$  nm.

where  $\epsilon_0$  is the permittivity of free space and  $\hat{\xi}_j(\hat{k}_f)$  defines the two orthogonal polarization directions of the scattered light perpendicular to  $\hat{k}_f$  so that  $\sum_j |\hat{\xi}_j(\hat{k}_f) \cdot \hat{E}_{\text{inc}}|^2 = 1 - |\hat{k}_f \cdot \hat{E}_{\text{inc}}|^2$ . Note that probability densities of the form Eq. (5.11) have the property  $P(\hat{k}_f) = P(-\hat{k}_f)$ .

Inserting Eq. (5.11) into Eq. (5.8) gives the distribution of energy delivered to the particle

$$\left( \langle \Delta E_x \rangle_R, \langle \Delta E_y \rangle_R, \langle \Delta E_z \rangle_R \right) = \epsilon \left( \frac{1}{5}, \frac{2}{5}, \frac{7}{5} \right), \quad (5.12)$$

where the subscript  $R$  refers to Rayleigh scattering. Thus, the scattering of one photon in the Rayleigh limit increases the particle's total energy by  $\langle \Delta E \rangle_R = \sum_j \langle \Delta E_j \rangle_R = 2\epsilon$  half the maximum amount possible and in different proportions in each direction. The particle gains 7/10 of the total energy in the direction of photon propagation, 1/10 of the total energy in the photon polarization direction, and 2/10 in the remaining direction. For unpolarized light, the total energy increase is the same as for linearly polarized light  $\langle \Delta E \rangle_R = 2\epsilon$ . However, the energy is distributed as 14/20 of the total energy in the direction of photon propagation and 3/20 of the total energy in each of the directions perpendicular to the photon propagation direction.

The previous calculation shows how the energy is distributed to each degree of freedom. The average rate at which energy is being delivered to these degrees of freedom  $\dot{E}_T$  (shot noise heating rate) is the change in energy per scattering event multiplied by the scattering rate. The scattering rate is the number of incident photons per unit area per unit time,  $J_p = I_0/\hbar\omega$ , times the scattering cross section,  $\sigma$ ,

$$\dot{E}_{TR} = \langle \Delta E \rangle_R J_p \sigma. \quad (5.13)$$

For Rayleigh particles,  $\sigma_R = \left(\frac{8\pi}{3}\right) \left(\frac{\alpha k^2}{4\pi\epsilon_0}\right)^2$ .  $\dot{E}_{TR}$  is the total translational energy gained per second due to shot noise. This is written in many forms in the literature, but often in terms of the scattered power  $\dot{E}_{TR} = \hbar\omega_0 P_{\text{scatt}}/mc^2$  with  $\omega_0 = ck$  the frequency of the laser.

If the particle oscillates at frequency  $\omega_j$  in the  $j$ th direction, each degree of freedom's occupation number increases at a rate of

$$\Gamma_x = \frac{1}{10} \frac{\dot{E}_{TR}}{\hbar\omega_x}, \quad \Gamma_y = \frac{2}{10} \frac{\dot{E}_{TR}}{\hbar\omega_y}, \quad \Gamma_z = \frac{7}{10} \frac{\dot{E}_{TR}}{\hbar\omega_z}. \quad (5.14)$$

Reference [94] experimentally measured the shot noise heating rate in the degree of freedom perpendicular to both the laser propagation and polarization directions. The measured value for the degree of freedom was reported to be within error bars of the expression in Eq. (5.14). (Quick note: their expression for the two directions

perpendicular to the laser propagation direction,  $\hat{k} = \hat{z}$ , are correct, while the total energy and proportionality constant for the  $z$  degree of freedom is not. )

### 5.2.3 Quantum Rayleigh shot noise heating rate

Although the results are equivalent, it is instructive to calculate the Rayleigh shot noise quantum mechanically. The model used to calculate the shot noise describes particle state decoherence due to scattering events with photons [3]. The decoherence in the system state generates diffusion in momentum space which leads to heating.

The system is the same as that considered above with the incident plane wave propagating in the  $\hat{z}$  and polarized in the  $\hat{x}$  direction. The particle density matrix  $\rho(\vec{r}, \vec{r}')$  is written in the position basis with  $\vec{r} = (x, y, z)$ . The state  $\vec{r}$  refers to the system before a scattering event and the primed coordinates refer to the system following a scattering event. Neglecting the unitary part of the time evolution the translational master equation reads

$$\partial_t \rho(\vec{r}, \vec{r}') = -\Lambda(\vec{r}, \vec{r}') \rho(\vec{r}, \vec{r}'), \quad (5.15)$$

where the decoherence rate  $\Lambda(\vec{r}, \vec{r}')$  to first order and neglecting cross terms which do not contribute to heating is

$$\Lambda(\vec{r}, \vec{r}') = D_x (x - x')^2 + D_y (y - y')^2 + D_z (z - z')^2, \quad (5.16)$$

but with separate diffusion constants [95]

$$D_j = J_p \int d^3 \vec{k} \mu(\vec{k}) \int d^2 \hat{k} |f(\vec{k}, \vec{k}')|^2 \frac{k^2}{2} |\hat{k} - \hat{k}'|^2, \quad (5.17)$$

where  $|f(\vec{k}, \vec{k}')|$  is the scattering amplitude and  $\mu(\vec{k}) = \delta(\vec{k} - \vec{k}')$  is the distribution of the laser which may safely be taken to be a  $\delta$  function. The shot noise heating rate may be calculated through

$$\dot{E}_T = \frac{d}{dt} \langle \mathbf{H} \rangle = \text{Tr}(\mathbf{K} \partial_t \rho), \quad (5.18)$$

with  $\mathbf{H} = \mathbf{K} + \mathbf{U}$  the translational Hamiltonian,  $\mathbf{U}$  the potential energy whose term vanishes after carrying out the trace, and  $\mathbf{K} = \mathbf{P}^2/2m$  is the kinetic energy. Combining Eqs. (5.15) through (5.17) and inserting into Eq. (5.18)

$$\dot{E}_{Tx} = J_p \frac{\hbar^2 k^2}{2m} \int d^2 \hat{k} |f(\vec{k}, \vec{k}')|^2 \left( \hat{k}_x'^2 \right), \quad (5.19a)$$

$$\dot{E}_{Ty} = J_p \frac{\hbar^2 k^2}{2m} \int d^2 \hat{k} |f(\vec{k}, \vec{k}')|^2 \left( \hat{k}_y'^2 \right), \quad (5.19b)$$

$$\dot{E}_{Tz} = J_p \frac{\hbar^2 k^2}{2m} \int d^2 \hat{k} |f(\vec{k}, \vec{k}')|^2 \left( \hat{k}_z^2 + \hat{k}_z'^2 - 2\hat{k}_z \hat{k}_z' \right). \quad (5.19c)$$

Noting that  $|f(\vec{k}, \vec{k}')|^2 = d\sigma/d\Omega$  and  $\varepsilon = \frac{\hbar^2 k^2}{2m}$ , Eqs. (5.19) are equal to Eqs. (5.8) and (5.13) in Sec. 5.2.1.

#### 5.2.4 Mie scattering

The analytical expressions in the previous subsection are valid for small particles  $kr|n-1| \ll 1$ . For particles outside the Rayleigh regime  $kr|n-1| \sim 1$  the differential scattering cross section in Eq. (5.10) and therefore Eq. (5.11) breaks down and Mie scattering [51] must be used to calculate the shot noise heating. Figure 5.1 plots the translational shot noise heating rate  $\dot{E}_T$  for each degree of freedom for varying particle radii using analytical Mie formulas. Specifically,  $\dot{E}_{Tj}/J_p = \langle \Delta E_j \rangle \sigma$  for each degree of freedom is found by numerically calculating the differential scattering cross section and numerically integrating Eqs. (5.8). These quantities are then divided by their respective Rayleigh expression,  $(\dot{E}_{Tj})_R/J_p = \langle \Delta E_j \rangle_R \sigma_R$ .

For particle sizes  $r \leq 50$  nm, Fig. 5.1 shows that the total shot noise heating rate may still be approximated as the Rayleigh expression to better than 10% error for both silica ( $n_s = 1.45$ ) and diamond ( $n_d = 2.39$ ) at a wavelength of  $\lambda = 1064$  nm or  $\lambda = 1550$  nm. For larger particle sizes, the non-sextic behavior of the differential scattering cross section with respect to the radius becomes more apparent. As expected, deviations from the Rayleigh approximation become more significant as  $kr|n-1|$  approaches unity with smaller wavelengths producing the most considerable change for both materials. For diamond, there is a resonance in the scattering near  $r \sim 200$  nm

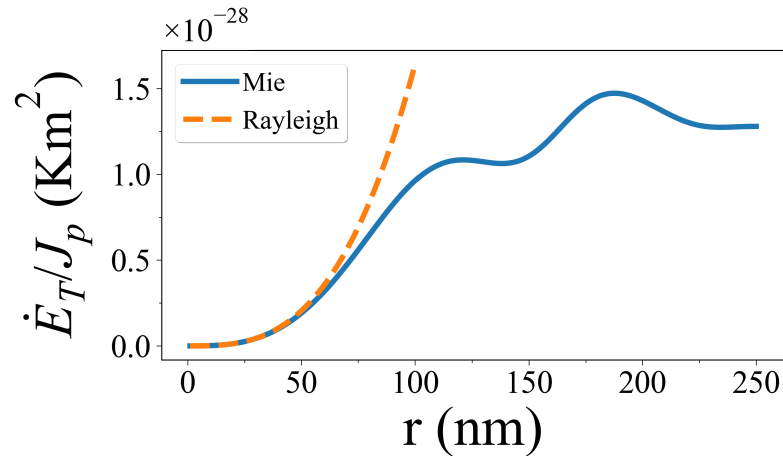


Figure 5.2. Comparison of the total shot noise heating rate using Mie and Rayleigh scattering for a silica nanoparticle ( $n_s = 1.46$  for  $\lambda = 532$  nm) under plane wave illumination. For radii  $r < 50$  nm the Mie calculation shares the same  $r^3$  dependence as the Rayleigh expression. For larger radii, the non-linear Mie calculation yields significantly less total heating.

for  $\lambda = 1064$  nm and a two order of magnitude suppression near  $r \sim 250$  nm for  $\lambda = 532$  nm.

For  $\lambda = 1550, 1064$ , and  $532$  nm, the shot noise heating rate for silica is decreased for each degree of freedom relative to the Rayleigh expression. From Fig. 5.1(f), the heating rate is almost an order of magnitude lower for  $\lambda = 532$  nm near  $r = 200$  nm. The reduction in heating as the radius increases and wavelength decreases is due to the reduction in cross section compared to the Rayleigh expression. Figure 5.2 shows the explicit dependence of  $r$  on the heating rate for silica at  $\lambda = 532$  nm compared with the  $r^3$  dependent Rayleigh expression. Here one can clearly see the range of accuracy of the Rayleigh approximation with the Mie calculation strongly deviating above  $r \sim 75$  nm. The reduction in heating is also attributed to the differential scattering cross section giving increasingly more forward scattering, thereby reducing the recoil impact on the scatterer.

In Ref. [96] the laser shot noise was calculated for a  $r = 230$  nm silica nanoparticle illuminated with a  $\lambda = 532$  nm laser. If their shot noise heating rate was calculated

using the Rayleigh expression, Fig. 5.1(f) shows that that estimate should be reduced by  $\sim 10$  times the calculated value, making laser shot noise an even less significant noise source for their experiment.

### 5.2.5 Focused Gaussian Beam

Since an optically levitated nanoparticle is often trapped using a focused Gaussian laser beam it is practical to consider the shot noise heating due to such an incident wave. The electromagnetic fields of a Gaussian laser beam ((0,0) mode) focused through a lens with numerical aperture  $\text{NA} = \sin \theta_{\max}$  can be expressed in cylindrical coordinates as [66, 97]

$$\vec{E}(\rho, \phi, z) = \frac{ikf}{2} E_0 e^{-ikf} \begin{bmatrix} I_{00} + I_{02} \cos 2\phi \\ I_{02} \sin 2\phi \\ -2iI_{01} \cos \phi \end{bmatrix}, \quad (5.20a)$$

$$\vec{H}(\rho, \phi, z) = \frac{ikf}{2Z_0} E_0 e^{-ikf} \begin{bmatrix} I_{02} \sin 2\phi \\ I_{00} - I_{02} \cos 2\phi \\ -2iI_{01} \sin \phi \end{bmatrix}, \quad (5.20b)$$

where  $Z_0$  is the impedance of free space,  $f$  is the focal length of the lens, and the  $I_{i,j}$  are integrals over the polar angle up to the extent of the lens,  $\theta_{\max}$ . The expressions for the integrals are

$$I_{00} = \int_0^{\theta_{\max}} f_w(\theta) (\cos \theta)^{1/2} \sin \theta (1 + \cos \theta) J_0(k\rho \sin \theta) e^{ikz \cos \theta}, \quad (5.21)$$

$$I_{01} = \int_0^{\theta_{\max}} f_w(\theta) (\cos \theta)^{1/2} \sin^2 \theta J_1(k\rho \sin \theta) e^{ikz \cos \theta}, \quad (5.22)$$

$$I_{02} = \int_0^{\theta_{\max}} f_w(\theta) (\cos \theta)^{1/2} \sin \theta (1 - \cos \theta) J_2(k\rho \sin \theta) e^{ikz \cos \theta}, \quad (5.23)$$

where  $J_n(x)$  is the Bessel function of order  $n$ ,  $f_w(\theta) = \exp(\sin^2 \theta / f_0^2 \sin^2 \theta_{\max})$  is the apodization function with the filling factor  $f_0 = w_0/R_a$  is the ratio of the laser beam waist before the lens and the radius of the aperture. For a detailed discussion of Eqs. (5.20) see Ref. [66].

Since the incident wave is no longer a plane wave, Eqs. (5.8) are not suitable for describing the energy transfer from the laser to the particle. Following a method similar to that of Refs. [98] and [99], the shot noise heating rate for a general particle and incident wave can be written compactly as

$$\dot{E}_{Tx_i} = J_p \epsilon \int d^2 \hat{k}' \left| \frac{\partial f(x_i, \vec{k}, \vec{k}')}{\partial x_i} \right|_{x_i=0}^2, \quad (5.24)$$

where  $x_i = (x, y, z)$  and  $f(x_i, \vec{k}, \vec{k}')$  is the scattering amplitude. For an incident plane wave,  $f(\vec{r}, \vec{k}, \vec{k}') = e^{i\vec{k}\cdot\vec{r}} f(\vec{k}, \vec{k}') e^{-i\vec{k}'\cdot\vec{r}}$ , yielding Rayleigh shot noise, Eqs. (5.19) in Sec. 5.2.3.

To compute the shot noise heating rate using Eq. (5.24) for a sphere of radius  $r$  with incident waves given by Eqs. (5.20) the scattered fields must be obtained. One approach is to combine Mie theory with the highly focused fields which has been undertaken in Ref. [100] to evaluate optical forces. In the present section, the scattered fields are computed numerically by employing the discrete-dipole approximation method (DDA) [101]. In the DDA, the spherical particle is composed of  $N$  discrete spherical dipoles each with polarizability  $\alpha$  and the internal fields of the dielectric are solved for self-consistently to retrieve the scattered fields outside the particle. Once the scattered fields are obtained the scattering amplitude can be determined. In the implementation of the DDA used for this calculation, each dipole that composed the spherical particle had a polarizability  $\alpha = 4\pi\epsilon_0 R^3 \left( \frac{\epsilon - 1}{\epsilon + 2} \right)$ . The shot noise heating rates relative to the Rayleigh expression for various numerical apertures and particle radii are shown in Fig. 5.3. The calculations were performed for a spherical particle composed of silica,  $n = 1.45$ , with its center of mass located at the focus,  $\vec{r}_0 = \langle 0, 0, 0 \rangle$ . The heating rates for each degree of freedom ( $x, y, z$ ) (first, second, and third column) were computed for two different laser wavelengths 1550 nm (top row) and 1064 nm (bottom row). The waist of the Gaussian laser beam just before entering the focusing lens was chosen to be twice the aperture radius of the lens, corresponding to a filling factor  $f_0 = 2$  for all values in the figure.

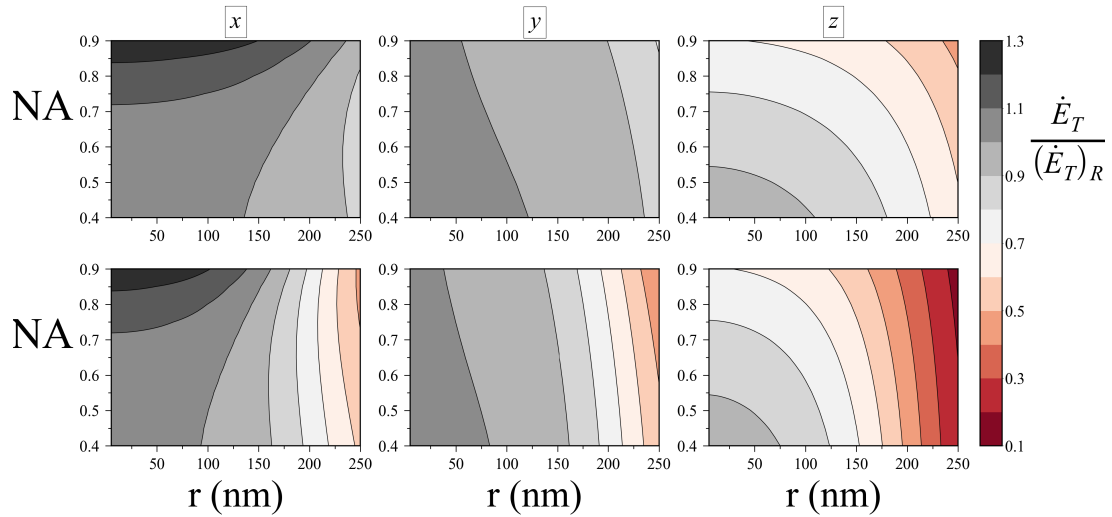


Figure 5.3. Contour surface plots of the shot noise heating rate for each degree of freedom relative to the rate in the Rayleigh limit for silica ( $n = 1.45$ ) at laser wavelengths  $\lambda = 1550$  nm (top row) and  $\lambda = 1064$  nm (bottom row). The heating rates for each degree of freedom ( $x, y, z$ ) are shown in the first, second, and third column respectively. The colorbar on the far right is a scale for the ratio between the numerically calculated shot noise heating, Eq. (5.24), and the Rayleigh expression for that degree of freedom. As expected for small NA and radius the shot noise in each degree of freedom agrees well with the Rayleigh expression.

As the radius of the particle increases, the shot noise heating decreases relative to the Rayleigh expression for all NA. As the radius increases, the intensity per volume decreases. Rayleigh expressions assume uniform incident plane waves while a tweezer has a Gaussian-like spot size.

When the numerical aperture increases, the  $\hat{z}$  component of the beam is more prominent, resulting in a polarization mainly in the  $x - z$  plane (the  $y$  component is negligible). It is plausible that since shot noise heating is smallest in the degree of freedom associated with the polarization direction, the shot noise in the axial degree of freedom decreases while heating increases in the  $x$  degree of freedom.

As the beam becomes more focused, the beam diverges more strongly as it exits the focal region. As opposed to a plane wave, which always propagates in the  $\hat{k}_i = \hat{z}$  direction, the incident wave through the particle due to a focused beam has propagation components in the  $\hat{x}$  and  $\hat{y}$  directions as well, decreasing the shot noise in the  $\hat{z}$  degree of freedom. This comes from the main factor of discussion in Sec. 5.2.2, the  $\hat{k}_{ij}^2$  term in Eq. (5.5) which gave a change in energy of  $1\epsilon$  in the direction of photon propagation for Rayleigh scattering in Eq. (5.12). This influence thus decreases for focused beams. In fact, Ref. [29] introduced a geometric factor  $A \leq 1$  helping to explain this effect. The factor allows for an approximate evaluation of the energy delivered to the particle in the  $z$  degree of freedom

$$\langle \Delta E_z \rangle_R \approx \epsilon \left( A^2 + \frac{2}{5} \right). \quad (5.25)$$

The geometrical factor is a result of a first order expansion of Eqs. (5.20) valid for particles small compared with the wavelength. The expression for  $A$  is a ratio of integrals [29] and approximates to  $A \approx 1 - (kz_R)^{-1}$  for small NA, where  $z_R$  is the Rayleigh range of a paraxial Gaussian beam [76].

Insertion of Eq. (5.25) into Eq. (5.13) for the shot noise in the  $z$  degree of freedom should be accurate for  $\lambda \gg r$ . Using the data obtained in Fig. 5.3 for particles with  $r = 5$  nm, the shot noise agrees with the approximate evaluation using Eq. (5.25) to within 2% for all NA.

The reduction in shot noise energy delivered to the  $z$  degree of freedom does not result in an increase in energy in the other degrees of freedom while the particle is situated at the origin. Since the particle is a sphere and the beam is symmetrical about the origin, the  $\hat{x}$  and  $\hat{y}$  components of the incident wavevectors on the particle in the  $-\hat{z}$  half space are reflections of the  $\hat{x}$  and  $\hat{y}$  outgoing wavevectors in the  $+\hat{z}$  halfspace, canceling the influence of the incident propagation direction on the shot noise in the  $x$  and  $y$  degrees of freedom.

The overall magnitudes for the shot noise in each degree of freedom in Fig. 5.3 are within an order of magnitude of the Rayleigh expression up to a radius of  $r = 250$  nm. Fortunately for experimentalists attempting to reach the motional quantum ground state, the values decrease as the radius increases for all degrees of freedom. This allows the Rayleigh expression for the shot noise heating rate to be used as an upper bound for calculations and a good approximation for all NA.

A natural next question is how the shot noise would be distributed for a particle in a standing Gaussian wave, the situation of consideration for particles trapped in a driven cavity. Differing from tweezer traps, cavity traps typically have very large beam waists  $\sim 40 \mu\text{m}$  [31, 71] and therefore the radial geometry of the beam is well approximated as a symmetric Gaussian. Over the range of a nanoparticle  $r \sim 100$  nm the field is essentially uniform and the beam can be approximated as an incident plane wave. In the axial direction the field dependence is of the form  $\sim \cos kz$ . The particle is placed in two common locations  $z = 0$  for cavity trapping and  $z = \lambda/8$  for maximal cavity coupling. The latter situation can be achieved by using a separate tweezing laser to place the particle at that location [31, 33, 34]. The following discussion is with reference to the shot noise from the cavity photons solely. The shot noise heating rate for a silica Mie particle of varying radius located at  $z = \lambda/8$  has been calculated analytically in Ref. [98] and numerically for a cavity with 1064 nm wavelength and  $26 \mu\text{m}$  waist. Up to  $\approx 250$  nm in radius, Fig. 4 in Ref. [98] shows the shot noise increasing as the particle size increases. Our calculations confirm this result. However,

it should not follow the traditional Rayleigh  $r^3$  dependence exactly. Owing to the large beam waist, the situation is similar to that in Fig. 5.1(e) in this thesis.

Additionally, at  $z = 0$ , the dependence on the initial photon propagation direction  $\hat{k}_{ij}^2$  vanishes giving  $A = 0$  in Eq. (5.25). The amount of shot noise delivered to the axial degree of freedom,  $z$ , is then equal to the amount delivered to the degree of freedom orthogonal to both the polarization and axial directions,  $y$ . However, at  $z = \lambda/8$  the  $\hat{k}_{ij}^2$  contribution returns, giving Eq. (5.12) for Rayleigh particles.

### 5.3 Rotational Rayleigh shot noise

This section examines the shot noise heating in the rotational degrees of freedom for a symmetric-top particle in the Rayleigh regime, such as the nanodumbbell in Ch. 4. The rotational heating rate is calculated in a similar fashion to that in Sec. 5.2.3. Here, the shot noise heating rate due to elliptically polarized light will be presented which can then be generalized for linear, circular, or unpolarized light by taking the respective limits.

The particle has moment of inertia  $I_x$  perpendicular to the symmetry axis,  $I_z$  along the symmetry axis, and  $\alpha_x, \alpha_z$  are the polarizabilities perpendicular and parallel to the symmetry axis, respectively. The particle density operator in the orientational basis is  $\rho(\Omega, \Omega')$  with  $\Omega = (\alpha, \beta, \gamma)$  the Euler angles in the  $z$ - $y'$ - $z''$  convention [76]. Let  $\Omega$  refer to the system before a scattering event and primed coordinates refer to the system following a scattering event. The rotational master equation reads

$$\frac{\partial}{\partial t} \rho(\Omega, \Omega') = -\Lambda(\Omega, \Omega') \rho(\Omega, \Omega'), \quad (5.26)$$

where

$$\Lambda = \frac{J_p}{2} \int d^3 \vec{k} \mu(\vec{k}) \int d^2 \hat{k}' |f_{(\Omega)}(\vec{k}, \vec{k}') - f_{(\Omega')}(\vec{k}, \vec{k}')|^2, \quad (5.27)$$

is the decoherence rate,  $f_{(\Omega)}(\vec{k}, \vec{k}')$  is the scattering amplitude, and  $\mu(\vec{k}) = \delta(\vec{k} - \vec{k}')$  is the distribution of the laser which will again be taken to be a delta function. The shot noise heating rate may be calculated through

$$\dot{E}_R = \frac{d}{dt} \langle \mathbf{H}_R \rangle = \text{tr}(\mathbf{K}_R \frac{\partial}{\partial t} \boldsymbol{\rho}), \quad (5.28)$$

with  $\mathbf{H}_R = \mathbf{K}_R + \mathbf{U}_R$  the rotational Hamiltonian,  $\mathbf{U}_R$  the potential energy which has zero contribution in the above equation, and  $\mathbf{K}_R$  is the rotational kinetic energy. In the  $z$ - $y'$ - $z''$  convention, the rotational kinetic energy is [82]

$$\mathbf{K}_R = -\frac{\hbar^2}{2I_x} \left[ \frac{\partial^2}{\partial \beta^2} + \cot(\beta) \frac{\partial}{\partial \beta} + \frac{1}{\sin^2(\beta)} \frac{\partial^2}{\partial \alpha^2} - \frac{2 \cos(\beta)}{\sin^2(\beta)} \frac{\partial^2}{\partial \alpha \partial \gamma} + \left( \frac{I_x}{I_z} + \cot^2(\beta) \right) \frac{\partial^2}{\partial \gamma^2} \right]. \quad (5.29)$$

To evaluate Eq. (5.26), begin with the far field scattering amplitude for a point dipole

$$f_{(\Omega)}(\vec{k}, \vec{k}') = \left( \frac{k^2}{4\pi\epsilon_0 E_0} \right) \hat{\zeta} \cdot \vec{p}, \quad (5.30)$$

with  $\hat{\zeta}$  the polarization of the scattered light,  $E_0$  the magnitude of the incident electric field, and  $\vec{p} = \overset{\leftrightarrow}{R} \overset{\leftrightarrow}{\alpha}_0 \overset{\leftrightarrow}{R} \vec{E}_{\text{inc}}$  the polarization vector. For incident elliptical light defined by  $\vec{E}_{\text{inc}} = E_0 \langle \cos \psi, i \sin \psi, 0 \rangle \exp(ikz)$ ,

$$\begin{aligned} \vec{p} &= \overset{\leftrightarrow}{R} \overset{\leftrightarrow}{\alpha}_0 \overset{\leftrightarrow}{R} \vec{E}_{\text{inc}} \\ &= E_0 \begin{pmatrix} \cos \psi \left[ \alpha_x + (\alpha_z - \alpha_x) \sin^2 \beta \cos^2 \alpha \right] + i \sin \psi \left[ (\alpha_z - \alpha_x) \sin^2 \beta \cos \alpha \sin \alpha \right] \\ \cos \psi \left[ (\alpha_z - \alpha_x) \sin^2 \beta \cos \alpha \sin \alpha \right] + i \sin \psi \left[ \alpha_x + (\alpha_z - \alpha_x) \sin^2 \beta \sin^2 \alpha \right] \\ \cos \psi \left[ (\alpha_z - \alpha_x) \sin \beta \cos \beta \cos \alpha \right] + i \sin \psi \left[ (\alpha_z - \alpha_x) \sin \beta \cos \beta \sin \alpha \right] \end{pmatrix} \\ &\equiv (\alpha_z - \alpha_x) E_0 \begin{pmatrix} A_x + iB_x \\ A_y + iB_y \\ A_z + iB_z \end{pmatrix} + \alpha_x E_0 \begin{pmatrix} \cos \psi \\ i \sin \psi \\ 0 \end{pmatrix}, \end{aligned} \quad (5.31)$$

where the  $A_j = A_j(\alpha, \beta, \gamma)$  ( $B_j = B_j(\alpha, \beta, \gamma)$ ) are the real (imaginary) parts of the polarization vector component  $j = (x, y, z)$ .

For scattered light in the  $\hat{r} = \langle \sin \theta \cos \phi, \sin \theta \sin \phi, \cos \theta \rangle$  direction in spherical coordinates, the outgoing polarization vector  $\hat{\zeta}$  can take two directions  $\hat{\theta} = \langle \cos \theta \cos \phi,$

$\cos \theta \sin \phi, -\cos \theta\rangle$  or  $\hat{\phi} = \langle -\sin \phi, \cos \phi, 0\rangle$ . As there is no preference for which polarization is chosen, the sum of the scattering amplitudes must be used in Eq. (5.28),

$$|f_{(\Omega)}(\vec{k}, \vec{k}') - f_{(\Omega')}(\vec{k}, \vec{k}')|^2 \rightarrow \left(\frac{k^2}{4\pi\epsilon_0 E_0}\right)^2 \left(|\hat{\theta} \cdot \vec{p} - \hat{\theta} \cdot \vec{p}'|^2 + |\hat{\phi} \cdot \vec{p} - \hat{\phi} \cdot \vec{p}'|^2\right). \quad (5.32)$$

Performing the integrals in Eq. (5.27) gives the decoherence rate as

$$\Lambda = J_p \left(\frac{4\pi}{3}\right) \left(\frac{k^2}{4\pi\epsilon_0}\right)^2 (\alpha_z - \alpha_x)^2 \sum_j [(A_j - A'_j)^2 + (B_j - B'_j)^2], \quad (5.33)$$

with  $A'_j = A_j(\alpha', \beta', \gamma')$  and  $B'_j = B_j(\alpha', \beta', \gamma')$ .

To calculate the shot noise using Eq. (5.28), note that the  $\frac{\partial}{\partial \gamma}$  terms from Eq. (5.29) evaluate to zero as there is no  $\gamma$  dependence in the polarization vector in Eq. (5.31). From here, the orientation of the nanoparticle relative to the incident polarization must be considered. For well librationaly bound nanoparticles under weak elliptical polarization, the particle is undergoing oscillations for which the small angle approximation may be appropriately made,  $\alpha \rightarrow 0 + \xi$ ,  $\beta \rightarrow \frac{\pi}{2} - \eta$ . In this view, Eq. (5.29) may be rewritten

$$\begin{aligned} \mathbf{K}_R &\rightarrow -\frac{\hbar^2}{2I_x} \left[ \frac{\partial^2}{\partial \beta^2} + \cot(\beta) \frac{\partial}{\partial \beta} + \frac{1}{\sin^2 \beta} \frac{\partial^2}{\partial \alpha^2} \right] \\ &\approx -\frac{\hbar^2}{2I_x} \left[ \frac{\partial^2}{\partial \eta^2} + \frac{\partial^2}{\partial \xi^2} \right]. \end{aligned} \quad (5.34)$$

Inserting Eqs. (5.33) and (5.34) into Eq. (5.29) and taking the trace gives the total rotational shot noise for elliptically polarized light to second order

$$\begin{aligned} \dot{E}_{R_e} &= J_p \left(\frac{4\pi}{3}\right) \left(\frac{k^2}{4\pi\epsilon_0}\right)^2 (\alpha_z - \alpha_x)^2 \left(\frac{\hbar^2}{2I_x}\right) [4 \cos^2 \psi + 2 \sin^2 \psi] \\ &= \frac{\dot{E}_{R_{\parallel}}}{4} [4 \cos^2 \psi + 2 \sin^2 \psi], \end{aligned} \quad (5.35)$$

with the energy distributed as

$$\left(\dot{E}_\alpha, \dot{E}_\beta, \dot{E}_\gamma\right) = \frac{\dot{E}_{R_{\parallel}}}{2} (\cos^2 \psi + \sin^2 \psi, \cos^2 \psi, 0). \quad (5.36)$$

For a symmetric-top particle illuminated by a linearly polarized laser with  $\vec{E}_{\text{inc}} = E_0 \exp(ikz)\hat{x}$ , the particle's symmetry axis will tend to align near the polarization axis. Using Eq. (5.35) with  $\psi = 0$ ,

$$\dot{E}_{R_{\parallel}} = J_p \left( \frac{16\pi}{3} \right) \left( \frac{k^2}{4\pi\epsilon_0} \right)^2 (\alpha_z - \alpha_x)^2 \left( \frac{\hbar^2}{2I_x} \right). \quad (5.37)$$

The amount of shot noise delivered to each Euler angle  $\alpha, \beta, \gamma$  in the  $z$ - $y'$ - $z''$  convention [76] is

$$\left( \dot{E}_{\alpha}, \dot{E}_{\beta}, \dot{E}_{\gamma} \right)_{\parallel} = \frac{\dot{E}_{R_{\parallel}}}{2} (1, 1, 0). \quad (5.38)$$

If the particle's symmetry axis is orthogonal to both the laser polarization and laser propagation direction  $\psi = \pi/2$ , the energy is distributed as

$$\left( \dot{E}_{\alpha}, \dot{E}_{\beta}, \dot{E}_{\gamma} \right)_{\perp} = \frac{\dot{E}_{R_{\parallel}}}{2} (1, 0, 0). \quad (5.39)$$

For unpolarized light, it is the average of Eqs. (5.38) and (5.39). As the angle  $\alpha \rightarrow \pi/2$ , the amount of shot noise delivered to the  $\beta$  degree of freedom decreases. This can be understood from a decoherence/measurement perspective. As the nanoparticle's symmetry axis becomes orthogonal to the laser polarization and propagation directions, the laser can no longer provide information about the orientation of  $\beta$ ; while  $\alpha = \pi/2$ , all angles  $0 \leq \beta \leq \pi$  look equivalent with respect to the laser polarization direction. This leaves  $\beta$  to be immeasurable and is therefore immune to decoherence/heating.

## 6. METHODS OF COOLING THE MOTION

As levitated particles follow the equipartition theorem [19,102], removing energy from the motion can be seen as lowering the particle's temperature,  $T = n\hbar\omega/k_B$ . Reducing the temperature of a levitated particle is one of the most useful accomplishments in the field and perfecting a method is one of the most sought after goals. From generating spatial superpositions for testing wavefunction collapse models to detection of gravitational waves, cooling the motion has great promise for the future of fundamental physics and our understanding of the universe [6–12].

Limiting the nanoparticle temperature that can be reached by cooling is inefficient detection of scattered light, laser shot noise, phase noise, among others. These limitations seen in conventional tweezer traps have sparked theorists and experimentalists alike to explore new and hybrid levitated systems that may offer alternative routes to the quantum regime. Passive/sympathetic cooling schemes involving coupling different degrees of freedom or nearby particles has been explored [17, 61, 84, 103–105]. Cavity cooling has had success [32, 33, 71] where strong coupling rates have been achieved through coherent scattering with the addition of a tweezer trap and allowed cooling to the lowest reported occupation number of  $\bar{n} < 1$  [31, 34]. All electrical or electro-optical hybrid systems utilizing electronic circuitry [106–108] even in its beginning stages are able to reach mK temperatures [109, 110] with one particular experiment reaching  $\bar{n} = 4$  through cold damping [28]. The field has also recently seen magnetic particles and traps being investigated [111–114], such as studying the dynamics of a ferromagnetic particle levitated above a superconductor [115–117].

This chapter provides three theoretical works [76, 118, 119] that offer new possibilities for cooling a levitated nanoparticle and an analysis of an experimental work [77] that cooled three translational and two rotational degrees of freedom of a levitated nanodumbbell simultaneously.

## 6.1 Parametric feedback cooling the rotational motion of nanodumbbells

Much progress has been made in cooling the translational degrees of freedom (DOF) [22,23,68–71] with a lowest reported occupation number  $\bar{n} < 1$  [34]. Preventing further reduction in the occupation number is the efficiency with which the position can be detected and collisions with the surrounding gas particles [23,69]. Shot noise on the detector from the trapping laser hinders the efficiency of position detection, and therefore decreases the effectiveness of the feedback cooling mechanism. Increasing the detection efficiency of the scattered light from the nanoparticle would allow more accurate position detection and is necessary to reach deeper into the quantum realm [120–122].

An alternative path to the ground state and a tool for torque sensing [45,123] is accessing control over the rotational DOF [54,56,80,83,84,123,124]. Whereas translational mode frequencies are typically in the kHz range, librational mode frequencies can be in the MHz range, possibly offering a more accessible ground state [39]. Cooling the nanoparticle through coupling of the translational and rotational modes has been explored both theoretically and experimentally [17,61,84]. Cooling of the librational modes directly has also been proposed using active feedback schemes [80]. However, these models often assume libration as the sole rotational motion. Describing the rotational dynamics in terms of libration exclusively is a good approximation for particle shapes such as nanorods because of the small moment of inertia about its symmetry axis, however, as was seen in Chap. 4, this approximation will break down for particles like dumbbells with more nearly equal moments of inertia.

This section investigates the effects of cooling the rotational degrees of freedom of a classical levitated nanodumbbell trapped in a laser field using a method known as parametric feedback cooling, which will be described below, using rigid-body dynamics. The dynamics without feedback cooling are described in Sec. 4.1.

The system under consideration is the same as that in Sec. 4.1. The particle’s center of mass is fixed at the origin so that only rotations are considered. The

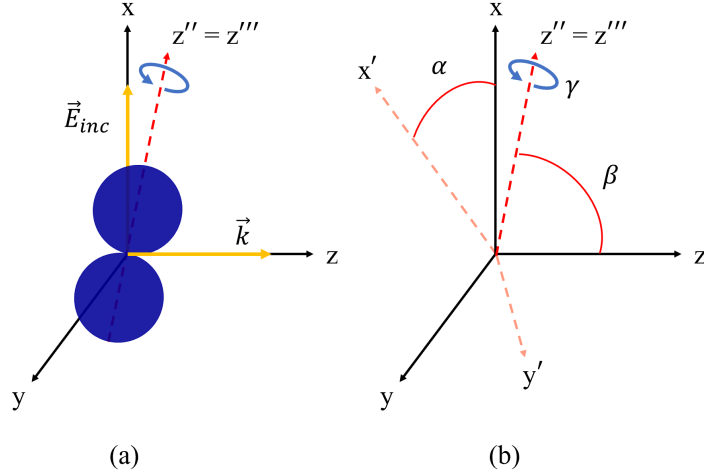


Figure 6.1. (a) A nanodumbbell with center of mass confined to the origin is allowed to rotate. The particle has the lowest energy when its long axis ( $z'''$ -axis) aligns with the laser's electric field polarized in the lab frame  $x$ -direction. (b) The definition of the Euler angles  $\alpha$ ,  $\beta$ ,  $\gamma$  shown in the  $z$ - $y'$ - $z''$  convention. For small angle rotations, the coordinate  $\alpha = 0 + \xi$  describes rotations near the lab frame  $x$ -axis in the  $x$ - $y$  plane and  $\beta = \pi/2 - \eta$  describes rotations near the lab frame  $x$ -axis in the  $x$ - $z$  plane. The coordinate  $\gamma$  describes rotations about the  $z'' = z'''$  axis with  $\gamma(t) \approx \omega_3 t$ . For visual clarity, the  $x'', y'', x''', y'''$  axes have been omitted from the figure.

nanodumbbell is composed of two spheres each with mass  $M_s$  and radius  $R$ . The spheres are aligned along the  $z'''$ -axis and touching at the origin, where the triple prime indicates the particle frame coordinate system (see Fig. 6.1). It is a symmetric top with principal moments of inertia  $I_x = I_y = \frac{14}{5}M_s R^2$  and  $I_z = \frac{4}{5}M_s R^2$ . An amorphous silica nanodumbbell with mass  $2M_s = 1.029 \times 10^{-17}$  kg, radius  $R = 85$  nm,  $I_x = 1.041 \times 10^{-31}$  kg  $\cdot$  m<sup>2</sup>,  $I_z = 2.974 \times 10^{-32}$  kg  $\cdot$  m<sup>2</sup>, index of refraction  $n = 1.458$ , and density  $\rho = 2000$  kg/m<sup>3</sup> [56] is used for the calculations. The laser beam is linearly polarized along the lab frame  $x$ -direction and propagating in the  $z$ -direction with a wavelength  $\lambda = 1550$  nm  $\gg R$ , power 500 mW, and is focused by a NA = 0.45 objective. Because the size of the nanoparticle is much smaller than the

wavelength of light, the nanodumbbell is treated as a point dipole with  $\vec{E}_{\text{inc}} = E_0 \hat{x}$ , the electric field polarizing the dumbbell, having no spatial dependence.

### 6.1.1 Linear polarization

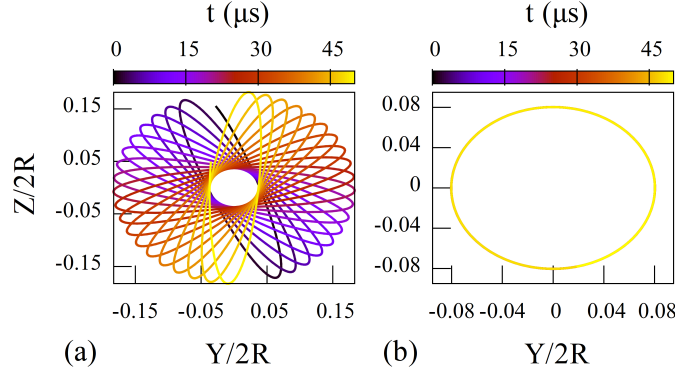


Figure 6.2. Trajectory of the nanoparticle's  $z'''$ -axis, projected on the lab frame  $y$ - $z$  plane found by simulating the full equations of motion and using linear polarization. Here,  $Z/2R = \cos(\beta)$ ,  $Y/2R = \sin(\beta) \sin(\alpha)$  define the location of the  $z'''$ -axis; in the small angle limit  $Z/2R \approx \eta$ ,  $Y/2R \approx \xi$ . (a) The particle's long axis moves in two joint motions, one describing libration and the other describing precession about the polarization axis. (b) Final trajectory of the long axis after parametric feedback cooling. The motion has reduced to pure precession.

Parametric feedback cooling utilizes a laser beam to trap a particle and cool its motion simultaneously through modulation of the laser power at twice the particle's oscillation frequency [23]. To obtain a signal at twice the oscillation frequency, the coordinate to be cooled  $q$  is multiplied by its time derivative  $q\dot{q}$ , for an arbitrary coordinate  $q$ . The idea is that since the particle undergoes harmonic motion,  $q \propto \sin(\omega t)$  and  $\dot{q} \propto \cos(\omega t)$  giving  $q\dot{q} \propto \sin(\omega t) \cos(\omega t) \propto \sin(2\omega t)$  as the source for twice the harmonic frequency. Modulating the potential at twice the frequency cools the motion by tightening the potential when the particle reaches the bottom of the well and loosening it when the particle reaches the classical turning point.

The analyses here assume perfect and instantaneous measurements of  $q\dot{q}$ , which cannot be achieved in practice. Shot noise heating due to photon scattering and the effects of gas collisions are also not included to simplify the analysis. While the heating mechanisms do determine the lowest energy attainable for a fixed cooling power, the dynamical effects of gas collisions do not become important for pressures  $\sim 10^{-3}$  Torr or lower and photon shot noise does not become important until the heating rate is near the cooling rate. See Sec. 6.1.4 for further discussion of these effects and the inclusion of noise. The results that follow thus provide a fundamental limit to cooling, irrespective of the limitations set by quantum mechanics or practical experimental parameters such as orientation detection efficiency.

It is also worth mentioning that since the equations of motion for  $\gamma$  are unaffected by the trapping potential, with the dynamics determined largely by the conserved angular velocity about the particle's symmetry axis,  $\omega_3$ , parametric feedback cooling only directly affects the  $\alpha, \dot{\alpha}$  and  $\beta, \dot{\beta}$  DOF. For this reason, the focus will be on the motions associated with  $\alpha$  and  $\beta$  ( $\xi$  and  $\eta$ ), as it is not possible to cool the nanoparticle's spin about its symmetry axis using parametric feedback cooling.

The equations of motion for the dumbbell in the small angle approximation from Sec. 4.1 Eqs. (4.14) (4.15) under feedback cooling become

$$\ddot{\xi} = -\omega^2(1 + \chi R^2 q\dot{q})\xi - \omega_c \dot{\eta}, \quad (6.1)$$

$$\ddot{\eta} = -\omega^2(1 + \chi R^2 q\dot{q})\eta + \omega_c \dot{\xi}, \quad (6.2)$$

where  $\chi$  is the cooling strength that sets the amplitude of the power modulation. Choosing to measure and feedback  $q\dot{q} = \xi\dot{\xi}$  into Eqs. (6.1) and (6.2), the average cooling power is calculated as

$$\begin{aligned} \langle P \rangle_{\xi\dot{\xi}} &= \left\langle \frac{dE}{dt} \right\rangle \\ &= \left( \frac{I_x}{2} \right) \left\langle \frac{d}{dt} \left[ \dot{\xi}^2 + \dot{\eta}^2 + \omega^2 (\xi^2 + \eta^2) \right] \right\rangle \\ &= -I_x \omega^2 \chi R^2 \left\langle \xi \dot{\xi} (\eta \dot{\eta} + \xi \dot{\xi}) \right\rangle. \end{aligned} \quad (6.3)$$

Inserting the normal mode solutions, Eqs. (4.18) and (4.19), into Eq. (6.3) gives the cooling rate in terms of the normal mode amplitudes  $A_{\pm}$ . Performing the derivatives

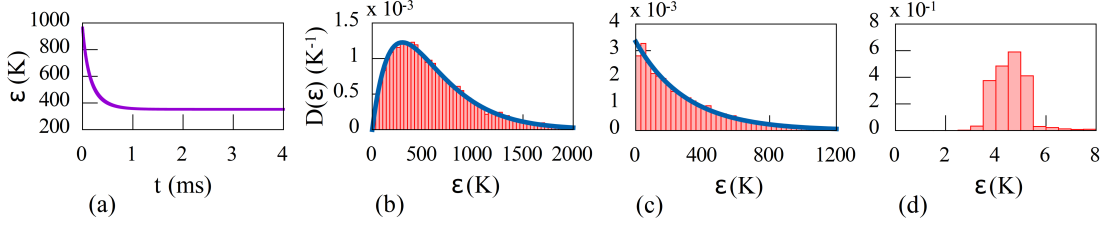


Figure 6.3. (a) Energy of the four quadratic degrees of freedom versus time under parametric feedback cooling during a single trajectory. The energy plateaus to a nonzero value as the nanoparticle circles the polarization axis. (b) Distribution of initial energies used before parametric feedback cooling. The distribution follows the blue line, a Maxwell-Boltzmann distribution with four quadratic degrees of freedom at a temperature of 300 K. (c) Distribution of energies following parametric feedback cooling with linear polarization. The distribution has a mean of 312 K and is similar to the blue line, a Maxwell-Boltzmann distribution with two quadratic degrees of freedom at a temperature of 300 K. The final energies are taken as the last data point in runs similar to that of (a). (d) Final energy distribution of the nanoparticle following feedback cooling with elliptical polarization for  $\theta = \frac{4\pi}{32}$ . Each distribution in this figure is composed of 12,000 runs implemented with a cooling strength  $\chi = 10^7$  s/m<sup>2</sup>.

in Eq. (6.3) with the  $A_{\pm}$  slow compared to  $\omega_{\pm}$  and averaging the sinusoidal factors over one cycle gives

$$\langle P \rangle_{\xi\dot{\xi}} = -\frac{1}{4} I_x \omega^2 \chi R^2 \Omega^2 \left[ A_+(t) A_-(t) \right]^2, \quad (6.4)$$

which implies that cooling is effective until one mode is removed from the motion. As  $t \rightarrow \infty$  the particle will fully precess about the polarization axis with no libration (see Fig. 6.1.1). The result of a single mode remaining is a plateau in the energy over time as shown in Fig. 6.3(a). Choosing to measure and feedback the frequency  $\eta\dot{\eta}$  produces the same result while the addition of the two,  $q\dot{q} = \eta\dot{\eta} + \xi\dot{\xi}$ , delivers the same effect at twice the rate since  $\eta$  and  $\xi$  oscillate at the same frequency.

Using the conserved quantity

$$\frac{d}{dt} \left[ \xi\dot{\eta} - \eta\dot{\xi} - \frac{\omega_c}{2} (\xi^2 + \eta^2) \right] = 0, \quad (6.5)$$

together with the normal mode solutions, Eqs. (4.18) and (4.19), gives the exact expression  $\frac{d}{dt}(A_-^2(t) - A_+^2(t)) = 0$ . This condition shows that as one mode is cooled completely, the second mode ceases to be time dependent, facilitating the notion that there is a limit to how much energy is removed from the motion.

To investigate the extent of possible cooling, a nanodumbbell is initially prepared with a thermal distribution at  $T = 300$  K and several thousand cooling runs are simulated using the full equations of motion. The simulations are run using a fourth order Runge-Kutta adaptive step algorithm [125] with random initial conditions conforming to a Boltzmann distribution. The initial frequencies of rotation are found by

$$\omega_i = \sqrt{\frac{k_B T}{I_j}} dW, \quad (6.6)$$

with  $(i, j) = ((1, x), (2, y), (3, z))$  and  $dW$  a Gaussian random number with zero mean and unit variance. The initial coordinate values  $\alpha, \beta$  are established through rejection sampling of the potential,

$$\mathcal{P}(\alpha, \beta) = e^{-\left(U(\alpha, \beta) - U(0, \frac{\pi}{2})\right)/k_B T}, \quad (6.7)$$

and  $\gamma$  is initialized as a uniformly distributed random number between 0 and  $2\pi$ .

Figure 6.3(b)(c) shows the energy distributions before and after cooling for a cooling strength  $\chi = 10^7$  s/m<sup>2</sup> and feedback frequency  $p_y \dot{p}_y$  (see Eqs. (4.7), (4.48), and (4.49)). In the figure,  $D(\varepsilon)$  is the probability energy density with  $\int_0^\infty D(\varepsilon) d\varepsilon = 1$ . As cooling extracts energy from the  $\alpha, \dot{\alpha}$  and  $\beta, \dot{\beta}$  DOF exclusively, in Fig. 6.3 the shifted energy  $\varepsilon = E - \frac{1}{2} I_z \omega_3^2$  is used where  $E = K + U(\alpha, \beta) - U(0, \pi/2)$  is the total energy adjusted so that 0 K is the minimum energy. The blue lines in Fig. 6.3(b)(c) are plots of the Maxwell-Boltzmann distribution function  $A\varepsilon^n \exp(-\varepsilon/300)$  for four ( $n = 1$ ) and two ( $n = 0$ ) DOF, respectively. As expected, the initial energies follow a Maxwell-Boltzmann distribution with an average energy 602 K  $\sim \frac{4}{2}T$  corresponding to four quadratic DOF. In the final energy distribution, it is seen that effectively two DOF have been removed due to cooling; the final energy distribution has a mean energy of 312 K  $\sim \frac{2}{2}T$ , corresponding to two uncooled quadratic DOF. The two

DOF remaining is consistent with the nanoparticle's long axis circulating around the polarization axis at a fixed non-zero angle, qualitatively seen in both the small angle approximation and the full simulation. The result that parametric feedback cooling is unable to cool the nanoparticle's motion completely even if both coordinate frequencies are known is one of the important results of this section. It is clear that cooling into the quantum regime is not possible utilizing a perfectly linearized beam and standard parametric feedback cooling, even if both angular DOF can be detected.

### 6.1.2 Elliptical polarization

The issue with the previous section's strategy for cooling is the coupling between  $\eta$  and  $\xi$  due to the spin about the symmetry axis and their similar frequencies of rotation about the polarization axis. To cool further requires breaking the symmetry between the two DOF responsible for the precession motion. In this section this symmetry is broken by introducing a potential that produces different librational frequencies for the two coordinates  $\eta$  and  $\xi$ . This can be achieved through elliptical polarization, using two perpendicular laser beams incident on the nanoparticle, or general asymmetries found in a focused laser beam's gradient [66]. Here, elliptical polarization is used with  $\vec{E}_{\text{inc}} = E_0 \langle \cos \theta, i \sin \theta, 0 \rangle$ . The potential energy is given by

$$U = -\frac{E_0^2}{4} \left[ \alpha_x + (\alpha_z - \alpha_x) \sin^2 \beta \right. \\ \left. \times \left( \cos^2 \theta \cos^2 \alpha + \sin^2 \theta \sin^2 \alpha \right) \right]. \quad (6.8)$$

This alters the equations of motion, Eqs. (4.14) (4.15),

$$\ddot{\xi} = -\omega_\xi^2 \xi - \omega_c \dot{\eta} \quad (6.9)$$

$$\ddot{\eta} = -\omega_\eta^2 \eta + \omega_c \dot{\xi} \quad (6.10)$$

where  $\omega_\xi^2 = \omega^2 (\cos^2 \theta - \sin^2 \theta)$ ,  $\omega_\eta^2 = \omega^2 \cos^2 \theta$ .

The normal modes of Eqs. (6.9) and (6.10) are

$$\xi(t) = A_+ \cos(\omega_+ t + \delta_+) + A_- \cos(\omega_- t + \delta_-), \quad (6.11)$$

$$\eta(t) = A_+ \kappa_2 \sin(\omega_+ t + \delta_+) - A_- \kappa_1 \sin(\omega_- t + \delta_-), \quad (6.12)$$

with  $\omega_{\pm} = \frac{1}{\sqrt{2}} \left( \omega_{\xi}^2 + \omega_{\eta}^2 + \omega_c^2 \pm Q \right)^{\frac{1}{2}}$ ,  $Q = \sqrt{4\omega_{\eta}^2 \omega_c^2 + (\omega_c^2 + \omega_{\xi}^2 - \omega_{\eta}^2)^2}$ ,  $\kappa_1 = (2\omega_+ \omega_c) / (Q + \omega_c^2 + \omega_{\xi}^2 - \omega_{\eta}^2)$ ,  $\kappa_2 = (2\omega_- \omega_c) / (Q - \omega_c^2 - \omega_{\xi}^2 + \omega_{\eta}^2)$ . The  $\kappa_i$  ( $i = 1, 2$ ) have the following properties  $\kappa_1^2 \geq 1$ ,  $\kappa_2^2 \leq 1$ ,  $\kappa_i(\theta = 0) = 1$ . The relations are important when considering the cooling rate when feeding back twice of both coordinate's frequencies shown below.

Feedback cooling using either  $q\dot{q} = \xi\dot{\xi}$  or  $q\dot{q} = \eta\dot{\eta}$  gives the following average cooling rates

$$\begin{aligned} \langle P \rangle_{\xi\dot{\xi}} = & \\ & \left[ A_+(t) \right]^4 y_1 - \left[ A_-(t) \right]^4 y_2 - \left[ A_+(t) A_-(t) \right]^2 y_3, \end{aligned} \quad (6.13)$$

$$\begin{aligned} \langle P \rangle_{\eta\dot{\eta}} = & \\ & - \left[ A_+(t) \right]^4 z_1 + \left[ A_-(t) \right]^4 z_2 - \left[ A_+(t) A_-(t) \right]^2 z_3, \end{aligned} \quad (6.14)$$

which reduce to Eq. (6.3) for  $\theta = 0$  and the  $y_i, z_i$  ( $i = 1, 2, 3$ ) are positive and constant for a fixed electric field strength. Equations (6.13) and (6.14) show a combination of heating and cooling with each choice of feedback frequency having preference of cooling a particular mode. In this arrangement one mode is cooled while the other heats, ultimately leading to heating. Simulations of energy versus time while feeding back the frequency  $\eta\dot{\eta}$  or  $\xi\dot{\xi}$  show the energy increasing indefinitely, sometimes following an initial period of cooling depending on the initial conditions.

However, feeding back both coordinate's frequencies in the form  $q\dot{q} = \eta\dot{\eta} + \xi\dot{\xi}$  will lead to cooling of both modes. The small angle approximation equations of motion under cooling become

$$\ddot{\xi} = -\omega_\xi^2 \left(1 + \chi R^2 (\xi\dot{\xi} + \eta\dot{\eta})\right) \xi - \omega_c \dot{\eta}, \quad (6.15)$$

$$\ddot{\eta} = -\omega_\eta^2 \left(1 + \chi R^2 (\xi\dot{\xi} + \eta\dot{\eta})\right) \eta + \omega_c \dot{\xi}. \quad (6.16)$$

The cooling rate is the addition of Eqs. (6.13) and (6.14),

$$\begin{aligned} \langle P \rangle_{\xi\dot{\xi} + \eta\dot{\eta}} &= \langle P \rangle_{\xi\dot{\xi}} + \langle P \rangle_{\eta\dot{\eta}} \\ &= -\left[A_+(t)\right]^4 (z_1 - y_1) - \left[A_-(t)\right]^4 (y_2 - z_2) \\ &\quad - \left[A_+(t)A_-(t)\right]^2 (y_3 + z_3), \end{aligned} \quad (6.17)$$

where

$$(z_1 - y_1) = \left(\frac{I_x \omega_+^2 \chi R^2}{4}\right) (\kappa_1^2 - 1) (\omega_\eta^2 \kappa_1^2 - \omega_\xi^2) \geq 0, \quad (6.18)$$

$$(y_2 - z_2) = \left(\frac{I_x \omega_-^2 \chi R^2}{4}\right) (1 - \kappa_2^2) (\omega_\xi^2 - \omega_\eta^2 \kappa_2^2) \geq 0, \quad (6.19)$$

$$(y_3 + z_3) = \left(\frac{I_x \omega_\xi^2 \chi R^2}{2}\right) (4\omega_\xi^2 + \omega_c^2) > 0, \quad (6.20)$$

which leads to complete cooling for the conditions described here,  $\omega_\eta^2 > \omega_\xi^2 \gg \omega_c^2$ . Only for very large values of  $\omega_c$  ( $\omega_c/\omega \sim 10^5$ ) is  $(y_2 - z_2) < 0$ . Figure 6.3(d) shows the final energy distribution with this choice of feedback for a fixed cooling strength  $\chi = 10^7$  s/m<sup>2</sup> and  $\theta = \frac{4\pi}{32}$ . The particle's accessible DOF have been cooled significantly compared to the case for linear polarization.

Figure 6.3(d) shows the final energies plateauing near 5 K. This is a consequence of the simulation time used of 80 ms and not a limit to further cooling. The limit is set only by the accuracy of the simulations. What delays further energy reduction are the decreasing values of the  $A_\pm(t)$  in the cooling rate  $\langle P \rangle_{\xi\dot{\xi} + \eta\dot{\eta}}$ . To circumvent this delay one may intermittently increase the cooling strength  $\chi$  to achieve more rapid cooling as shown in Fig. 6.4(a). As an example, for the nanoparticle considered here, an occupation number  $n = 1$  corresponds to a temperature on the order of

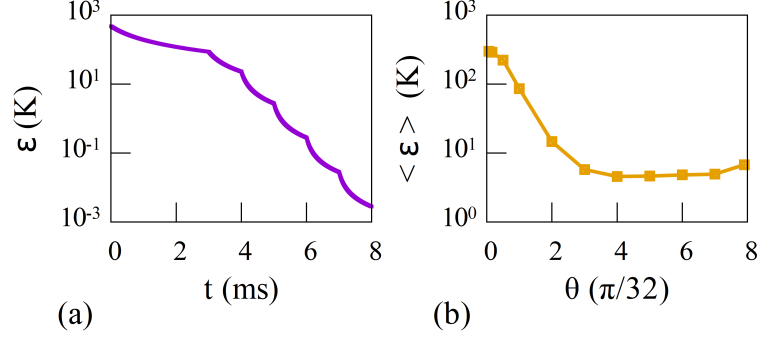


Figure 6.4. Plots showing the dependence of the cooling strength,  $\chi$ , in (a) and the frequency separation of  $\omega_\eta$  and  $\omega_\xi$  in (b) on the cooling rate,  $\langle P \rangle_{\xi\dot{\xi}+\eta\dot{\eta}}$ . (a) Intermittently increasing the cooling strength  $\chi$  during a single cooling process for a fixed electric field strength ( $\theta = \frac{4\pi}{32}$ ). Each dip corresponds to an abrupt increase in the value of  $\chi$ . At  $t = 0$ , the cooling process starts with  $\chi = 10^7$  s/m<sup>2</sup>. Beginning with  $t = 3$  ms,  $\chi$  is increased every 1 ms by a factor of ten, ending with  $10^{12}$  s/m<sup>2</sup>. (b) Average energy after feedback cooling versus  $\theta$  showing the dependence of the frequency separation between  $\omega_\eta$  and  $\omega_\xi$  on the cooling rate  $\langle P \rangle_{\xi\dot{\xi}+\eta\dot{\eta}}$ . The points are averages of 1000 calculated energies following feedback cooling for a fixed simulation time of 80 ms and cooling strength  $\chi = 10^7$  s/m<sup>2</sup>.

$T = \hbar\omega/k_B = 16.7 \mu\text{K}$  for  $\omega/2\pi = 349$  kHz. Setting the simulation accuracy to  $\sim 10^{-10}$  K, the particle is able to reach a temperature of  $\sim 10^{-9}$  K by employing the same method as that in Fig. 6.4(a). These classical calculations thus show that parametric feedback cooling is a suitable method for approaching the quantum regime. The dynamics and fundamental limits at lower temperatures would require a full quantum analysis.

Also affecting the cooling rate is the frequency separation between  $\omega_\xi$  and  $\omega_\eta$ . A slight difference in frequency will allow cooling, but the rate is much larger when the frequency difference is larger. In Fig. 6.4(b) the final average energy of 1000 randomly initialized cooling runs,  $\langle \varepsilon \rangle$ , is plotted versus  $\theta$  with each run having a fixed simulation time of 80 ms. For  $\theta \approx 0$  ( $\omega_\eta \approx \omega_\xi$ ) the average final energy is  $\sim 300$  K, similar to the final temperature when feedback cooling using linear polarization. As  $\theta$  increases ( $\omega_\eta > \omega_\xi$ ), the cooling proceeds more quickly, as evidenced by the

average final energy decreasing. The rate plateaus near  $\theta = \frac{4\pi}{32}$  where the competing heating terms in Eqs. 6.13) and 6.14) become negligible.

### 6.1.3 Experimental signatures

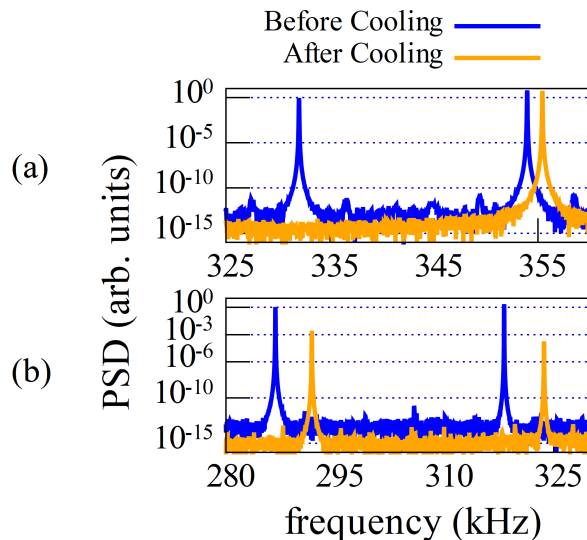


Figure 6.5. Power spectral densities of a  $p_y$  measurement before and after feedback cooling for (a) linear polarization and (b) elliptical polarization. Feedback cooling using linear polarization eliminates one peak, shifting the remaining peak to a normal mode frequency and reducing the motion to pure precession. Feedback cooling under elliptical polarization reduces both peaks in magnitude, and shifts them toward the normal mode frequencies found in the small angle approximation.

What is actually measured in the laboratory is the power spectral density (PSD) of the signal. Figure 6.5(a)(b) shows the PSD of a  $p_y$  measurement before and after cooling the particle using linear and elliptical polarization. Before cooling, two peaks are seen identifying the existence of two rotational motions at different frequencies; the libration and precession motions discussed in Sec. 4.1. As the particle is cooled using linear polarization, both peaks converge to a normal mode frequency  $\omega_{\pm}$  with the larger peak reducing to a non-zero value and the smaller peak decreasing to zero.

Introducing elliptical polarization allows both modes to be cooled fully. In this case, the two initial peaks each converge to a normal mode frequency with the magnitudes of both peaks decreasing to zero.

#### 6.1.4 Discussion of heating and noise

The above analysis has shown that it is theoretically possible to cool the librational motion through parametric feedback cooling within a classical approximation that does not include sources of noise or heating. However, real experiments will encounter unavoidable shot noise, gas collisions, measurement uncertainty, and quantum limits.

The effects of a non-zero measurement uncertainty has been addressed in [80] showing that inefficient feedback sets a lower bound on the occupation number after cooling for a fixed cooling power. This noise source becomes important for a nanoparticle in a low occupation state  $n \sim 50$  ( $T \sim 1$  mK). The spin about the symmetry axis of a nanodumbbell limits the energy of the particle's accessible DOF in the 1-100 K range after parametric feedback cooling with linear polarization (Fig. 6.3(c)), leaving imperfect feedback to be a negligible effect. For elliptical polarization, librational cooling is expected to be affected similarly to that found in [80] with a lower bound on the occupation number.

One may think it possible that gas collisions could induce an asymmetry between the librational coordinates which would allow further cooling. To test this hypothesis the effects of shot noise and gas collisions in our simulations were included for linearly polarized light. Laser shot noise was included using the methods of [80] and Ch. 5. Gas collisions were considered as the Langevin type,  $\dot{\pi}_i = -\Gamma_i \pi_i + \zeta(t)$ , with  $\pi_i = (\dot{\alpha}, \dot{\beta}, \dot{\gamma})$ ,  $\Gamma_i = \tau_i/I_i \Omega_i$  the damping rate ( $\Gamma_\alpha = \Gamma_\beta$ ) [56], and  $\zeta(t)$  stochastic noise. Simulations were performed for three different pressures  $P = 760, 10^{-3},$  and  $10^{-7}$  Torr.

For  $P = 760$  Torr, the nanoparticle is unable to be cooled. The final energies conform to a Maxwell-Boltzmann distribution as it thermalizes with the surrounding

gas at 300 K. Here, increasing the cooling strength  $\chi$ , with hope to overcome energy exchange with the gas, heats the particle as its motion is more Brownian than periodic.

For  $P = 10^{-3}$ , and  $10^{-7}$  Torr, the main results of Secs. 4.1 and 6.1.1 hold, with final energy distributions and PSD's similar to that of Fig. 6.3(c) and Fig. 6.5(a), respectively. The simulations reveal that gas collisions and photon scattering do not change the general conclusions of this section in the classical limit. The effects of laser shot noise and gas collisions while cooling using elliptically polarized light are expected to limit the lowest occupation number attainable for a fixed cooling rate.

### 6.1.5 Conclusion

The effect of parametric feedback cooling using a linearly polarized beam is to remove one of the two modes, resulting in pure precession. In this geometry, it is not possible to extract energy from more than two degrees of freedom and not possible to cool to the quantum regime even when information about both librational modes is available. Evidence of these dynamics may be found in the power spectral density with two peaks converging toward normal mode frequencies during the cooling process, with the smaller of the two peaks' magnitude reducing to zero.

Using a potential energy that sets different frequencies of libration allows cooling to much lower energies when information about both librational modes are available, theoretically approaching the quantum regime in this classical analysis. The setup for cooling may be achieved experimentally by using elliptical polarization or using two perpendicular laser beams incident on the nanoparticle and feeding back both coordinate frequencies. If a single librational coordinate frequency is used in the feedback, the particle will ultimately heat. The rate of cooling is largely determined by the cooling strength and the separation between the two librational frequencies. In this case, the power spectral density will show two peaks converging toward the two normal mode frequencies with both magnitudes decreasing to zero over time.

## 6.2 Experimentally cooling the rotational motion of nanodumbbells

Previous experimental studies have reported cooling of the rotational degrees of freedom of anisotropic particles where the motion is complex and less understood [55, 84, 126]. Following the publication of the work in the previous section, Ref. [76], Ref. [77] reported five dimensional cooling of a levitated nanodumbbell. This work validated the theoretical predictions found in Sec. 4 and much of Sec. 6.1. As noted in Sec. 6.1.3, Fig. 6.5, two main experimental features of levitating nanodumbbells are the observation of two peaks in the power spectral density of the librational coordinates and the frequency difference between them. The two peaks correspond to the two precessional modes  $\omega_{\pm}$ . The frequency separation of the two modes is dependent on the angular frequency about the particle's symmetry axis (the spin),  $\omega_3$ .

In the experiment, each rotational and translational degree of freedom was able to be observed, and five out of six were able to be controlled and actively cooled. Figure 6.6(a) shows the setup for the experiment and Fig. 6.6(b) shows the PSD's obtained from measuring the motion of the  $x, y, z, \alpha, \beta$  degrees of freedom. The translational DOF are observed to have sharp peaks at their harmonic frequencies as is expected from Ch. 3. The  $\alpha, \beta$  degrees of freedom show two broad peaks, centered at  $\omega_{\pm}$ . Two peaks are expected to be observed for the rotational DOF, as explained in Ch. 4 and Sec. 6.1.

In Secs. 6.1.34.3 it was shown not to be possible to directly observe the DOF associated with the spin about a nanodumbbell's symmetry axis,  $\gamma$ , since it is absent from the dipole moment. However, the normal modes of the librational DOF,  $\omega_{\pm}$ , are dependent on the spin  $\omega_3$ . For linear polarization, the frequency separation between the peaks in the power spectral density  $\omega_+ - \omega_- = \omega_c = (I_z/I_x)\omega_3$  is directly proportional to the spin about the symmetry axis. Thus, it is possible to indirectly measure  $\omega_3$  by observing the frequency difference in the normal modes.

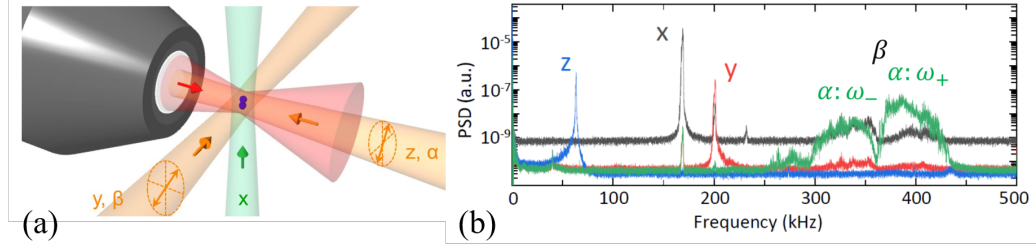


Figure 6.6. Illustration of the experimental setup in Ref. [77] in (a) and the power spectral densities obtained for the  $x, y, z, \alpha, \beta$  degrees of freedom of a dumbbell with radius 85 nm. In the setup, there are a total of 4 lasers. The power with the greatest intensity, the trapping laser (red), is focused by a NA=0.85 objective, traveling in the  $z$  direction and polarized in the  $x$  direction. The remaining 3 lasers are cooling lasers (green and orange). The cooling laser traveling in the  $x$  and polarized in the  $y$  direction provides force feedback on the translational  $x$  degree of freedom. The cooling lasers traveling in the  $y$  and  $-z$  directions are meant to cool the  $y$  and  $z$  degrees of freedom, respectively. The  $y$  and  $z$  cooling lasers simultaneously cool the  $\beta$  and  $\alpha$  degrees of freedom, respectively. This is achieved by tilting the polarizations of each rotational cooling laser roughly 10 degrees with respect to the equilibrium axis of  $\beta$  and  $\alpha$ , the  $x$  axis. The  $y$  and  $z$  cooling lasers power is then modulated at two frequencies, one translational and one rotational. For the power spectral densities in (b), the two normal modes of  $\alpha$  and  $\beta$  can be seen with wide distributions, corresponding to continuously fluctuating  $\omega_3$  due to scattering with the gas molecules.

For symmetric-top particles,  $\omega_3$  is unaffected by the rotational potential energy and is therefore a conserved quantity. However, it is not immune to decoherence from the surrounding air molecules. The dynamics of the spin of the nanodumbbell are then described by Langevin-type, Brownian motion due to collisions with gas air molecules, as described in Sec. 5.1. The fluctuation of  $\omega_3$  causes the frequency separation between the two precessional modes of  $\beta$  and  $\alpha$  to fluctuate. As  $\omega_3$  decreases, the two precessional modes become closer in frequency, whereas when  $\omega_3$  increases the two modes separate further. This would appear as an anti-correlation between the two modes over time. Observation of this effect is seen in Figs. 6.7(a)(b) and 6.8(a)(c).

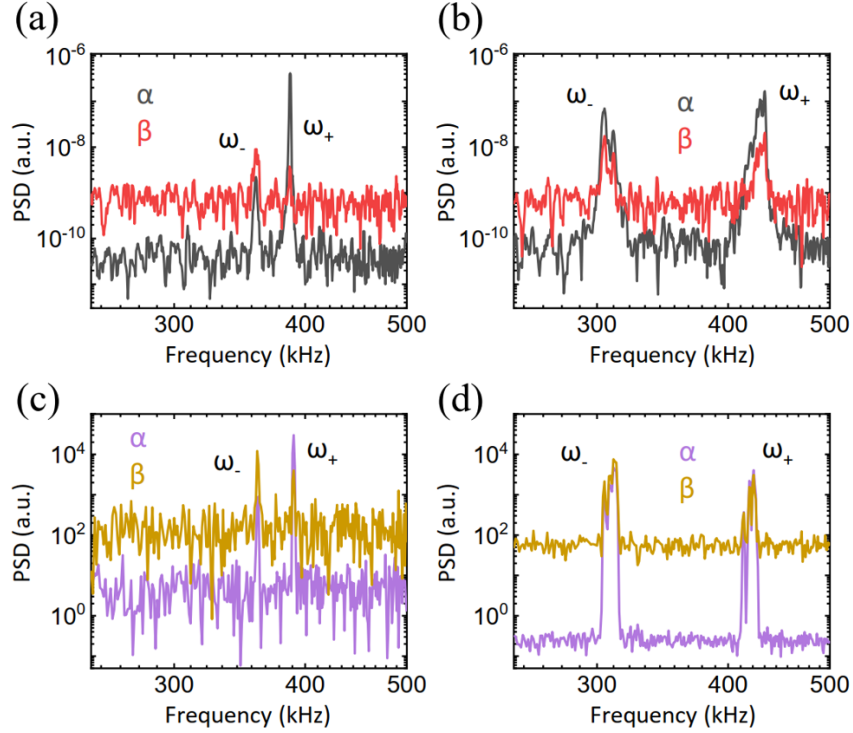


Figure 6.7. (a)(b) Experimental power spectral densities of the  $\alpha$  and  $\beta$  degrees of freedom following the cooling procedure for a  $R = 85$  nm dumbbell. The PSD's are snapshots at two different times, showing how the fluctuation of  $\omega_3$  affects the exact position of the normal modes at any given time. (c)(d) Simulation PSD's using the parameters in the experiment. From (c), the coupling for (a) was found to be  $\omega_c/2\pi = 17$  kHz and from (d), the value of  $\omega_c/2\pi$  is 115 kHz.

Gas collisions also affect the librational degrees of freedom  $\alpha, \beta$  directly. Power spectral densities taken over time scales longer than the damping rate are able to sample a wide range of orientational energies in the non-linear potential. This, in combination with the fluctuating  $\omega_3$ , yield broad peaks for each observable orientational degree of freedom as seen in Figs. 6.6(b) and 6.9. As the pressure lowers, the librational coordinates ( $\alpha, \beta$ ), as well as  $\omega_3$ , become less influenced by gas collisions. The reduction causes the two peaks for ( $\alpha, \beta$ ) to narrow, limited by the more stable, but still fluctuating,  $\omega_3$ . This can be seen in Fig. 6.9.

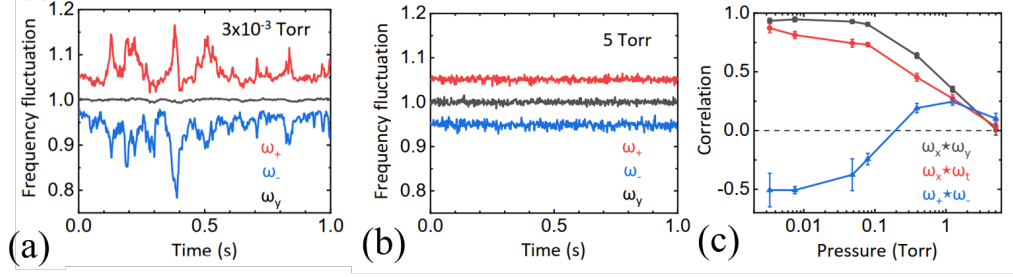


Figure 6.8. (a) Normalized frequency fluctuations  $\omega_y(t)/\langle\omega_y(t)\rangle$ ,  $\omega_+(t)/\langle(\omega_+(t) + \omega_-(t))/2\rangle$ ,  $\omega_-(t)/\langle(\omega_+(t) + \omega_-(t))/2\rangle$  at low pressure  $3 \times 10^{-3}$  Torr showing stable translational motion and large fluctuations for the rotational coordinates. Note the anti-correlation between the  $\omega_{\pm}$  modes. (b) Normalized frequency fluctuations at high pressure, 5 Torr. (c) Correlations between the translational, rotranslational, and rotational DOF. The normal modes of the orientational DOF are anti-correlated due to the coupling with the spin about the nanodumbbell's symmetry axis.

The illustration painted above considered a linearly polarized laser incident on a nanodumbbell. The current experiment utilizes four lasers focused on the nanodumbbell, each with different polarizations. As the rotational potential energy depends on the laser polarization direction, the additional polarization directions introduce further complexity to the rotational dynamics. However, since the power of the three cooling lasers is small relative to the trapping laser, the main features of the rotational motion for linear polarization are retained. Even so, a subtle feature introduced by the perturbation of the cooling lasers is also observed. Specifically, the heights of the two peaks for each librational coordinate are unequal. For a single laser with linear polarization, the heights of the two peaks would be equal for each coordinate  $\alpha, \beta$ . Including a second laser polarized in the  $\hat{z}$  direction shifts the height of the  $\omega_+$  mode to be higher than the  $\omega_-$  mode for the coordinate  $\alpha$ , and vice versa for  $\beta$ . This feature is indeed observed as seen in Figs. 6.6(b) and 6.7(a)(b). If the second laser were polarized in the  $\hat{y}$  direction, it would be expected that the height

of the  $\omega_+$  mode would be reduced compared to the height of the  $\omega_-$  peak for the coordinate  $\alpha$ , and vice versa for  $\beta$ .

Unlike translational motion frequencies, rotational frequencies are dependent on the radius of the particle  $\omega_{\pm} \sim 1/R$ . The two particles studied here,  $R = 60$  nm and  $R = 85$  nm, help show this dependence. From Fig. 6.9 which displays the PSD's before and after cooling a  $R = 60$  nm particle,  $\omega_{\pm 60} \sim (580, 620)$ , whereas  $\omega_{\pm 85} = (340, 400)$  for a 85 nm particle seen in Figs. 6.6(b) and 6.7 before and after cooling, respectively.

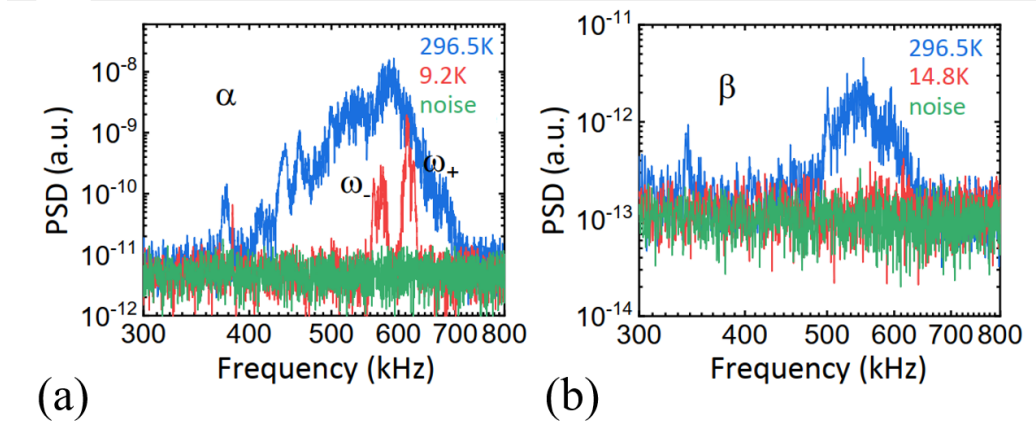


Figure 6.9. Power spectral densities of the orientational degrees of freedom, (a)  $\alpha$  and (b)  $\beta$ . The PSD before cooling is in blue, the PSD after cooling is in red, and the noise floor in green. In (a) the broad peak at 300 K is reduced to the two normal mode peaks with an estimated temperature of 10 K. In (b) the  $\beta$  DOF has been cooled to a point where the signal is below the noise floor.

The method of rotational cooling performed is based on the idea of force feedback cooling (cold damping) traditionally performed on the translational DOF. Here, the two translational cooling lasers traveling in the  $y$  and  $z$  directions, respectively, are simultaneously used for rotational cooling. The two lasers have their polarizations oriented at an angle  $\sim 10$  deg relative to the trapping laser polarization axis, with one cooling laser polarization in the  $x-y$  plane and the other in the  $x-z$  plane, Fig. 6.6(a).

Through modulation of the laser intensities at the two librational angular velocities,  $\dot{\alpha}$ ,  $\dot{\beta}$ , the cooling lasers provide a damping force on the librational coordinates  $\ddot{\alpha} \propto -\Gamma_{\alpha}\dot{\alpha}$ ,  $\ddot{\beta} \propto -\Gamma_{\beta}\dot{\beta}$ . Simulations reveal that this method of cooling has no classical limit of energy reduction. Experimentally, it is estimated that the total rotational energy has been reduced to  $\sim 10$  K, excluding the rotational kinetic energy due to the spin. Limiting further cooling is the constant shifting of the librational peaks due to the spin fluctuations. The continuous shifting of the normal mode peaks inhibits performing an accurate instantaneous time derivative required for the feedback loop.

### 6.3 Sympathetically cooling a magnetic nanoparticle

Another method of cooling a particle is to cool it sympathetically rather than directly. This section explores a possible method of cooling the translational motion of an optically trapped ferromagnetic nanoparticle by coupling to a spin-polarized cold atomic gas. The coupling arises from the magnetic dipole-dipole interaction and allows significant energy exchange between the two systems. While the atom cloud is continuously Doppler cooled, energy is extracted from the nanoparticle through this energy exchange. The coupling of a nanoparticle to an atom cloud has been proposed previously with the coupling mediated by scattered light into a cavity [105]. Sympathetic cooling a particular vibrational mode of a membrane was successfully demonstrated using a similar technique [127–130], but with final temperatures well above the ground state. The scheme proposed here does not require optical cavities and has the potential to cool to the quantum regime.

#### 6.3.1 Toy model

This toy model provides an understanding of the coupling mechanism used for the real proposed system found in Secs. 6.3.2 and 6.3.3. The toy system is comprised of two particles in one dimension with mass  $M_1$  and  $M_2$  individually trapped in their own harmonic traps with frequencies  $\omega_1$  and  $\omega_2$ . The particles are linearly coupled

via the potential energy  $U_{\text{int}} = c\sqrt{M_1 M_2}\omega_1\omega_2 y_1 y_2$  with  $y_i$  the position of particle  $i$  and  $c$  determining the interaction strength. The full potential is

$$U = \frac{1}{2}M_1\omega_1^2 y_1^2 + \frac{1}{2}M_2\omega_2^2 y_2^2 + c\sqrt{M_1 M_2}\omega_1\omega_2 y_1 y_2. \quad (6.21)$$

The equations of motion

$$\ddot{y}_1 = -\omega_1^2 y_1 - c\sqrt{\frac{M_2}{M_1}}\omega_1\omega_2 y_2, \quad (6.22)$$

$$\ddot{y}_2 = -\omega_2^2 y_2 - c\sqrt{\frac{M_1}{M_2}}\omega_1\omega_2 y_1, \quad (6.23)$$

yield four normal mode eigenfrequencies

$$\omega_{\pm}^2 = \frac{1}{2} \left[ (\omega_1^2 + \omega_2^2) \pm \sqrt{(\omega_1^2 - \omega_2^2)^2 + 4\omega_1^2\omega_2^2 c^2} \right], \quad (6.24)$$

which lead to four formal solutions for  $y_1(t)$  and  $y_2(t)$ . On resonance,  $\omega_1 = \omega_2 = \omega$ , Eq. (6.24) simplifies to  $\omega_{\pm} = \pm\omega\sqrt{1 \pm c} \approx \pm\omega(1 \pm c/2)$  in the weak coupling limit  $c \ll 1$ . To garner an idea of the dynamics, presuppose the initial conditions  $y_1(0) = A$ ,  $\dot{y}_1(0) = 0$ ,  $y_2(0) = 0$  and  $\dot{y}_2(0) = 0$  while on resonance in the weak coupling limit. The solutions of Eqs. (6.22) (6.23) can be written as

$$y_1(t) = A \cos(\omega t) \cos\left(\frac{\omega c t}{2}\right), \quad (6.25)$$

$$y_2(t) = -A\sqrt{\frac{M_1}{M_2}} \sin(\omega t) \sin\left(\frac{\omega c t}{2}\right). \quad (6.26)$$

Equations (6.25) and (6.26) show fast oscillations at frequency  $\omega$  enveloped in a slower beat frequency  $\omega c/2$ . The result describes energy exchange between the two oscillators at a rate four times that of the beat frequency  $f_{\text{exch}} = \frac{\omega c}{\pi}$  (see Fig. 6.10). If there is not one, but  $N$  non-interacting particles in the harmonic potential  $\omega_2$ , each interacting with particle 1, the eigenfrequencies and therefore the rate of exchange increases by  $\sqrt{N}$  so that

$$f_{\text{exch}} = \frac{\omega c \sqrt{N}}{\pi}. \quad (6.27)$$

If the particles in trap 2 experience a continual damping force  $F_i = -\alpha v_i$  ( $i \neq 1$ ) energy will be removed from particle 1's motion through the exchange. In the overdamped regime,  $\alpha/M_2 \gg \omega c$ , particle 1's energy decreases according to

$$E_1(t) = E_0 e^{-\gamma t}, \quad (6.28)$$

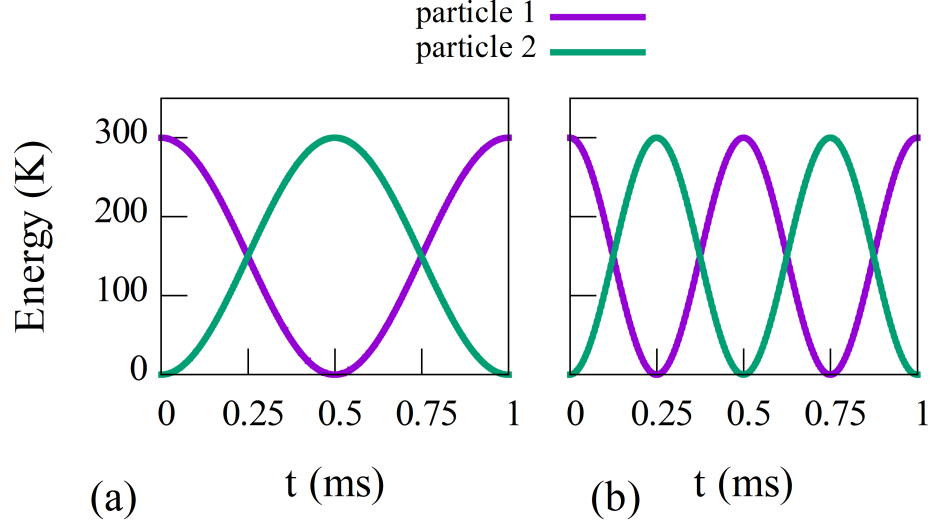


Figure 6.10. (a) Energy versus time of particle 1 and 2 while on resonance. (b) Energy versus time for 1 particle in trap 1 coupled to 4 non-interacting particles in trap 2. As Eq. (6.27) predicts, the exchange frequency increases by  $\sqrt{N} = 2$  compared to (a).

where the cooling rate

$$\gamma \propto \frac{f_{\text{exch}}^2}{\alpha/M_2}, \quad (6.29)$$

determines the temperature reached by particle 1 in time  $t$  in the absence of heating and noise.

### 6.3.2 Model of the system

The proposed physical system includes a ferromagnetic nanosphere of radius  $R$  and mass  $M_p$  harmonically trapped in the focus of a laser beam traveling in the  $\vec{k} = \frac{2\pi}{\lambda} \hat{z}$  direction (see Fig. 6.11). A ferromagnetic sphere with dipole moment  $\vec{m}$  produces a magnetic field [49]

$$\vec{B}_s(r) = \left(\frac{\mu_0}{4\pi}\right) \left[ \frac{3(\vec{m} \cdot \hat{r}) \hat{r}}{r^3} - \frac{\vec{m}}{r^3} \right], \quad (6.30)$$

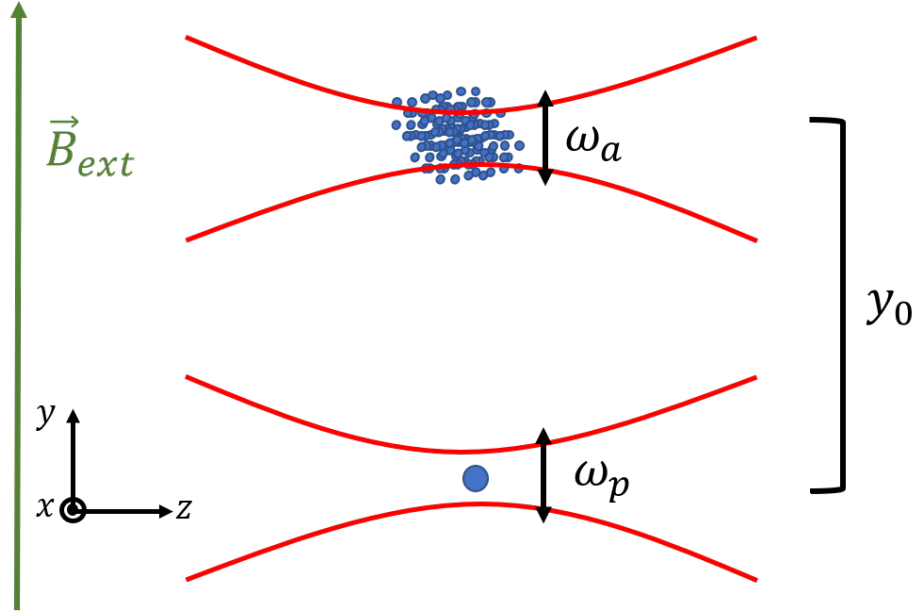


Figure 6.11. Illustration of the proposed model. A ferromagnetic nanoparticle is trapped at the focus of a Gaussian beam. The oscillation frequency for the nanoparticle in the  $y$  direction is  $\omega_p$ . A cloud of  $N$  atoms a distance  $y_0$  away are trapped in a separate, far red-detuned dipole trap oscillating at frequency  $\omega_a$  in the  $y$  direction. An external magnetic field  $\vec{B}_{\text{ext}}$  orients the magnetic moments of the nanoparticle and atoms.

where  $\vec{r}$  is directed outwards from the center of the sphere. The sphere's moment will align along the  $y$ -axis if a constant, uniform magnetic field  $\vec{B}_{\text{ext}} = B_0 \hat{y}$  is present, and a field distribution described by Eq. (6.30) will surround the particle.

A distance  $y_0$  above the focus of the nanoparticle trap, a cloud of  $N$ , non-interacting, spin-polarized atoms each with dipole moment  $\vec{\mu}_a = -\mu_a \hat{y}$  and mass  $M_a$  are trapped in a far red-detuned dipole trap with oscillation frequency  $\omega_a$ . The total particle-atom cloud potential energy including the repulsive interaction  $U_{\text{int},j} = -\vec{\mu}_{a,j} \cdot \vec{B}_s(r_j)$  for each atom  $j$  is

$$U = \frac{1}{2} M_p \omega_p^2 r_p^2 + \sum_{j=1}^N \left( \frac{1}{2} M_a \omega_a^2 r_{a,j}^2 + U_{\text{int},j} \right), \quad (6.31)$$

where  $r_{a,j}$  ( $r_p$ ) is the atom (particle) position. If both the atoms and the nanoparticle undergo small oscillations compared to the distance separating them,  $y_0 \gg (r_p, r_{a,j})$ , the interaction  $U_{\text{int},j}$  is quasi-one-dimensional

$$U_{\text{int},j} \approx g / (y_{a,j} + y_0 - y_p)^3, \quad (6.32)$$

where  $g = 2\mu_a |\vec{m}| \mu_0 / 4\pi$  defines the interaction strength. The  $N + 1$  equations of motion for the  $y$  degrees of freedom are

$$\ddot{y}_p = -\omega_p^2 y_p - \sum_{j=1}^N \frac{3g/M_p}{(y_{a,j} + y_0 - y_p)^4}, \quad (6.33)$$

$$\begin{aligned} \ddot{y}_{a,1} &= -\omega_a^2 y_{a,1} + \frac{3g/M_a}{(y_{a,1} + y_0 - y_p)^4}, \\ &\dots \end{aligned} \quad (6.34)$$

$$\ddot{y}_{a,N} = -\omega_a^2 y_{a,N} + \frac{3g/M_a}{(y_{a,N} + y_0 - y_p)^4}.$$

The focus from here on will be the dynamics associated with the  $y$  degree of freedom. The equations of motion for the  $x$  and  $z$  degrees of freedom have minimal coupling and are therefore largely harmonic oscillators.

In what follows, the aim will be to study the possibility of removing motional energy from the nanoparticle sympathetically by continuously cooling each atom. Doppler cooling was the method of choice for cooling the atoms in this section. Under Doppler cooling each atom experiences a momentum kick  $\hbar k$  in the  $\hat{k}$  direction if a photon is absorbed followed by a kick of the same magnitude in a random direction after spontaneous emission. The probability for absorption in each time interval  $dt \ll 1/\omega_a$  is  $\mathcal{P} = \mathcal{R}dt$  with absorption rate [131]

$$\mathcal{R} = \frac{\Gamma \Omega^2 / 4}{\left(\Delta + \vec{v}_{a,j} \cdot \vec{k}\right)^2 + \Omega^2 / 2 + \Gamma^2 / 4}. \quad (6.35)$$

Here,  $\Omega$  is the Rabi frequency,  $\Gamma$  the decay rate,  $r = I/I_{sat}$  the saturation intensity ratio, and  $\Delta$  the laser detuning. The resulting atom velocity after this time interval can be written as

$$\dot{y}_{a,j}(t + dt) = \dot{y}_{a,j}(t) + \frac{\hbar k}{M_a} \begin{cases} \text{sgn}(\hat{k}) \pm 1, & \text{absorbed} \\ 0, & \text{otherwise} \end{cases}. \quad (6.36)$$

Other factors contributing to the dynamics of the trapped nanoparticle are collisions with the surrounding gas molecules and laser shot noise heating. For the vacuum chamber pressures used in atom trapping,  $\sim 10^{-8} - 10^{-9}$  Torr, the effects due to laser shot noise dominate that of the surrounding gas. After a time interval  $dt$  the nanoparticle velocity becomes

$$\dot{y}_p(t + dt) = \dot{y}_p(t) + \sqrt{2\dot{E}_T dt / M_p} \mathcal{W}(0, 1), \quad (6.37)$$

where  $\dot{E}_T$  is the translational shot noise heating rate [92] and  $\mathcal{W}(0, 1)$  is a random Gaussian number with zero mean and unit variance.

Section 6.3.3 presents the results of simulating Eqs. (6.33) to (6.37) with Eqs. (6.35) and (6.36) modeled using a Monte Carlo method. Subsections 6.3.2 and 6.3.2 explore the dynamics of Eqs. (6.33) and (6.34) analytically under a linear coupling approximation both with and without atom damping.

### Dynamics under an approximate linear coupling

In the regime  $y_0 \gg (y_p, y_{a,j})$ , Eq. (6.32) may be expanded

$$U_{\text{int},j} \approx \frac{g}{y_0^3} \left[ 1 + \frac{3}{y_0} (y_p - y_{a,j}) + \frac{6}{y_0^2} (y_p - y_{a,j})^2 + \dots \right]. \quad (6.38)$$

Keeping only terms to second order in Eq. (6.38) and defining the center of mass of the atom cloud as  $Y_a \equiv \frac{1}{N} \sum_{j=1}^N y_{a,j}$ , the equations of motion may be written as

$$\ddot{y}_p = -N a_p - (\omega_p^2 + N\Omega_p^2) y_p + N\Omega_p^2 Y_a, \quad (6.39)$$

$$\ddot{Y}_a = a_a - (\omega_a^2 + \Omega_a^2) Y_a + \Omega_a^2 y_p, \quad (6.40)$$

where  $a_i = (3g/M_i y_0^4)$ ,  $i = (p, a)$ , is a constant acceleration that shifts the equilibrium position of the oscillator and  $\Omega_i^2 = (12g/M_i y_0^5)$  is a coupling constant as well as a frequency shift in the harmonic potential.

Provided the condition  $y_0 \gg (y_p, y_a)$  is maintained so that higher order terms in Eq. (6.38) do not contribute, the nanoparticle will exchange energy with the atom cloud due to the linear coupling in Eqs. (6.39) and (6.40). Retaining predominantly the lower order terms is only possible for nanoparticle temperatures much smaller than room temperature as the atoms' positions will increase drastically as they exchange energy with the particle. The condition may also be satisfied if the motion of the atoms is continuously cooled via a cooling mechanism such as Doppler cooling, which will be discussed in the next subsection.

Due to the frequency shifts,  $\Omega_i^2$ , the nanoparticle and/or atom cloud trap frequencies need to be tuned to resonance for coherent energy exchange  $\omega_a^2 + \Omega_a^2 = \omega_p^2 + N\Omega_p^2 = \omega_0^2$ . While on resonance, the rate at which energy is exchanged from the particle to the atoms is solved for by finding the normal mode frequencies of Eqs. (6.39) and (6.40) and identifying the beat frequency. This "exchange frequency" is

$$\begin{aligned} f_{\text{exch}} &= \frac{12g\sqrt{N}}{\pi\omega_0 y_0^5 \sqrt{M_p M_a}} \\ &= \frac{\Omega_p \Omega_a \sqrt{N}}{\pi\omega_0}. \end{aligned} \tag{6.41}$$

Note that while the overall force due to the magnetic dipole-dipole interaction was chosen to be repulsive, the dynamics are similar for an attractive interaction since the energy exchange effect is independent of the sign of the linear coupling term. Thus, although the atom cloud may be uniformly spin-polarized through the external magnetic field and optical pumping [132–134], there is no loss of coupling if atoms undergo spin flips on time scales greater than the oscillation period.

## Sympathetic cooling with linear coupling

If each atom in the cloud is continuously Doppler cooled, motional energy can be removed from the nanoparticle. For the calculations in this section, Doppler cooling is modeled using Langevin dynamics and is valid for the time scales of consideration here,  $\Gamma \gg \omega_0$ .

Doppler cooled atoms experience an effective damping force  $F_{D,j} = -\alpha \dot{y}_{a,j}$  with damping rate  $\Gamma_a = \alpha/M_a = \hbar k^2 I / (I_0 M_a)$  when tuned to reach the Doppler temperature  $T_{\min} = \hbar \Gamma / 2k_B$  [131, 134, 135]. Excluding the constant accelerations in Eqs. (6.39) and (6.40), the equations of motion with Doppler cooling on the atoms as well as laser shot noise on the nanoparticle become

$$\ddot{y}_p = -\omega_0^2 y_p + N \Omega_p^2 Y_a + \xi_{\text{SN}}(t), \quad (6.42)$$

$$\ddot{Y}_a = -\omega_0^2 Y_a + \Omega_a^2 y_p - \Gamma_a \dot{Y}_a + \xi_{\text{DC}}(t)/\sqrt{N}, \quad (6.43)$$

where  $\xi_{\text{SN}}(t)$  accounts for fluctuations due to laser shot noise and  $\frac{1}{N} \sum_{j=1}^N F_{a,j}(t)/M_a \rightarrow \xi_{\text{DC}}(t)/\sqrt{N}$  are fluctuations due to spontaneous emission during Doppler cooling.

With the atoms continuously Doppler cooled, the final temperature of the nanoparticle,  $T_p$ , under sympathetic cooling can be estimated. One method is through integration of the power spectral density (PSD) since  $T_p \propto \int S_{yy}(\omega) d\omega = \langle y_p^2 \rangle$ . Fourier transforming Eqs. (6.42) and (6.43) and solving for the nanoparticle's displacement in the frequency domain,  $\tilde{y}_p = \mathcal{F}\{y_p\}$ , gives

$$\tilde{y}_p = \left[ \frac{\sqrt{N} \Omega_p^2 \tilde{\xi}_{\text{DC}}(\omega)}{\Delta} + \tilde{\xi}_{\text{SN}}(\omega) \right] \left[ \frac{1}{\delta^2(\omega) - N \Omega_p^2 \Omega_a^2 / \Delta} \right], \quad (6.44)$$

where  $\Delta = \delta^2(\omega) + i\Gamma_a \omega$  and  $\delta^2(\omega) = \omega_0^2 - \omega^2$ . Shot noise adds an overall constant to the noise floor of the spectrum and near  $\omega \sim \omega_0$  the affects are negligible,  $\tilde{\xi}_{\text{SN}}(\omega) \ll N \Omega_p^2 \tilde{\xi}_{\text{DC}}(\omega) / \Delta$ , and may therefore be omitted. Using the single sided noise spectrum  $|\tilde{\xi}_{\text{DC}}(\omega)|^2 \rightarrow 4\Gamma_a k_B T_{\min} / M_a$ , the PSD of the nanoparticle's displacement is

$$S_{yy}(\omega) = \frac{N \Omega_p^4 (4\Gamma_a k_B T_{\min} / M_a)}{\delta^4(\omega) \left[ (\delta^2(\omega) - N \Omega_p^2 \Omega_a^2 / \delta^2(\omega))^2 + (\Gamma_a \omega)^2 \right]}. \quad (6.45)$$

Equation (6.45) is exact in the absence of laser shot noise on the nanoparticle and has been confirmed through simulation of Eqs. (6.42) and (6.43) with and without  $\xi_{\text{SN}}(t)$ . The PSD is well described by two peaks located at  $\omega_{\pm}^2 = \omega_0^2 \pm \sqrt{N}\Omega_p\Omega_a$  in the weak coupling regime  $\omega_0^2 > \sqrt{N}\Omega_p\Omega_a$ . In the strong coupling regime,  $\omega_0^2 < \sqrt{N}\Omega_p\Omega_a$ , the  $\omega_-$  mode becomes unstable and the particle heats exponentially. Estimates of the final temperature of the nanoparticle through numerical integration of Eq. (6.45) are given in Sec. 6.3.3.

A second measure of the nanoparticle's approximate final temperature can be found by comparing the relative heating and cooling rates. In the weak coupling  $\Gamma_a \gg \Omega_p\Omega_a/\omega_0$  and underdamped regimes  $\omega_0^2 \gg \Gamma_a^2$ , the average cooling power is

$$\begin{aligned} \langle P \rangle &= -NM_p\Omega_p^2 \langle Y_a \dot{y}_p \rangle \\ &\approx Nk_B T_a \frac{(\pi f_{\text{exch}})^2}{\Gamma_a}, \end{aligned} \quad (6.46)$$

where  $T_a = T_{\text{min}}$  is the average temperature of an atom. From Eq. (6.46) the cooling rate is identified as

$$\begin{aligned} \gamma_{\text{cool}} &= \frac{(\pi f_{\text{exch}})^2}{\Gamma_a} \\ &= \frac{144g^2 N}{\omega_0^2 M_p \alpha y_0^{10}}. \end{aligned} \quad (6.47)$$

Note that the particle cooling rate in Eq. (6.47) depends on the number of atoms  $N$ , the atom cooling rate  $\alpha$ , as well as the magnetic interaction strength  $g = (2\mu_a |\vec{m}| \mu_0 / 4\pi) \propto M_p$ . Equation (6.47) shows that slower atom cooling is beneficial for faster cooling of the nanoparticle. However, it is important that  $\alpha$  remain large enough so that the atoms remain in the regime  $y_0 \gg y_{a,j}$  and do not escape the trap as a result of heating.

Since the final temperature of the nanoparticle will be limited by the atoms' Doppler Temperature,  $T_{\text{min}}$ , we may infer a rate equation of the form

$$\dot{T}_p \approx -\gamma_{\text{cool}} (T_p - T_{\text{min}}) + \dot{T}_{\text{SN}}, \quad (6.48)$$

Table 6.1.

Relevant properties of the three species of atoms and their Doppler parameters. From left to right: the atom mass, magnetic moment, decay rate, Doppler line, and Doppler temperature.

Element	$M_a$ (a.u.)	$\mu_a/\mu_B$	$\Gamma/2\pi$ (MHz)	$\lambda_{\text{line}}$ (nm)	$T_{\text{min}}$ ( $\mu\text{K}$ )
Dy	162.5	10	32.2	421	760
Cr	52	6	5.02	425	124
Rb	86.9	1	6.06	780	146

where  $\dot{T}_{\text{SN}}$  is the heating rate due to laser shot noise. Equation (6.48) yields an equilibrium temperature of  $T_p = T_{\text{min}} + \dot{T}_{\text{SN}}/\gamma_{\text{cool}}$ , numerical values of which are calculated in Sec. 6.3.3.

### 6.3.3 Simulations of the full system

#### System description

To determine the extent to which energy can be extracted from a nanoparticle through the scheme outlined in the previous section, several thousand simulations of the  $N + 1$  equations of motion were performed using the full, non-linear, one dimensional  $1/y^3$  potential in Eq. (6.32) while continuously Doppler cooling each atom. Equations (6.33) and (6.34) were numerically solved using a fourth order Runge-Kutta algorithm. Laser shot noise kicks on the particle were implemented using Eq. (6.37) and Doppler cooling was modeled with a Monte Carlo method using Eqs. (6.35) and (6.36).

The nanosphere used for the simulations was composed of YIG with a radius  $R = 50$  nm, density  $\rho = 5110$  kg/m<sup>3</sup>, index of refraction  $n = 2.21$  [136], and magnetic dipole moment  $|\vec{m}| = \frac{1}{5}N_p\mu_B = 4.05 \times 10^{-18}$  JT<sup>-1</sup> where  $\mu_B$  is the Bohr magneton and  $N_p$  is the number of atoms that make up the entire YIG nanoparticle. This

expression for the magnetic moment is approximate, but is conservative compared to what is achievable experimentally [137, 138].

The simulated nanoparticle was trapped in a  $\omega_p/2\pi = 100$  kHz optical trap at the focus of a laser beam linearly polarized along the lab frame  $x$ -direction and propagating in the  $z$ -direction with a wavelength  $\lambda = 1550$  nm  $\gg R$ , power 150 mW, and focused by a NA = 0.6 objective. The nanosphere was set with initial positions and velocities conforming to a Maxwell-Boltzmann distribution at a temperature of  $T = 1$  K. This temperature can be reached experimentally by first using parametric feedback cooling or cold damping before implementing sympathetic cooling [22, 23]. The translational shot noise heating rate  $\dot{T}_{\text{SN}} = 2\dot{E}_T/k_B = 72.4$  mK/s was computed using the Rayleigh expression [92]. Due to the frequency shifts  $\Omega_i^2$  in Eqs. (6.39) and (6.40), the nanoparticle's frequency was shifted to match the frequency of the atoms while at the atom Doppler temperature.

Three species of atoms, dysprosium, chromium, and rubidium, were used for separate simulations. Relevant properties for these atoms are listed in Table 6.1. The atom cloud trap center was placed  $y_0 = \lambda/3 = 516$  nm away from the nanoparticle trap's center. The atom dipole trap frequency  $\omega_a/2\pi = 100$  kHz remained unshifted. The atoms were initially set with velocities at their Doppler temperature and were continuously Doppler cooled. Doppler cooling parameters were set such that the atoms would reach their Doppler temperature  $\Omega = \Gamma\sqrt{r/2}$ ,  $r = I/I_{\text{sat}} = 0.1$ , and  $\Delta = -\Gamma/2$  (see Sec. 6.3.2). Interactions between the atoms and atom loss from the trap were not included in the simulation. For the parameters used in the calculations, the atoms (Dy, Cr, Rb) and particle are sufficiently in the weak coupling regime (see Eq. (6.45))  $\sqrt{N}\Omega_p\Omega_a/\omega_0^2 = (8.23, 6.07, 1.19) \times 10^{-3}$  for  $N = 10^4$ , respectively.

From the parameters above, the beam waist of the particle trap is  $\sim 800$  nm while the atom-particle separation distance is set at 516 nm. While this distance is flexible, we envision the atom trap to be more tightly focused with a wavelength smaller than that of the nanoparticle's. Further, the particle oscillation amplitude is  $\sim 10$  nm at  $T = 1$  K, an order of magnitude smaller than the separation distance. The

separation distance is foreseen to be the main experimental challenge as an increase in the separation by a factor of two decreases the nanoparticle damping rate by a factor of  $2^{10} = 1024$ . One could imagine a thin dielectric barrier placed between the particle and atoms if atom collisions with the nanoparticle would be of concern.

### Simulation Results

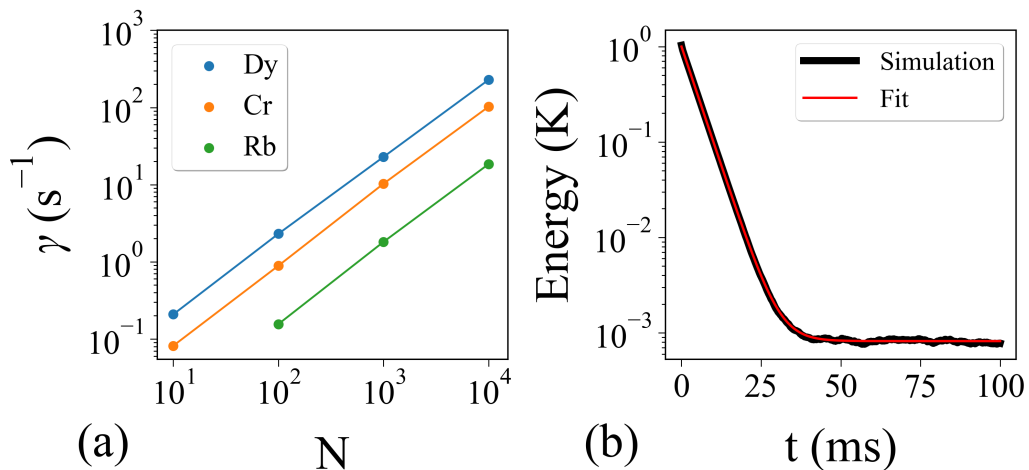


Figure 6.12. (a) Nanoparticle cooling rate versus the number of atoms in the atom cloud. The rate is linearly proportional to the number of atoms and increases for species with larger magnetic moment  $\mu_a$  as predicted by Eq. (3.11). Only atom numbers that produced a statistically significant cooling rate were plotted. (b) Kinetic energy of the nanoparticle versus time for  $N = 10^4$  dysprosium atoms and fit to a decaying exponential. From the fit,  $\gamma$  was extracted and used to plot (a).

For each atom species, the energy removal rate of the nanoparticle,  $\gamma$ , was extracted for varying numbers of atoms in the trap,  $N$ , as seen in Fig. 6.12. From several thousand averages,  $\gamma$  was obtained by fitting energy versus time plots to a decaying exponential,  $E(t) = A \exp(-\gamma t) + C$ , for a given  $N$  (see Fig. 6.12(b)). It is to be noted that due to the long simulation times, most energy versus time plots did not allow for observation of the equilibrium temperature of the nanoparticle and

were solely used for extracting  $\gamma$ . The final temperature of the nanoparticle can be greater than the atom Doppler Temperature as is the case in Fig. 6.12(b) where the final average temperature is  $794 \mu\text{K}$ . This is attributed to shot noise heating as well as non-linear effects that contribute slight frequency mismatching between each atom and the nanoparticle. While the particle is resonant on the average,  $\Omega_{a,j}$  for each atom  $j$  depends on each atom's displacement amplitude and therefore changes slightly with time. The fact that the majority of atoms are out of phase with each other and the nanoparticle does not affect the results.

From Fig. 6.12(a), the cooling rate depends linearly on the number of atoms in the trap as Eq. (3.11) predicts. As the particle exchanges energy with the atoms, each atom acquires a portion of the nanoparticle's energy. When  $n$  more atoms are added to the trap, there are  $n$  more chances for removing that energy through Doppler cooling. As Fig. 6.12(a) shows no deviation from a linear dependence for larger  $N$ , the cooling rate may be extrapolated for larger  $N$  values so long as  $\omega_0^2 > \sqrt{N}\Omega_p\Omega_a$ . As the calculations were performed using the full  $N + 1$  equations of motion, simulation time was the only constraint from observing the effects for larger atom numbers,  $N > 10^4$ .

The average final temperatures reached for each atom species (Dy,Cr,Rb) was  $794 \mu\text{K}$ ,  $406 \mu\text{K}$ , and  $158 \text{ mK}$ , respectively, for a simulation time of  $t = 100 \text{ ms}$  at  $N = 10^4$ . Numerical integration of Eq. (6.45) for the three atom species (Dy, Cr, Rb) at  $N = 10^4$  gives an approximated equilibrium temperature of  $T_p \approx M_p\omega_0^2\langle y_p^2 \rangle/k_B = (2.002, 0.584, 0.572) \text{ mK}$ , respectively. Since the particle is not a simple harmonic oscillator the values are approximate, but may serve as an upper bound for the particle temperature in experiments. The final temperature may additionally be estimated using the rate equation Eq. (6.48),  $T_p = (784, 256, 756) \mu\text{K}$  at  $N = 10^4$  for (Dy, Cr, Rb), respectively, which shows better agreement with the simulation results for Dy and Cr. A simulation time of  $100 \text{ ms}$  was not long enough to observe the equilibrium temperature of the particle using Rb atoms. The expressions used

to estimate the final temperature assume equilibrium has been reached, hence the discrepancy between the simulation temperature and the estimates.

Besides the number of atoms in the trap, Eq. (6.47) predicts that the cooling rate  $\gamma_{\text{cool}} \propto g^2$  depends on the square of the magnetic coupling strength  $g = 2\mu_a|\vec{m}|\mu_0/4\pi$ . Using the data in Fig. 6.12(a) and the values for  $\mu_a$  in Table 6.1,  $\gamma \propto \mu_a^2$  is confirmed with a coefficient of determination  $r^2 = 0.997$ . Together with the linear dependence of  $\gamma$  on  $N$ , this confirms the ability to describe this non-linear system in an approximated linear coupling regime as was done in Sec. 6.3.2.

Note that  $\gamma$  in Fig. 6.12 includes the cooling rate  $\gamma_{\text{cool}}$  as well as the competing shot noise heating rate  $\dot{E}_T$ . The two parameters that these two quantities share are the density, which is predominantly fixed, and the size (radius  $R$ ) of the nanoparticle. Approximating  $|\vec{m}| \propto R^3$  we find  $\gamma_{\text{cool}} \propto R^3$  while  $\dot{E}_T \propto R^3$  shares the same  $R$  dependence [92]. However, shot noise heating is linear in time while the cooling is exponential, indicating that larger particles may provide faster cooling, but will not influence the final temperature of the nanoparticle. The influence of shot noise heating may be further reduced by cooling the degree of freedom in the laser polarization direction,  $\hat{x}$ , since the least amount of shot noise is delivered to that degree of freedom for a particle in the Rayleigh limit [92]. The major source of heating in conventional levitated systems are collisions with the surrounding gas for pressures above  $10^{-6}$  Torr with  $\Gamma_{\text{gas}}/2\pi \sim 10$  kHz. Cold atom experiments typically operate with  $10^{-8} - 10^{-9}$  Torr chamber pressures, making laser shot noise  $\dot{E}_T/\hbar\omega_0 = 7.5$  kHz the dominant source of heating for the YIG particle in this proposal.

## Discussion

To date, cold damping and cavity cooling by coherent scattering have proven to be the most effective methods of cooling a levitated nanoparticle with reported occupation numbers of  $\bar{n} = 4$  and  $\bar{n} < 1$ , respectively [28, 34]. Similar to parametric feedback cooling, cold damping provides damping rates in the  $\sim 1$  kHz range while

coherent scattering has yielded rates in the 10 kHz range [27, 28, 31, 34]. The results above indicate that atom numbers of the order  $N \sim 10^6$ , which corresponds to  $\gamma > 1$  kHz, would be sufficient for the nanoparticle to reach the atom's Doppler temperature even for atom species with unit magnetic moment  $\mu_a/\mu_B = 1$ . The number of atoms that have been trapped experimentally is in the range  $\sim 10^6 - 10^8$  for chromium, rubidium, and others [105, 134, 139]. The ground state energy of the nanoparticle is  $T = \hbar\omega_0/k_B = 5 \mu\text{K}$ . Many of the commonly trapped atom species have unit magnetic moment, large  $N$ , and are able to reach the  $\sim 1 - 10 \mu\text{K}$  regime [140, 141]. Comparing with the energy removal rate found for Rb in Fig. 6.12(a), these parameters are sufficient for motional ground state cooling of the nanoparticle.

The general idea of the proposed scheme is to sympathetically cool a nanoparticle utilizing the linear coupling found in the dipole-dipole interaction, but is not limited to the methods chosen here and allows for adaptability. For example, Doppler cooling as the atom cooling method was chosen for simulation simplicity while retaining physicality. Other atom cooling methods offer lower temperatures such as sideband cooling, Sisyphus cooling, or using a spin-polarized Bose-Einstein condensate, which are able to reach nK temperatures [142]. A charged YIG particle could also be trapped in an ion trap instead of an optical trap.

#### 6.3.4 Conclusion

A theoretical proposal to sympathetically cool a levitated ferromagnetic nanoparticle via coupling to a spin-polarized atomic gas was studied. While oscillating in their respective traps, the particle and atom cloud systems would be coupled through the non-linear magnetic dipole-dipole interaction. For sufficiently large separation between the particle and the atom cloud relative to their displacements, the nanoparticle and atom cloud would exchange energy with one another via the linear coupling term that is dominant in the magnetic force expansion. If the atoms are continuously Doppler cooled, energy would be able to be removed from the particle's motion.

Simulations of the particle-atom cloud system were performed using the full, non-linear, magnetic dipole-dipole interaction for three species of atoms and varying numbers of atoms in the trap. The nanoparticle cooling rate was shown to be proportional to the number of atoms in the trap as well as the square of the magnetic moment of the atom, validating that it is possible to describe the dynamics using a linear approximation to the magnetic force. The rate at which energy is removed from the particle motion is significant for  $10^4$  atoms in the trap when the atoms are continuously Doppler cooled. It is expected that the particle would reach the atom Doppler temperature as the number of atoms increases. This method of sympathetic cooling has potential to cool the nanoparticle to its motional ground state for atom species with lower Doppler temperatures. However, any atom cooling strategy that offers low enough temperatures should allow for motional ground state cooling if there are a sufficient number of atoms.

#### 6.4 Dynamics and cooling of levitated disks

While not strictly a section dedicated to cooling, this section applies nearly all of the ideas and tools covered thus far in this thesis. From large, non-spherical particle scattering and force calculations to ro-translational dynamics and cooling. This section largely follows our publication, Ref. [118].

The choice of particle used in levitated optomechanics is an important factor that depends on the goal of application. The most widely used particle in the field is a silica sphere with radius small compared to the wavelength. The dynamics of spheres trapped in cavities and focused laser beams are well understood and used for cooling to the motional ground state as well as force sensing [26, 34, 38, 143]. This is owing to the simple harmonic translational and free rotational dynamics making it an ideal system to handle for both experimentalists and theorists. As seen in Ch. 4, particles with decreased particle symmetry allow rotational degrees of freedom to enter into the potential energy. A nanorod has large differences in moments of inertia and

polarizability which allows rotations to be described as decoupled librations about the laser polarization axis. The motion of nanodumbbells or generally anisotropic materials requires rigid-body dynamics since these particles have moments of inertia of similar magnitude [55, 76]. As was described in Sec. 2.1, increasing the size of the particle relative to the wavelength of the laser further complicates the motion for any particle shape [100]. Still, from Ch. 4, terms necessary to describe nanorods and nanodumbbells are well understood [54, 77, 81, 123].

Dielectric disks also have a relatively simple shape, but have not seen as much attention as other particle geometries in the literature to date. Several studies point to thin nanodisk scattering being more realistically described in a Rayleigh-Gans rather than a Rayleigh approximation for index of refraction  $n \sim 1$  [62–64]. This generally leads to an orientational dependent shape function in the form of a Bessel function. From studies investigating the applications of disks for various purposes, it is unclear whether there is consensus on the necessity of including the shape function or other non-harmonic terms in the dynamics [46, 61, 144]. There are few experimental studies involving disks, however two such studies suggest terms of higher order may be necessary for describing the motion [145, 146].

In this section it is shown that higher order terms of at least third order in the potential energy are necessary for describing the dynamics of disks outside the Rayleigh regime in a Gaussian standing wave. While a focused Gaussian traveling wave is the most common trap, the large radiation pressure exerted on disks raises the concern for instability. In a Gaussian standing wave (e.g. driven cavity) axial confinement is much stronger and the axial radiation pressure is absent. A disk experiences restoring forces in all three translational degrees of freedom and torques in two rotational degrees of freedom. Similar to rods and nanodumbbells, the rotation about the disk's symmetry axis is unaffected by light coupling and is a constant of the motion. Focus is given to the effects due to the third order terms which provide unique ro-translational couplings that have not yet been discussed in levitated optomechanics. The coupling terms are a result of the finite extension of the disk coupling to both the Gaussian

and standing wave geometry of the beam. Inclusion of the coupling terms results in dynamics with several different modes of oscillation for each degree of freedom which are evident in the power spectral density. Simulations show no evidence of instability.

An analytical as well as numerical approach using a discrete-dipole approximation method is used to identify the forces and torques on disks of radius  $2 \mu\text{m}$  with index of refraction  $n = 1.45$  and  $n = 2.0$  as well as disks of radius  $200 \text{ nm}$  with  $n = 1.45$ . The Gaussian standing wave is constructed with a wavelength  $\lambda = 850 \text{ nm}$  and various waists  $w_0 = 2, 2.5, 3, 4 \mu\text{m}$ .

The coupling terms may hinder or benefit applications for levitated disks. Disks have been proposed as potential accelerometers for gravitational wave detection [46]. The third order coupling terms may complicate determining which degree of freedom experienced a force or torque. On the other hand, it may be used as a means for indirectly detecting the motion of several degrees of freedom with a single detection scheme and therefore an efficient force and/or torque detector. Another common application is cooling the motion of the disk in attempt to study macroscopic quantum mechanics [6, 7, 12]. As energy from one degree of freedom can be transferred to another through the couplings, it may have potential for sympathetically cooling several degrees of freedom by performing a cooling method on only one of the degrees of freedom. Preliminary results show that this is indeed possible for both radii studied using parametric feedback cooling or cold damping. Provided near ground state cooling can be achieved, the multi-mode resonator can further be used to explore entanglement or quantum state transfer [147, 148].

#### 6.4.1 Approximate Analytical Potential Energy

This subsection outlines the analytical calculation of the potential energy of a thin dielectric disk in a Gaussian standing wave in the Rayleigh-Gans approximation. In this approach the disk thickness is taken to be very thin so that the Rayleigh approximation holds along that direction [61, 63]. The approximated results verify

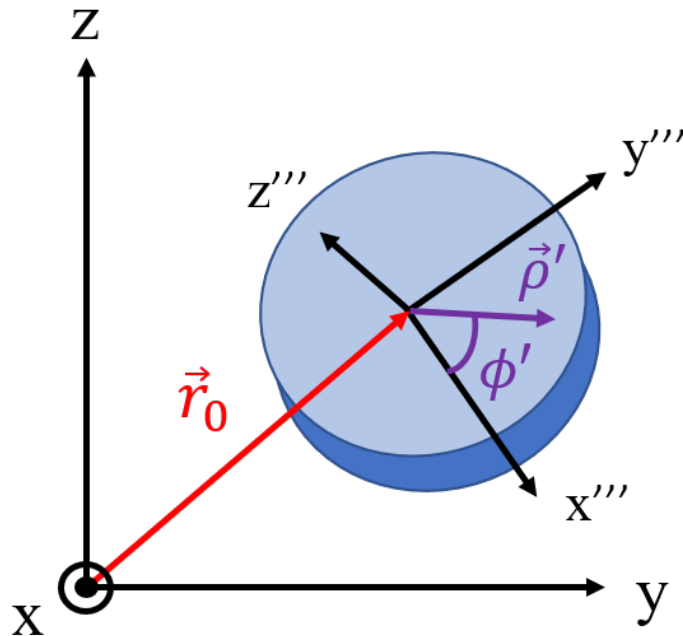


Figure 6.13. Coordinate system in the lab frame  $(x, y, z)$  and the particle frame  $(x''', y''', z''')$ . The disk's symmetry axis is aligned with the particle frame  $z'''$  axis. The disk's center of mass as measured from the lab frame  $\vec{r}_0$  is shown in red. The location to a point on the thin disk is given by the polar coordinates  $(\rho', \phi')$  in the particle frame which are shown in purple.

the existence and helps elucidate the origin of the terms responsible for the dynamics seen in the following sections.

The disk is described with radius  $a$ , thickness  $T \ll \lambda$ , index of refraction  $n$ , and susceptibilities  $\chi_{\parallel} = n^2 - 1$  and  $\chi_{\perp} = \chi_{\parallel}/n^2$  corresponding to the susceptibility parallel and perpendicular to the disk symmetry axis ( $z'''$  axis), respectively [61]. The principal moments of inertia are  $I_z = ma^2/2$  and  $I_x = I_y = m(3a^2 + T^2)/12$ . The disk's center of mass is located at  $\vec{r}_0 = \langle x_0, y_0, z_0 \rangle$  and, as before, rotations are described in terms of the Euler angles  $(\alpha, \beta, \gamma)$  in the  $z - y' - z''$  convention (Ch. 4).

The Gaussian standing wave is formed by two counter-propagating Gaussian waves with non-zero longitudinal components so that they satisfy Maxwell's equations [66]. Each traveling wave has the symmetric waist  $w_0$ , wavenumber  $\vec{k} = (\pm\hat{x})2\pi/\lambda$ , and is polarized in the  $\hat{z}$  direction. Around the focus,  $x = 0$ , each wave takes the form

$$\vec{E}_{\pm}(x, y, z) = E_0 e^{-(y^2+z^2)/w_0^2} \left[ \hat{z} \mp \frac{iz}{x_R} \hat{x} \right] e^{\pm ikx}, \quad (6.49)$$

where  $x_R = kw_0^2/2$  is the Rayleigh range and  $+$  ( $-$ ) stands for the the right (left) traveling wave. The incident fields used for the numerical calculations in Secs. 6.4.2 and 6.4.3 are found by propagating Eq. (6.49) throughout all space using the angular spectrum representation [66]. For the analytical calculations performed in this section the approximated Gaussian standing wave

$$\vec{E}_{\text{inc}}(x, y, z) \approx E_0 e^{-(y^2+z^2)/w_0^2} \left[ \cos kx \hat{z} + \sin kx \frac{z}{x_R} \hat{x} \right], \quad (6.50)$$

is used, which is valid in the space  $|x| \ll x_R$ .

The mechanical potential energy associated with the interaction between the light and the dielectric is

$$U = -\frac{1}{4} \int \vec{P}(r') \cdot \vec{E}(r') d^3r', \quad (6.51)$$

where the integral is over the volume of the disk,  $\vec{P}(r') = \epsilon_0 \overset{\leftrightarrow}{R} \overset{\dagger}{\overset{\leftrightarrow}{\chi}}_0 \overset{\leftrightarrow}{R} \vec{E}(r')$  is the polarization vector,  $\overset{\leftrightarrow}{\chi}_0$  is the diagonal susceptibility matrix in the nanoparticle frame, and  $\overset{\leftrightarrow}{R}$  is the rotation matrix

$$\overset{\leftrightarrow}{R} = \begin{pmatrix} c\beta c\alpha c\gamma - s\alpha s\gamma & c\beta s\alpha c\gamma + c\alpha s\gamma & -s\beta c\gamma \\ -c\beta c\alpha s\gamma - s\alpha c\gamma & -c\beta s\alpha s\gamma + c\alpha c\gamma & s\beta s\gamma \\ s\beta c\alpha & s\beta s\alpha & c\beta \end{pmatrix} \quad (6.52)$$

$$= \begin{pmatrix} R_{11} & R_{12} & R_{13} \\ R_{21} & R_{22} & R_{23} \\ R_{31} & R_{32} & R_{33} \end{pmatrix}, \quad (6.53)$$

where the notation  $c = \cos$ ,  $s = \sin$  was used.

The potential energy in the Rayleigh-Gans approximation with the incident field, Eq. (6.50), becomes

$$U \approx -\frac{E_0^2}{4} \int e^{-2[y^2(r') + z^2(r')]/w_0^2} \times \left[ \cos^2 kx(r') \chi_1 + \sin 2kx(r') \frac{z(r')}{x_R} \chi_2 + \chi_{12} \frac{k^2 z^2(r')}{x_R^2} \sin^2 kx(r') \right] d^3 r', \quad (6.54)$$

where  $\chi_1 = \Delta\chi \cos^2 \beta + \chi_\perp$ ,  $\chi_2 = \Delta\chi \sin \beta \cos \beta \sin \alpha$ ,  $\chi_{12} = \Delta\chi \sin^2 \beta \sin^2 \alpha + \chi_\perp$ , and  $\Delta\chi = \chi_\parallel - \chi_\perp$ . To evaluate Eq. (6.54) the coordinates of the disk must be projected onto each lab frame coordinate  $(x, y, z)$  and it is favorable to move to polar coordinates. First, in the limit  $T \ll \lambda$  the functions in Eq. (6.54) are independent of the thickness leaving the functions in the integral dependent only on the disk's radial and angular coordinates  $(r') = (\rho', \phi')$  (see Fig. 6.13). In terms of the center of mass and disk coordinates,  $x(r')$ ,  $y(r')$ , and  $z(r')$  in Eq. (6.54) are

$$x_i(r') = x_{0,i} + \vec{\rho}' \cdot \hat{x}_i, \quad x_i = (x, y, z), \quad (6.55)$$

with

$$\begin{aligned} \vec{\rho}' &= \overset{\leftrightarrow}{R} \vec{\rho} \\ &= \rho' \left[ \cos \phi' \begin{pmatrix} R_{11} \\ R_{12} \\ R_{13} \end{pmatrix} + \sin \phi' \begin{pmatrix} R_{21} \\ R_{22} \\ R_{23} \end{pmatrix} \right], \end{aligned} \quad (6.56)$$

and the  $R_{ij}$  are matrix components in the rotation matrix  $\overset{\leftrightarrow}{R}$  above. For a disk with negligible thickness, a point on the disk is located at  $\vec{\rho} = \rho(\cos \phi \hat{x} + \sin \phi \hat{y})$  in the body frame. In the lab frame, the point is located at  $\vec{\rho}' = \overset{\leftrightarrow}{R} \vec{\rho} \equiv \langle \rho'_x, \rho'_y, \rho'_z \rangle$  yielding Eq. (6.56).

Insertion of Eqs. (6.55) and (6.56) into Eq. (6.54) leads to analytic solutions in terms of Bessel functions. In the limit of small radius  $w_0 \gg a$ ,  $r_0 a \ll w_0^2$  where the zeroth order approximation to the exponentials ( $\sim 1$ ) can be used, a Bessel function of the first kind is obtained as was found in Ref. [61]. However, this approximation

misses the coupling of the disk to the Gaussian standing wave and a fourth order expansion in the coordinates is required to resolve it.

Practical parameters in levitated optomechanics are in the range  $(\lambda, w_0) \sim 1 \mu\text{m}$  and  $(r_0, a) \sim 1 - 0.1 \mu\text{m}$ . To complete the derivation, the limits  $a^2 \ll w_0^2$ ,  $r_0^2 \ll w_0^2$  are used to expand each function in Eq. (6.54) to fourth order in the coordinates and terms  $\mathcal{O}(a^6/w_0^6)$  as well as  $\mathcal{O}(x_{0,i}^n \pi_j^m)$ , where  $n + m \geq 4$ ,  $\pi_j = (\alpha, \beta)$ , are dropped which retains terms up to third order in the coordinates. Due to the symmetry of the disk, the potential energy is independent of the angle  $\gamma$ . Further, the disk's symmetry axis is primarily aligned along the lab frame  $\hat{x}$  direction and, as will be justified in the next section, rotates at angles that justify the small angle approximation  $\alpha \rightarrow 0 + \theta_z$ ,  $\beta \rightarrow \pi/2 + \theta_y$  with  $\theta_z, \theta_y$ , small. Here  $\theta_z$  represents small angle rotations about the lab frame  $z$  axis while  $\theta_y$  is a small rotation about the lab frame  $y$  axis.

Expanding each function in Eq. (6.54) to first order gives

$$\begin{aligned}
U = & -\frac{TE_0^2}{4} \left[ 1 - \frac{2\rho_0^2}{w_0^2} \right] \int_0^a \rho' d\rho' \int_0^{2\pi} d\phi' \\
& \times \left[ 1 - \frac{2}{w_0^2} (\rho_y'^2 + \rho_z'^2) \right] \\
& \times \left[ 1 - \frac{4}{w_0^2} (y_0\rho_y' + z_0\rho_z') \right] \\
& \times \left[ \chi_1 \left( 1 - \frac{k^2}{2} (x_0 + \rho_x')^2 \right)^2 \right. \\
& + \chi_2 \frac{2k}{x_R} (z_0 + \rho_z') (x_0 + \rho_x') \\
& \left. + \chi_{12} \frac{k^2}{x_R^2} (z_0 + \rho_z')^2 (x_0 + \rho_x')^2 \right], \tag{6.57}
\end{aligned}$$

where the integral over the thickness was performed. Odd powers of  $\rho'_i \rho'_j$  integrate to zero from the  $\phi'$  dependence. The resulting potential energy is of the form

$$\begin{aligned}
U \approx & \frac{m}{2} (\omega_x^2 x_0^2 + \omega_y^2 y_0^2 + \omega_z^2 z_0^2) + \frac{I_x}{2} (\omega_{\theta_y}^2 \theta_y^2 + \omega_{\theta_z}^2 \theta_z^2) \\
& + mx_0 (\omega_1^2 y_0 \theta_z - \omega_2^2 z_0 \theta_y), \tag{6.58}
\end{aligned}$$

and the analytical frequencies are

$$\omega_x^2 = \eta k^2 \chi_\perp [1 - A], \quad (6.59)$$

$$\omega_y^2 = \omega_z^2 = \frac{2\eta\chi_\perp}{w_0^2} [1 - A], \quad (6.60)$$

$$\omega_{\theta_y}^2 = \frac{4\eta}{a^2} \left[ \Delta\chi (1 - 2A) - \frac{k^2 a^2 \chi_\perp}{8} \right], \quad (6.61)$$

$$\omega_{\theta_z}^2 = \frac{\eta k^2 \chi_\perp}{2}, \quad (6.62)$$

$$\omega_1^2 = \eta \left[ 2k^2 A \chi_\perp - \frac{\Delta\chi_\perp}{w_0^2} \right], \quad (6.63)$$

$$\omega_2^2 = 2\eta k^2 A \chi_\perp, \quad (6.64)$$

where the common factor  $\eta = \frac{2\epsilon_0 E_0^2}{\rho}$  with  $\rho$  the mass density, the moment of inertia for negligible thickness  $I_y = I_x = ma^2/4$  was used, and  $A = a^2/4w_0^2$  is one quarter the square ratio of the radius to the waist.

The terms in the first row in Eq. (6.58) describe simple harmonic motion for the three translational and two rotational degrees of freedom. The last term is a coupling between the translational and rotational degrees of freedom that is of third order in the coordinates. The coupling terms arise due to the finite radius of the disk and the Gaussian and standing wave geometry of the beam. An asymmetric electric field gradient across the disk produces a stronger force on the section of the disk with greater laser intensity. That section of the disk is pulled into the region of the trap with greater laser intensity more strongly than the section of the disk with less field intensity. As the radius increases and the trap becomes more confining, the greater the electric field gradient across the disk and the more influential the coupling terms are. With reference to Eq. (6.54), it is a result of the ro-translational coupling in the Gaussian together with the  $x_0$  dependence in  $\cos^2 kx(r')$  describing the standing wave. From rows 3 and 4 in Eq. (6.57),

$$(y_0 \rho'_y + z_0 \rho'_z) (x_0 + \rho'_x)^2 \quad (6.65)$$

$$\propto (y_0 \rho'_y + z_0 \rho'_z) (x_0 \rho'_x) \quad (6.66)$$

$$\propto -x_0 (y_0 \theta_z - z_0 \theta_y). \quad (6.67)$$

The asymmetry in the  $(\omega_1, \omega_2)$  coefficients is due to the  $\hat{x}$  component of the incident electric field proportional to  $z_0/x_R$ . If this term is negligible,  $x_R \gg z_0$ , the coefficients are equivalent,  $\omega_1 = \omega_2$ .

To garner an idea of the dynamics that arise due to the coupling, consider the  $x_0 y_0 \theta_z$  term in Eq. (6.58). A disk displaced by  $\vec{r}_0 = \langle x_0, y_0, 0 \rangle$  in Fig. 6.13 experiences a torque about the  $-z$  axis due to a greater electric field intensity on the side of the disk nearest the focus. These terms are therefore a gradient force/torque as a consequence of the electric field gradient along the finite extension of the disk.

In experiments the beam waists in the  $z$  and  $y$  directions are often not symmetric. The asymmetric Gaussian leads the frequencies above to be altered slightly and can be accounted for by using different beam waists in Eq. (6.57).

One noteworthy feature in Eq. (6.62) is that the  $\omega_{\theta_z}$  rotational frequency depends on  $\chi_{\perp}$  rather than  $\Delta\chi$ . Rotational frequencies in the Rayleigh approximation depend on  $\Delta\chi$  solely as was seen in Ch. 4 as the particle's long axis tries to align with the electric field. In the Rayleigh approximation  $\omega_{\theta_z} = 0$  and is only non-zero here due to the electric field gradient across the finite extension of the disk.

## 6.4.2 Numerical Evaluation of the Forces and Torques

### System and Procedure

The optical scattering problem for finite sized dielectric objects is generally difficult to solve analytically. As was done in the previous section, approximations are often required to glean insight into the dynamics. Another rigorous approach is to numerically solve for the scattered electromagnetic waves and use the resulting Maxwell stress tensor to obtain the forces and torques. This section details the results from performing the latter method by numerically implementing the discrete-dipole approximation (DDA) to calculate the scattered fields of the disk [58, 101].

In the DDA, the disk is composed of  $N$  discrete spherical dipoles each with polarizability  $\alpha$  and the internal fields of the dielectric are solved for self-consistently to re-

trieve the scattered fields outside the particle. In the implementation of the DDA, each dipole that composed the spherical dipole had a polarizability  $\alpha = 4\pi\epsilon_0 R^3 \left( \frac{n^2 - 1}{n^2 + 2} \right)$ . This is the same approach that was used to calculate the shot noise heating rate in a focused Gaussian beam in Sec. 5.2.5. The scattered fields that are generated from the DDA are then added to the incident field and inserted into the Maxwell stress tensor [49]

$$T_{ij} = \epsilon_0 \left[ E_i E_j + c^2 B_i B_j - \frac{1}{2} \left( |\vec{E}|^2 + c^2 |\vec{B}|^2 \right) \delta_{ij} \right], \quad (6.68)$$

in order to obtain the forces and torques

$$\vec{F} = \oint \vec{T} \cdot \hat{n} dS, \quad (6.69)$$

$$\vec{\tau} = \oint \vec{M} \cdot \hat{n} dS, \quad (6.70)$$

where  $\vec{M} = -\vec{T} \times \vec{r}$ . The surface over which the integration is performed was taken to be a sphere centered at the disk center with radius  $1.5\times$  that of the disk. The surface integration was performed using Gaussian quadrature with increasing number of points until convergence was demonstrated.

The above procedure was performed for dielectric disks located near the intensity maximum of a Gaussian standing wave. To construct the standing wave, a right-traveling wave,  $\vec{E}_R(x, y, z)$  is found by propagating Eq. (6.49) throughout all space using the angular spectrum representation with no paraxial approximation. A left-traveling wave,  $\vec{E}_L(x, y, z) = \vec{E}_R(-x, -y, z)$ , is added to the right-traveling wave to form the standing wave. The wavelength of each wave is  $\lambda = 850$  nm and is fixed throughout this section. While the detailed coefficients of the forces and torques change with wavelength the major results of this section do not, and 850 nm is an efficient emission wavelength for GaAs quantum well gain media used in semiconductor lasers [149]. A range of Gaussian beam waists were explored  $w_0 = 2, 2.5, 3, 4$   $\mu\text{m}$  to define the optical trap.

Most of the calculations performed were for disks of radius  $a = 2$   $\mu\text{m}$ , thickness  $T = \lambda/4n$  to achieve maximum light coupling, and index of refraction  $n = 1.45$  or  $n = 2.0$ . The indices of refraction correspond to materials composed of silica and

silicon nitride, respectively. Unless otherwise stated, the data and discussions that follow will refer to this set of parameters.

The following example outlines the steps for how a calculation is performed: the disk's symmetry axis is aligned with the axial direction ( $x$  axis), the disk is displaced a distance  $y_0$  from the focus of the standing wave, the scattered waves are calculated using the DDA, the forces and torques are computed using Eqs. (6.69) and (6.70). The process is identical for rotations: the disk is initially situated at  $\vec{r}_0 = \langle 0, 0, 0 \rangle$  and  $(\alpha = 0, \beta = \pi/2)$ , a rotation is made  $\alpha = 0 + \theta_z$ , the scattered waves are calculated using the DDA, the forces and torques are calculated. The baseline for the calculations is when the disk is placed symmetrically at the focus of the standing wave,  $\vec{r}_0 = \langle 0, 0, 0 \rangle$ ,  $(\alpha = 0, \beta = \pi/2)$  which should be a potential minimum. Indeed, a force or torque due to a displacement generally gives a value at least ten orders of magnitude greater than the baseline.

## Forces and Torques

As is expected in levitated optomechanics, small displacements in one direction reveals a spring force in that same direction  $F_i = -k_i x_{i,0}$  and torque  $\tau_i = -\kappa_i \pi_i$ ,  $\pi_i = (\alpha, \beta)$ . The spring constants for each degree of freedom,  $(k_i, \kappa_i)$ , are determined by direct division,  $k_i = -F_i/x_{i,0}$ . At the harmonic level, no coupling of the different degrees of freedom through the potential energy were found.

Being that there are 6 degrees of freedom (including  $\gamma$ ), there are 15 different second order couplings possible in the forces and torques. Of these possibilities, only terms similar to that in Eq. (6.58) were found to be above the baseline. These terms were found to be significant for disks of large and small radii. For example, a displacement of the center of mass by  $\vec{r}_0 = \langle x_0, 0, z_0 \rangle$  produces a torque about the  $y$  axis, suggesting a term in the potential energy  $U \propto D_1 y_0 z_0 \theta_y$ , with  $D_1$  a proportionality constant. A similar coupling of the same order was found  $U \propto D_2 x_0 y_0 \theta_z$ , with  $D_2 \neq D_1$  necessarily. The coefficients  $D_1$  and  $D_2$  are also determined by division, i.e.

Table 6.2.

Frequencies for a silica disks of radius  $a = 200$  nm and thickness  $T = \lambda/(40n)$  for two beam waists  $w_0 = 2, 3 \mu\text{m}$ . The disk has dimensions that are reduced by a factor of ten from the  $a = 2 \mu\text{m}$ ,  $T = \lambda/(4n)$  disks. A fixed total power of 100 mW is used for the calculations. The number of points used to compose the disk was  $N = 37488$  and the thickness of the disk was 4 points.

$w_0$ ( $\mu\text{m}$ )	$\omega_x$ (kHz)	$\omega_y$ (kHz)	$\omega_z$ (kHz)	$\omega_{\theta_y}$ (kHz)	$\omega_{\theta_z}$ (kHz)	$\omega_1$ (kHz)	$\omega_2$ (kHz)
2	394	38	38	537	390	46	39
3	264	17	17	361	263	21	17

$D_1 = F_z/(y_0\theta_x)$ . Interestingly, the coefficients computed in this way generally gives different values for the force in the  $\hat{y}$  and  $\hat{z}$  directions

$$F_y \propto -Ax_0\theta_z, \quad (6.71)$$

$$F_x \propto -C_1y_0\theta_z, \quad (6.72)$$

$$\tau_z \propto -C_1x_0y_0, \quad (6.73)$$

for the first coupling term, and

$$F_z \propto Bx_0\theta_y, \quad (6.74)$$

$$F_x \propto C_2z_0\theta_y, \quad (6.75)$$

$$\tau_y \propto C_2x_0z_0, \quad (6.76)$$

for the second coupling term, with  $A \approx C_1$  and  $B \approx C_2$ . The coefficients  $A$  and  $B$  can differ from  $C_1$  and  $C_2$  by 2% using a waist of  $w_0 = 2 \mu\text{m}$  and 20% using a waist of  $w_0 = 4 \mu\text{m}$ . Although the discrepancy is suspected to be due to higher order terms, we are only interested in the dynamics due to this term and the average values  $D_1 = (A + 2C_1)/3$  and  $D_2 = (B + 2C_2)/3$  will be used from here on so that potential energy can be written in the form of Eq. (6.58). The consequences of using the average values is insignificant and will be discussed in Sec. 6.4.3.

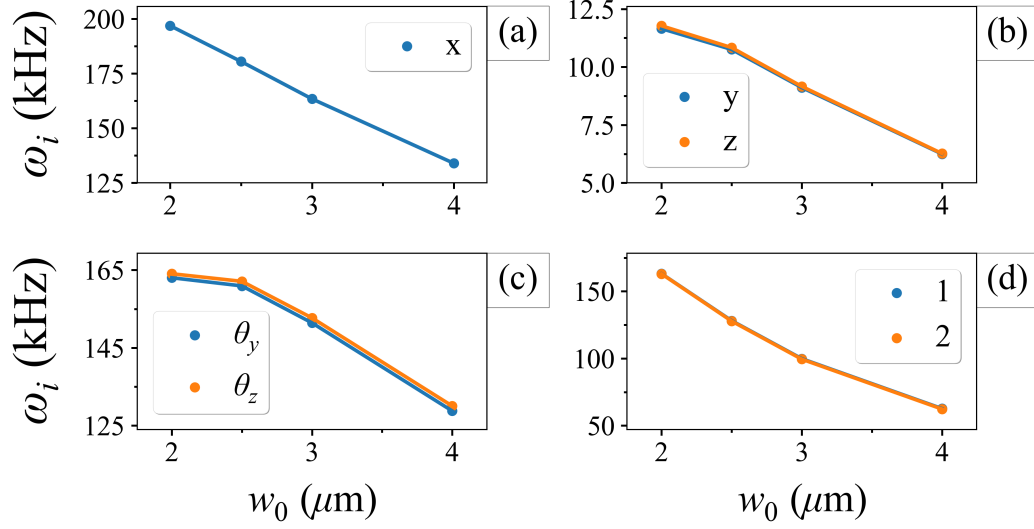


Figure 6.14. Frequencies obtained using the DDA for silica disks ( $n=1.45$ ) of radius  $a = 2 \mu\text{m}$  and thickness  $T = \lambda/(4n)$  for varying beam waist. Frequencies are shown for the (a)  $x$ , (b)  $y$  and  $z$ , (c)  $\theta_y$  and  $\theta_z$  degrees of freedom and the coupling constants in (d). A fixed total power of 100 mW is used for the calculations. For each calculation the disk was composed of  $N = 299744$  points with a thickness of 8 points.

The spring and coupling constants ( $k_i, \kappa_i, D_i$ ) have the same units and are most useful when written in terms of frequencies

$$\omega_i = \sqrt{k_i/m}, \quad i = (x, y, z), \quad (6.77)$$

for translational harmonic motion,

$$\omega_i = \sqrt{\kappa_i/I_x}, \quad i = (\theta_y, \theta_z), \quad (6.78)$$

for rotational harmonic motion, and

$$\omega_i = \sqrt{D_i/m}, \quad i = (1, 2), \quad (6.79)$$

for the coupling terms.

Values for the frequencies as a function of beam waist are shown in Fig. 6.14 for silica and Fig. 6.15 for silicon nitride using a fixed total laser power of 100 mW.

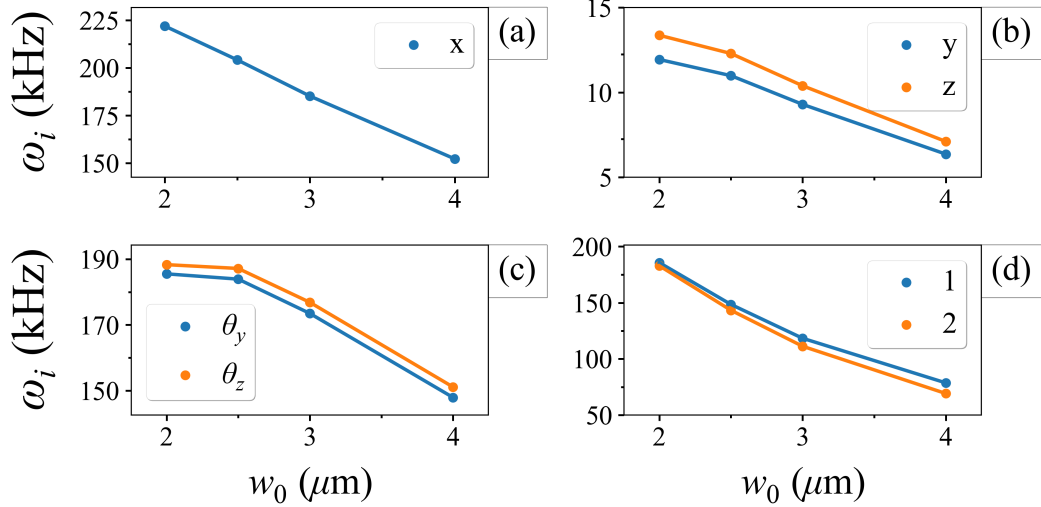


Figure 6.15. Frequencies obtained using the DDA for silicon nitride disks ( $n=2.0$ ) of radius  $a = 2 \mu\text{m}$  and thickness  $T = \lambda/(4n)$  for varying beam waist. Frequencies are shown for the (a)  $x$ , (b)  $y$  and  $z$ , (c)  $\theta_y$  and  $\theta_z$  degrees of freedom and the coupling constants in (d). A fixed total power of 100 mW is used for the calculations. For each calculation the disk was composed of  $N = 569984$  points with a thickness of 8 points.

The general trend identified from the figures is that each frequency decreases as the waist increases. This feature is not unexpected, however, for particles in the Rayleigh regime  $\lambda \gg a$ ,  $\omega_i \propto 1/w_0^2$  while for  $a = 2 \mu\text{m}$  disks the dependence is nearly linear.

For both materials, the frequency in the axial direction is in the 150 – 200 kHz range while the radial degrees of freedom oscillate in the 1 – 10 kHz range. The axial frequency is most strongly affected by the standing wave which is independent of the waist. However, the radial frequencies are dominantly due to the Gaussian geometry. To leading order (see Sec. 6.4.1), for fixed power the axial frequencies depend inversely on the wavelength and waist  $\omega_x \propto 1/\lambda w_0$  while the radial frequencies depend on the waist as  $\omega_{y,z} \propto 1/w_0^2$ , hence the disparity between the axial and radial frequencies. Note that part of the waist dependence on each frequency is due to the dependence of the laser intensity on the waist. Each frequency therefore shares a  $1/w_0$  dependence from the power.

For a  $2 \mu\text{m}$  radius disk at  $T = 300 \text{ K}$ , these frequencies correspond to translational oscillation amplitudes of  $x_0 \sim 1 \text{ nm}$  and  $(0, y_0, z_0) \sim 20 \text{ nm}$ . The rotational frequencies are closer to the axial frequency and in the range  $190 - 125 \text{ kHz}$ . The rotational frequencies differ by 20% between the two materials at the same waist. Using the average frequency, this corresponds to angular displacements of  $\sim 1 \text{ mrad}$ . Displacements of this size justify some of the approximations made in Sec. 6.4.1 since  $r_0 \ll w_0$  and  $\sin \alpha \approx \theta_z$ .

Also shown in Figs. 6.14 and 6.15 are the coupling coefficients  $(\omega_1, \omega_2)$ . The coefficients being in the  $50 - 200 \text{ kHz}$  range are comparable to both the rotational and axial frequencies. Due to the large coupling frequencies combined with the relatively large oscillation amplitude in the radial degrees of freedom, the resulting forces/torques due to the coupling terms have an impact on the dynamics as shown in Sec. 6.4.3.

Force and torque calculations were also performed for silica disks of radius  $a = 200 \text{ nm}$  and thickness  $T = \lambda/(40n)$  for the two beam waists  $w_0 = 2, 3 \mu\text{m}$ . The dimensions are  $10\times$  smaller than the  $a = 2 \mu\text{m}$ ,  $T = \lambda/(4n)$  disk. The resulting frequencies are shown in Table 6.2. From the table, each frequency scales as  $\omega_i \sim 1/w_0$  except for the radial frequencies  $(\omega_y, \omega_z) \sim 1/w_0^2$ . This dependence on the waist is consistent with the analytical frequencies given in Sec. 6.4.1. Also from the table, each harmonic frequency is larger, and the coupling frequencies reduced, compared to its  $a = 2 \mu\text{m}$  and  $T = \lambda/(4n)$  counterpart in Fig. 6.14. The dependence of each frequency on the radius is also consistent with that found analytically in Sec. 6.4.1. The harmonic frequencies increase as the radius decreases since the disk has greater field intensity per volume. The coupling frequencies scale as  $\sim a/w_0^2$  due to the electric field gradient across the disk. This dependence provides a factor of ten between the  $a = 200 \text{ nm}$  and  $a = 2 \mu\text{m}$  coupling frequencies.

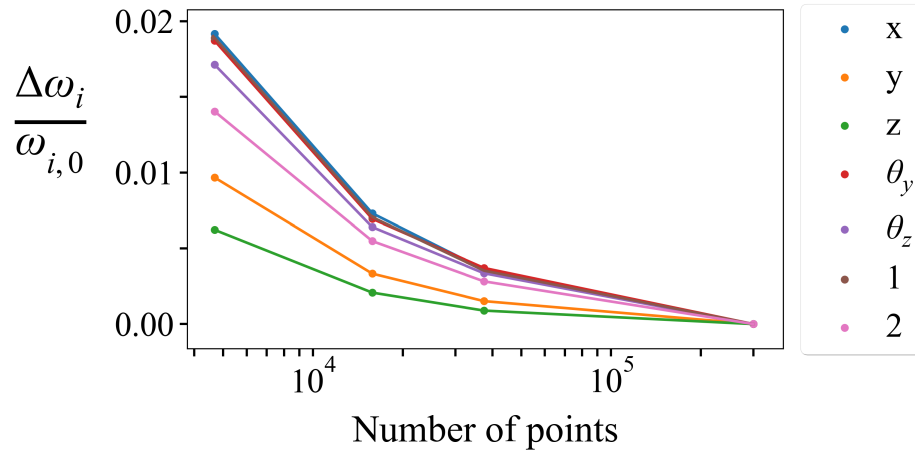


Figure 6.16. Frequencies obtained for a  $a = 2 \mu\text{m}$  silica disk using DDA for varying number of points that the disk was composed of relative to the frequency obtained using 299744 points,  $\omega_{i,0}$ . The legend describes the various frequencies for the  $x, y, z, \theta_y, \theta_z$  degrees of freedom as well as the  $\omega_1, \omega_2$  coupling frequencies. The data points along the  $x$ -axis are 4680, 15804, 37488, and 299744 points. Comparing the left and rightmost data points in the figure shows that using 64 times more points changes the frequencies by less than 2%.

### Accuracy of the DDA

The frequencies shown in Sec. 6.4.2 were obtained through several numerical operations such as integrations and the implementation of the DDA. One of the major questions regarding convergence of these values is how many points (i.e. number of discrete dipoles),  $N$ , should be used to discretize the disk. Figure 6.16 shows the relative change of the various frequencies discussed in the previous subsections as a function of the number of points used to compose the disk. Here,  $\omega_{i,0}$  is the frequency calculated using the largest number of points shown in the plot,  $N = 299744$ . The frequency calculated using  $N$  points is  $\omega_i$ . The change in the frequency  $\omega_i$  compared to  $\omega_{i,0}$  points is then  $\Delta\omega_i = \omega_i - \omega_{i,0}$ . The plot is shown for all of the various frequencies discussed above using a  $a = 2 \mu\text{m}$  silica disk with a  $w_0 = 2 \mu\text{m}$  waist. Increasing the number of points by a factor of 64 from  $N = 4680$  to  $N = 299744$

changes the frequency by less than 2%. On the other hand, the time complexity of the DDA method used to calculate the scattered light from the disk scales as  $N \ln N$ .

### 6.4.3 Dynamics

The previous two sections have illustrated that disks levitated in Gaussian standing waves experience simple harmonic motion as well as non-harmonic forces and torques involving second order couplings. This section discusses the resulting dynamics due to these forces and torques as well as the natural torques that arise in rigid body dynamics.

Thus far the focus has been on identifying terms in the potential energy. For translational motion the kinetic energy is trivial and leads to the equations of motion

$$\ddot{x} = -\omega_x^2 x - (\omega_1^2 y \theta_z - \omega_2^2 z \theta_y), \quad (6.80)$$

$$\ddot{y} = -\omega_y^2 y - \omega_1^2 x \theta_z, \quad (6.81)$$

$$\ddot{z} = -\omega_z^2 z + \omega_2^2 x \theta_y, \quad (6.82)$$

for small angle oscillations.

As was shown in Ch. 4, for a symmetric-top rigid body the rotational kinetic energy naturally involves coupling between the  $\alpha, \dot{\alpha}, \beta,$  and  $\dot{\beta}$  degrees of freedom. Whether these terms are significant or not depends on the geometry. For  $a = 200$  nm disks each non-linear coupling term is significant and must be considered. For  $a = 2 \mu\text{m}$  disks, the term responsible for precession about the  $x$  axis is the largest, but is still  $10^{-4}$  times smaller than the harmonic term and is therefore negligible. The equations of motion for  $a = 2 \mu\text{m}$  disks are then written as

$$\ddot{\theta}_y = -\omega_{\theta_y}^2 \theta_y + \frac{m}{I_x} \omega_2^2 x z, \quad (6.83)$$

$$\ddot{\theta}_z = -\omega_{\theta_z}^2 \theta_z - \frac{m}{I_x} \omega_1^2 x y, \quad (6.84)$$

$$\dot{\gamma} = \omega_3 = \text{const}, \quad (6.85)$$

for small angle oscillations.

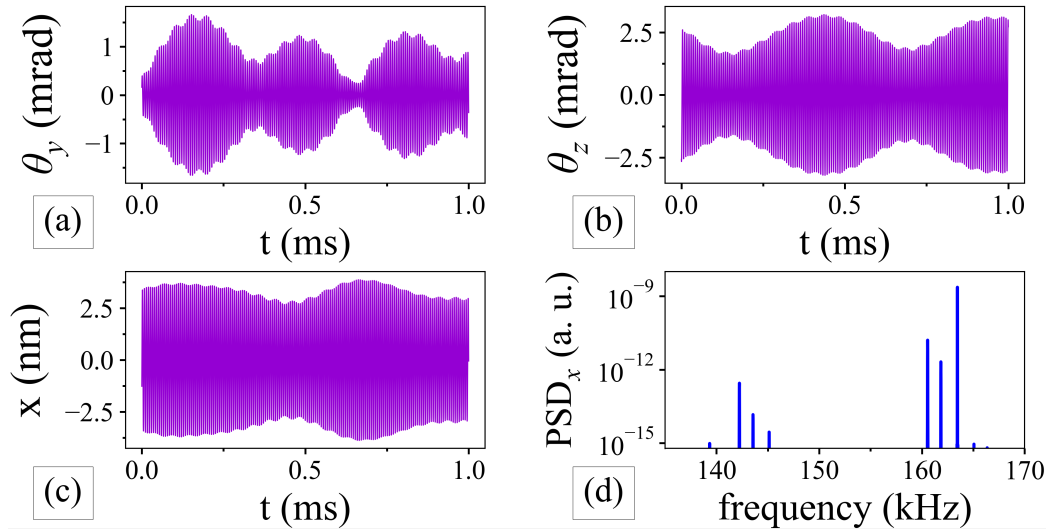


Figure 6.17. Example trajectories of the (a)  $\theta_y$ , (b)  $\theta_z$ , and (c)  $x$  degrees of freedom as well as (d) the power spectral density of the axial motion ( $x$ ) for a  $a = 2 \mu\text{m}$  silica disk in a  $w_0 = 3 \mu\text{m}$  waist trap. The influence of the second order coupling term produces several amplitude modulations at different frequencies, but the disk remains stable. The frequencies of modulation in the  $x$  degree of freedom can be seen in the power spectral density. Note that the rotational amplitudes remain in the  $\sim \text{mrad}$  range, justifying the small angle approximation.

Figure 6.17 shows sample trajectories of the  $\theta_y$ ,  $\theta_z$ , and  $x$  motions of a  $a = 2 \mu\text{m}$  silica disk in a  $w_0 = 3 \mu\text{m}$  waist Gaussian standing wave by simulating Eqs. (6.80) to (6.84) at  $T = 300 \text{ K}$ . The influence of the second order coupling terms are seen to be significant for the three degrees of freedom with each trajectory containing modulations at various frequencies. Without the couplings the oscillations would be at the same amplitude for all times. In a gaseous environment these modulations might be mistaken for noise in an experiment.

The bottom-rightmost plot in Fig. 6.17 shows the power spectral density (PSD) of the  $x$  motion. The harmonic frequency  $\omega_x/2\pi = 163 \text{ kHz}$  is the largest and rightmost peak in the PSD. The other frequencies in the figure are the harmonic frequency plus the sums and differences of the various  $y$ ,  $z$ ,  $\theta_y$ , and  $\theta_z$  frequencies. Whereas sidebands

due to coupling typically appear symmetrically on each side of the harmonic frequency, the frequency structure seen in Fig. 6.17 is such that all significant modes have smaller frequency than the harmonic frequency. This is not a general feature of the coupling term and depends on the degree of freedom that is being observed and the various levels of degeneracy.

In their analysis of disks as gravitational wave detectors, Ref. [46] considered plane waves to form the standing wave in which case the couplings would be absent (see Sec. 6.4.1). A single peak in the PSD can then be used to describe a translational degree of freedom. However, a Gaussian standing wave is needed to trap the non-axial degrees of freedom and therefore should be considered. A concern then for the disks ability to be a detector is the extra 'noise' the degree of freedom being observed for detection of the wave will have. If there is a disturbance in one of the degrees of freedom, the degree of freedom being observed for gravitational waves will also be disturbed to some degree that depends on the coupling.

The influence of the coupling term on each degree of freedom has two factors: the size of the coefficients  $\omega_1$  and  $\omega_2$ , and the level of degeneracy of the coupled degrees of freedom. First, the  $\omega_1$  and  $\omega_2$  coupling coefficients are relatively large  $\sim 100$  kHz. Second, strong coupling is achieved when the frequencies are nearly degenerate. Because  $\omega_x$ ,  $\omega_{\theta_y}$ , and  $\omega_{\theta_z}$  are close in frequency the coupling term produces a larger effect on these degrees of freedom. Since the radial degrees of freedom oscillate  $10\times$  slower, the influence of the coupling term is significantly reduced, but not absent.

The question of stability is one of the most important for applications using levitated nanodisks. Despite the seemingly complicated motion, simulations have shown no evidence that this motion is unstable. The disk remains stable in the trap after several thousand oscillations for all of the beam waists explored  $w_0 = 2, 2.5, 3, 4 \mu\text{m}$ . The  $a = 200$  nm disk was found to be stable at all frequencies, even with inclusion of the non-linear coupling terms in the rotational kinetic energy [76]. Recall from Sec. 6.4.2 the differing coefficients in Eqs. (6.71) to (6.76) as produced from the DDA

calculations. Simulating the equations of motion with different coefficients attached to each degree of freedom's coupling term causes no issue for stability.

A common application in levitated optomechanics is cooling the motion of the levitated particle in attempt to reach the ground state, or to reach lower pressures [143]. The couplings found for the disk offer a possibility of cooling one or more degrees of freedom sympathetically by actively cooling only one degree of freedom. The full dynamics of cooling using the couplings is to be explored in a future work, but we note some preliminary findings. Through simulations of the equations of motion Eqs. (6.80) to (6.84), results show that sympathetic cooling is indeed possible. For both radii, parametric feedback or cold damping [22, 23] is an effective method for cooling multiple degrees of freedom. By inserting artificial numbers for the frequencies in the simulation, two relations were found for optimal cooling. Frequencies tailored within a few kHz of the relations  $\omega_x = \omega_{\theta_y} \pm \omega_z$  and/or  $\omega_x = \omega_{\theta_z} \pm \omega_y$ , can achieve significant sympathetic cooling to at least the mK regime. From Fig. 6.14,  $a = 2 \mu\text{m}$  silica disks are naturally in this regime. From Sec. 6.4.1, each frequency depends on several parameters and has the possibility to be tuned to achieve optimal cooling experimentally.

#### 6.4.4 Conclusion

The forces and torques exerted on dielectric disks trapped in a Gaussian standing wave were analyzed for disks of radius  $2 \mu\text{m}$  with index of refraction  $n = 1.45$  and  $n = 2.0$  as well as disks of radius  $200 \text{ nm}$  with  $n = 1.45$ . Calculations of the forces and torques were conducted both analytically and under numerical simulation using a discrete-dipole approximation method.

Similar to nanodumbbells, a nanodisk experiences restoring forces in all three translational degrees of freedom, restoring torques in two rotational degrees of freedom, and has constant spin about the symmetry axis. Due to the finite geometry of the disk, third order, ro-translational coupling terms in the potential energy are

found to be a necessary consideration when describing the dynamics of disks. The coupling terms are the result of an electric field gradient across the disk and depend on the ratio of the radius to the beam waist and on the temperature.

The ro-translational coupling produces several modes of oscillation in the coupled degrees of freedom which are evident in the power spectral density. While the restoring forces are dominant, the coupling terms can become sizable through strong coupling, which manifests when the coupled degrees of freedom are nearly degenerate. Despite the couplings, simulations show no evidence that the motion is unstable, which is of utmost importance for applications such as gravitational wave detection, force sensing, and ground state cooling.

## 7. SUMMARY AND OUTLOOK

This thesis covered a small portion of the rapidly growing field of levitated optomechanics and highlighted some of my published work in the field [76, 77, 92, 118, 119]. Chapter 3 discussed the well-known translational dynamics of a spherical particle trapped in the focus of an optical tweezer. It was shown that the conservative optical gradient force, which yields three dimensional harmonic trapping, and the dissipative scattering force due to radiation pressure dominate the dynamics for the majority of particles in levitated optomechanics. The modern method by which experimentalists measure the particle motion in real-time was calculated analytically in Sec. 3.3.

In Chap. 4, the classical and quantum dynamics of a symmetric-top particle (e.g. a nanodumbbell) in a linearly polarized laser beam were shown to describe harmonic oscillations as well as precession about the laser polarization axis. The precession motion is a consequence of the non-zero angular momentum about the particle's symmetry axis which is a conserved quantity. Necessary for feedback cooling, a common method for measuring the orientation of the particle was also calculated in Sec. 4.3.

Chapter 5 discussed the common sources of decoherence and noise present in an optically levitated system with a focus on the damping and noise due to gas collisions as well as laser shot noise. Incorporation of the effects into the particle motion can be achieved using Langevin dynamics. Beginning from conservation of energy and momentum, the energy delivered to a particle from laser shot-noise was found to depend on the scattered radiation pattern as well as the incident wave's propagation direction. The energy in each degree of freedom increases per scattering event, but with different proportionality constants. These proportionality constants carry over to the average heating rate for each degree of freedom. Analytical expressions for the shot noise heating rate were provided in the Rayleigh limit as well as numerical calculations

for particles in the Mie regime for silica and diamond. The shot noise heating in each degree of freedom was also computed for silica Mie particles at the focus of strong and weakly focused Gaussian beams. For finite sized silica nanospheres, the values of the shot noise obtained for an incident focused Gaussian beam are within an order of magnitude of the Rayleigh expression for each degree of freedom. The discrepancy increases as the radius of the particle and/or the numerical aperture of the lens increases. The Rayleigh expression may serve as a good approximation and upper bound as it is typically larger than the rates found for particles with finite radius. The rotational shot noise due to linear, elliptical, and unpolarized light was calculated for symmetric-top particles in the Rayleigh regime using quantum decoherence theory. The results show the amount of heating in each degree of freedom is different depending on the degree of ellipticity. As it is not contained within the polarization vector, no energy is transferred to the degree of freedom associated with motion about the particle's symmetry axis. These results are crucial for experimental tests of heating and noise due to fundamental noise sources such as that expected by the continuous spontaneous localization model.

In Chap. 6 three new possible methods of cooling a particle's motion were presented together with an analysis of an experiment that performed ro-translational cooling on a levitated nanodumbbell. From Sec. 6.1, cooling a nanodumbbell's librational modes completely using parametric feedback cooling is only possible if the two librational frequencies are different with a larger separation giving a larger cooling rate. This can be achieved by using elliptically polarized light. Cooling with linear polarization allows cooling of one precessional mode while the remaining mode describes pure precession about the laser polarization axis.

Section 6.2 examined the experimental findings of cooling a levitated nanodumbbell's three translational and two rotational degrees of freedom using force feedback (cold damping). The dynamics of the dumbbell were found to be consistent with the theoretical analysis found in Secs. 4.1 and 6.1. Two peaks were found in the power spectral density while measuring each librational coordinate. As the spin about the symmetry

axis is uncoupled to the laser, its motion is entirely Brownian due to collisions with the surrounding gas. As the two librational coordinates are coupled through the spin about the symmetry axis, the two peaks were observed to shift in time in accordance with the Brownian motion of the spin.

The second theoretical cooling scheme in Sec. 6.3 explored the validity of cooling the translational motion of a magnetic nanosphere coupled to a Doppler cooled, spin-polarized atomic gas via the magnetic dipole-dipole interaction. The nanosphere may experience significant cooling for  $> 10^4$  atoms. The method has potential to exceed the cooling rates of modern cooling methods yielding cooling rates  $\sim 10$  kHz for a sufficient number of atoms  $\sim 10^6$ . As the particle will thermalize with the atom cloud, reaching the particle ground state is possible if an atom cooling strategy is able to reach temperatures below the particle ground state temperature.

Lastly, in Sec. 6.4 the dynamics of dielectric disks trapped in a Gaussian standing wave outside of the Rayleigh regime were computed. Terms in the potential energy up to third order in the coordinates were computed both analytically and numerically using a discrete dipole approximation method. While the translational and rotational dynamics of disks are dominated by harmonic terms similar to those of a symmetric-top particle in the Rayleigh regime, the third order terms are significant for coupling degrees of freedom with similar harmonic frequencies, a common occurrence in levitated optomechanics. The third order ro-translational coupling terms show no evidence of instability and produce multiple modes evidenced through the power spectral density. The coupling terms offer multi-modal cooling by actively cooling one degree of freedom and provide a platform for entanglement or quantum state transfer.

The future outlook of the field of levito-dynamics is bright considering the swift advancements in understanding since its fervent exploration since the year 2010. The investigations described above are ideas that may, with careful undertaking, allow a levitated nanoparticle to breach unknowns in physics and human understanding. The rapid understanding of the means by which to trap and manipulate particles

in various trap designs have advanced the field to discern effective cooling mechanisms that bring a levitated particle to the quantum regime. Due to this, levitated optomechanics is now but one branch of the broader field of levito-dynamics after the common methods of trapping has grown from single beam tweezer traps to ion traps, optical cavities, levitation above superconductors, or some combination of them all. The type of particle that has dominated the literature is a silica sphere, however birefringent vaterite spheres, non-spherical particles such as nanodumbbells, rods, and disks, and magnetic particles have also been explored. With the diversity of traps and types of particles available the applications and proposals are amplifying each year. Some of the current avenues of research involve creating schemes for verifying macroscopic quantum mechanics [35, 150–152], providing platforms for ultrasensitive detection [48, 153], inventing new blueprints for cooling a particle's motion [109, 119, 126], or discovering exotic motions and hidden symmetries in the dynamics governing the particle motion [154, 155]. The methods by which researchers are uncovering these possibilities is vast, but a few can be highlighted such as forcing higher order couplings of the particle to the apparatus to be significant or finding new couplings such as interactions with SQUIDS or atoms [36, 151, 152, 156], creating new potential maps through incident broadband light or metamaterials [157], making use of unexplored regions of common potentials such as utilizing orbital angular momentum [158], and looking at unique entanglements such as with other particles [35, 159] which could bridge the field with quantum information. The recent advancement of one dimensional translational ground state cooling by coherent scattering is only the advent for tests of fundamental physics. The research which follows will build upon our knowledge and will underpin our understanding of that which surrounds us.

## REFERENCES

- [1] Sougato Bose, Anupam Mazumdar, Gavin W. Morley, Hendrik Ulbricht, Marko Toroš, Mauro Paternostro, Andrew A. Geraci, Peter F. Barker, M. S. Kim, and Gerard Milburn. Spin entanglement witness for quantum gravity. *Phys. Rev. Lett.*, 119:240401, Dec 2017.
- [2] C. Marletto and V. Vedral. Gravitationally induced entanglement between two massive particles is sufficient evidence of quantum effects in gravity. *Phys. Rev. Lett.*, 119:240402, Dec 2017.
- [3] Maximilian Schlosshauer. *The quantum-to-classical transition and decoherence*. Springer-Verlag Berlin Heidelberg, 2014.
- [4] Andrea Smirne and Angelo Bassi. Dissipative continuous spontaneous localization (csl) model. *Scientific Reports*, 5(1):12518, 2015.
- [5] K. Jacobs and D. Steck. A straightforward introduction to continuous quantum measurement. *Contemp. Phys.*, 47:279–303, September 2006.
- [6] O. Romero-Isart, A. C. Pflanzer, F. Blaser, R. Kaltenbaek, N. Kiesel, M. Aspelmeyer, and J. I. Cirac. Large quantum superpositions and interference of massive nanometer-sized objects. *Phys. Rev. Lett.*, 107:020405, Jul 2011.
- [7] O. Romero-Isart, A. C. Pflanzer, M. L. Juan, R. Quidant, N. Kiesel, M. Aspelmeyer, and J. I. Cirac. Optically levitating dielectrics in the quantum regime: Theory and protocols. *Phys. Rev. A*, 83:013803, Jan 2011.
- [8] Oriol Romero-Isart, Mathieu L Juan, Romain Quidant, and J Ignacio Cirac. Toward quantum superposition of living organisms. *New J. Phys.*, 12(3):033015, 2010.
- [9] Zhang-qi Yin, Tongcang Li, Xiang Zhang, and L. M. Duan. Large quantum superpositions of a levitated nanodiamond through spin-optomechanical coupling. *Phys. Rev. A*, 88:033614, Sep 2013.
- [10] James Millen and André Xuereb. Perspective on quantum thermodynamics. *New J. Phys.*, 18(1):011002, 2016.
- [11] J. Millen, T. Deesuwana, P. Barker, and J. Anders. Nanoscale temperature measurements using non-equilibrium brownian dynamics of a levitated nanosphere. *Nat. Nanotechnol.*, 9:425, May 2014.
- [12] Dustin Kleckner, Igor Pikovski, Evan Jeffrey, Luuk Ament, Eric Eliel, Jeroen van den Brink, and Dirk Bouwmeester. Creating and verifying a quantum superposition in a micro-optomechanical system. *New J. Phys.*, 10(9):095020, 2008.

- [13] P. H. Kim, C. Doolin, B. D. Hauer, A. J. R. MacDonald, M. R. Freeman, P. E. Barclay, and J. P. Davis. Nanoscale torsional optomechanics. *Appl. Phys. Lett.*, 102(5):053102, 2013.
- [14] Jasper Chan, T. P. Mayer Alegre, Amir H. Safavi-Naeini, Jeff T. Hill, Alex Krause, Simon Gröblacher, Markus Aspelmeyer, and Oskar Painter. Laser cooling of a nanomechanical oscillator into its quantum ground state. *Nature*, 478:89, October 2011.
- [15] Amir H. Safavi-Naeini, Jasper Chan, Jeff T. Hill, Thiago P. Mayer Alegre, Alex Krause, and Oskar Painter. Observation of quantum motion of a nanomechanical resonator. *Phys. Rev. Lett.*, 108:033602, Jan 2012.
- [16] J. Gomis-Bresco, D. Navarro-Urrios, M. Oudich, S. El-Jallal, A. Griol, D. Puerto, E. Chavez, Y. Pennec, B. Djafari-Rouhani, F. Alzina, A. Martínez, and C. M. Sotomayor Torres. A one-dimensional optomechanical crystal with a complete phononic band gap. *Nat. Commun.*, 5:4452, July 2014.
- [17] Shengyan Liu, Tongcang Li, and Zhang qi Yin. Coupling librational and translational motion of a levitated nanoparticle in an optical cavity. *J. Opt. Soc. Am. B*, 34(6):C8–C13, Jun 2017.
- [18] Ryota Omori, Tamiki Kobayashi, and Atsuyuki Suzuki. Observation of a single-beam gradient-force optical trap for dielectric particles in air. *Opt. Lett.*, 22(11):816–818, Jun 1997.
- [19] Tongcang Li, Simon Kheifets, David Medellin, and Mark G. Raizen. Measurement of the instantaneous velocity of a brownian particle. *Science*, 328(5986):1673–1675, 2010.
- [20] P. F. Barker and M. N. Shneider. Cavity cooling of an optically trapped nanoparticle. *Phys. Rev. A*, 81:023826, Feb 2010.
- [21] D. E. Chang, C. A. Regal, S. B. Papp, D. J. Wilson, J. Ye, O. Painter, H. J. Kimble, and P. Zoller. Cavity opto-mechanics using an optically levitated nanosphere. *Proceedings of the National Academy of Sciences*, 107(3):1005–1010, 2010.
- [22] Tongcang Li, Simon Kheifets, and Mark G. Raizen. Millikelvin cooling of an optically trapped microsphere in vacuum. *Nat. Phys.*, 7:527, March 2011.
- [23] Jan Gieseler, Bradley Deutsch, Romain Quidant, and Lukas Novotny. Subkelvin parametric feedback cooling of a laser-trapped nanoparticle. *Phys. Rev. Lett.*, 109:103603, Sep 2012.
- [24] Zhang-qi Yin, Tongcang Li, and M. Feng. Three-dimensional cooling and detection of a nanosphere with a single cavity. *Phys. Rev. A*, 83:013816, Jan 2011.
- [25] Zhang-Qi Yin, Andrew A. Geraci, and Tancang Li. Optomechanics of levitated dielectric particles. *International Journal of Modern Physics B*, 27(26):1330018, 2013.
- [26] James Millen, Tania S Monteiro, Robert Pettit, and A Nick Vamivakas. Optomechanics with levitated particles. *Reports on Progress in Physics*, 83(2):026401, jan 2020.

- [27] Luca Ferialdi, Ashley Setter, Marko Toroš, Chris Timberlake, and Hendrik Ulbricht. Optimal control for feedback cooling in cavityless levitated optomechanics. *New Journal of Physics*, 21(7):073019, jul 2019.
- [28] Felix Tebbenjohanns, Martin Frimmer, Vijay Jain, Dominik Windey, and Lukas Novotny. Motional sideband asymmetry of a nanoparticle optically levitated in free space. *Phys. Rev. Lett.*, 124:013603, Jan 2020.
- [29] Felix Tebbenjohanns, Martin Frimmer, and Lukas Novotny. Optimal position detection of a dipolar scatterer in a focused field. *Phys. Rev. A*, 100:043821, Oct 2019.
- [30] Nadine Meyer, Andrés de los Rios Sommer, Pau Mestres, Jan Gieseler, Vijay Jain, Lukas Novotny, and Romain Quidant. Resolved-sideband cooling of a levitated nanoparticle in the presence of laser phase noise. *Phys. Rev. Lett.*, 123:153601, Oct 2019.
- [31] Uroš Delić, Manuel Reisenbauer, David Grass, Nikolai Kiesel, Vladan Vuletić, and Markus Aspelmeyer. Cavity cooling of a levitated nanosphere by coherent scattering. *Phys. Rev. Lett.*, 122:123602, Mar 2019.
- [32] C. Gonzalez-Ballester, P. Maurer, D. Windey, L. Novotny, R. Reimann, and O. Romero-Isart. Theory for cavity cooling of levitated nanoparticles via coherent scattering: Master equation approach. *Phys. Rev. A*, 100:013805, Jul 2019.
- [33] Dominik Windey, Carlos Gonzalez-Ballester, Patrick Maurer, Lukas Novotny, Oriol Romero-Isart, and René Reimann. Cavity-based 3d cooling of a levitated nanoparticle via coherent scattering. *Phys. Rev. Lett.*, 122:123601, Mar 2019.
- [34] Uroš Delić, Manuel Reisenbauer, Kahan Dare, David Grass, Vladan Vuletić, Nikolai Kiesel, and Markus Aspelmeyer. Cooling of a levitated nanoparticle to the motional quantum ground state. *Science*, 367(6480):892, February 2020.
- [35] C. Gut, K. Winkler, J. Hoelscher-Obermaier, S. G. Hofer, R. Moghadas Nia, N. Walk, A. Steffens, J. Eisert, W. Wieczorek, J. A. Slater, M. Aspelmeyer, and K. Hammerer. Stationary optomechanical entanglement between a mechanical oscillator and its measurement apparatus. *Phys. Rev. Research*, 2:033244, Aug 2020.
- [36] A. Vinante, M. Carlesso, A. Bassi, A. Chiasera, S. Varas, P. Falferi, B. Margesin, R. Mezzena, and H. Ulbricht. Narrowing the parameter space of collapse models with ultracold layered force sensors. *Phys. Rev. Lett.*, 125:100404, Sep 2020.
- [37] Ryan J Marshman, Anupam Mazumdar, Gavin W Morley, Peter F Barker, Steven Hoekstra, and Sougato Bose. Mesoscopic interference for metric and curvature & gravitational wave detection. *New Journal of Physics*, 22(8):083012, aug 2020.
- [38] Gambhir Ranjit, Mark Cunningham, Kirsten Casey, and Andrew A. Geraci. Zeptonewton force sensing with nanospheres in an optical lattice. *Phys. Rev. A*, 93(5), may 2016.

- [39] Thai M. Hoang, Yue Ma, Jonghoon Ahn, Jaehoon Bang, F. Robicheaux, Zhang-Qi Yin, and Tongcang Li. Torsional optomechanics of a levitated nonspherical nanoparticle. *Phys. Rev. Lett.*, 117:123604, Sep 2016.
- [40] T. J. Kippenberg and K. J. Vahala. Cavity optomechanics: Back-action at the mesoscale. *Science*, 321(5893):1172–1176, 2008.
- [41] David Hempston, Jamie Vovrosh, Marko Toroš, George Winstone, Muddassar Rashid, and Hendrik Ulbricht. Force sensing with an optically levitated charged nanoparticle. *Appl. Phys. Lett.*, 111(13):133111, 2017.
- [42] F. Ricci, M. T. Cuairan, G. P. Conangla, A. W. Schell, and R. Quidant. Accurate mass measurement of a levitated nanomechanical resonator for precision force-sensing. *Nano Letters*, 19(10):6711–6715, 2019. PMID: 30888180.
- [43] Markus Aspelmeyer, Tobias J. Kippenberg, and Florian Marquardt. Cavity optomechanics. *Rev. Mod. Phys.*, 86:1391–1452, Dec 2014.
- [44] Levi P. Neukirch and A. Nick Vamivakas. Nano-optomechanics with optically levitated nanoparticles. *Contemp. Phys.*, 56(1):48–62, 2015.
- [45] Zhujing Xu and Tongcang Li. Detecting casimir torque with an optically levitated nanorod. *Phys. Rev. A*, 96:033843, Sep 2017.
- [46] Asimina Arvanitaki and Andrew A. Geraci. Detecting high-frequency gravitational waves with optically levitated sensors. *Phys. Rev. Lett.*, 110:071105, Feb 2013.
- [47] David C. Moore, Alexander D. Rider, and Giorgio Gratta. Search for millicharged particles using optically levitated microspheres. *Phys. Rev. Lett.*, 113:251801, Dec 2014.
- [48] Jonghoon Ahn, Zhujing Xu, Jaehoon Bang, Peng Ju, Xingyu Gao, and Tongcang Li. Ultrasensitive torque detection with an optically levitated nanorotor. *Nature Nanotechnology*, 15(2):89–93, 2020.
- [49] John David Jackson. *Classical electrodynamics*. Wiley, New York, NY, 3rd ed. edition, 1999.
- [50] Olivier J. F. Martin and Nicolas B. Piller. Electromagnetic scattering in polarizable backgrounds. *Phys. Rev. E*, 58:3909–3915, Sep 1998.
- [51] Thomas Wriedt. *Mie Theory: A Review*, pages 53–71. Springer Berlin Heidelberg, Berlin, Heidelberg, 2012.
- [52] D. R. Huffman C. F. Bohren. *Absorption and Scattering of Light by Small Particles*. Wiley, New York, 1983.
- [53] C. F. Bohren and D. R. Huffman. *Particles Small Compared with the Wavelength*, chapter 5, pages 130–157. Wiley-Blackwell, 2007.
- [54] Stefan Kuhn, Alon Kosloff, Benjamin A. Stickler, Fernando Patolsky, Klaus Hornberger, Markus Arndt, and James Millen. Full rotational control of levitated silicon nanorods. *Optica*, 4(3):356–360, Mar 2017.

- [55] Muddassar Rashid, Marko Toroš, Ashley Setter, and Hendrik Ulbricht. Precession motion in levitated optomechanics. *Phys. Rev. Lett.*, 121:253601, Dec 2018.
- [56] Jonghoon Ahn, Zhujing Xu, Jaehoon Bang, Yu-Hao Deng, Thai M. Hoang, Qinkai Han, Ren-Min Ma, and Tongcang Li. Optically levitated nanodumbbell torsion balance and ghz nanomechanical rotor. *Phys. Rev. Lett.*, 121:033603, Jul 2018.
- [57] Bas W. Kwaadgras, Maarten Verdult, Marjolein Dijkstra, and René van Roij. Polarizability and alignment of dielectric nanoparticles in an external electric field: Bowls, dumbbells, and cuboids. *The Journal of Chemical Physics*, 135(13):134105, 2011.
- [58] B. T. Draine. The Discrete-Dipole Approximation and Its Application to Interstellar Graphite Grains. *Astrophysical Journal*, 333:848, October 1988.
- [59] Jan Trojek, Lukáš Chvátal, and Pavel Zemánek. Optical alignment and confinement of an ellipsoidal nanorod in optical tweezers: a theoretical study. *J. Opt. Soc. Am. A*, 29(7):1224–1236, Jul 2012.
- [60] Kishan Dholakia and Pavel Zemánek. Colloquium: Gripped by light: Optical binding. *Rev. Mod. Phys.*, 82:1767–1791, Jun 2010.
- [61] Benjamin A. Stickler, Stefan Nimmrichter, Lukas Martinetz, Stefan Kuhn, Markus Arndt, and Klaus Hornberger. Rotranslational cavity cooling of dielectric rods and disks. *Phys. Rev. A*, 94:033818, Sep 2016.
- [62] D. M. LeVine, R. Meneghini, R. H. Lang, and S. S. Seker. Scattering from arbitrarily oriented dielectric disks in the physical optics regime. *J. Opt. Soc. Am.*, 73(10):1255–1262, Oct 1983.
- [63] R. Schiffer and K. O. Thielheim. Light scattering by dielectric needles and disks. *Journal of Applied Physics*, 50(4):2476–2483, 1979.
- [64] Thomas M. Willis and Herschel Weil. Disk scattering and absorption by an improved computational method. *Appl. Opt.*, 26(18):3987–3995, Sep 1987.
- [65] Roald K. Wangsness. *Electromagnetic Fields*. Wiley.
- [66] Lukas Novotny and Bert Hecht. *Principles of Nano-Optics*. Cambridge University Press, 2006.
- [67] A. Ashkin. Acceleration and trapping of particles by radiation pressure. *Phys. Rev. Lett.*, 24:156–159, Jan 1970.
- [68] Martin Frimmer, Jan Gieseler, and Lukas Novotny. Cooling mechanical oscillators by coherent control. *Phys. Rev. Lett.*, 117:163601, Oct 2016.
- [69] Jamie Vovrosh, Muddassar Rashid, David Hempston, James Bateman, Mauro Paternostro, and Hendrik Ulbricht. Parametric feedback cooling of levitated optomechanics in a parabolic mirror trap. *J. Opt. Soc. Am. B*, 34(7):1421–1428, Jul 2017.
- [70] *Millikelvin cooling of the center-of-mass motion of a levitated nanoparticle*, volume 10347, 2017.

- [71] Nikolai Kiesel, Florian Blaser, Uroš Delić, David Grass, Rainer Kaltenbaek, and Markus Aspelmeyer. Cavity cooling of an optically levitated submicron particle. *Proceedings of the National Academy of Sciences*, 110(35):14180–14185, 2013.
- [72] Simin Feng and Herbert G. Winful. Physical origin of the gouy phase shift. *Opt. Lett.*, 26(8):485–487, Apr 2001.
- [73] Filipp V. Ignatovich, Achim Hartschuh, and Lukas Novotny. Detection of nanoparticles using optical gradient forces. *J. Mod. Opt.*, 50(10):1509–1520, 2003.
- [74] Frederick Gittes and Christoph F. Schmidt. Interference model for back-focal-plane displacement detection in optical tweezers. *Opt. Lett.*, 23(1):7–9, Jan 1998.
- [75] A. T. M. Anishur Rahman, A. C. Frangeskou, P. F. Barker, and G. W. Morley. An analytical model for the detection of levitated nanoparticles in optomechanics. *Rev. Sci. Instrum.*, 89(2):023109, 2018.
- [76] T. Seberson and F. Robicheaux. Parametric feedback cooling of rigid body nanodumbbells in levitated optomechanics. *Phys. Rev. A*, 99:013821, Jan 2019.
- [77] Jaehoon Bang, T. Seberson, Peng Ju, Jonghoon Ahn, Zhujing Xu, Xingyu Gao, F. Robicheaux, and Tongcang Li. Five-dimensional cooling and nonlinear dynamics of an optically levitated nanodumbbell. *Phys. Rev. Research*, 2:043054, Oct 2020.
- [78] J. J. Sakurai. *Modern quantum mechanics*. Addison-Wesley, 2011.
- [79] Jerry B. Marion Stephen T. Thornton. *CHAPTER 11 - Dynamics of Rigid Bodies*. Cengage Learning, 2003.
- [80] Changchun Zhong and F. Robicheaux. Shot-noise-dominant regime for ellipsoidal nanoparticles in a linearly polarized beam. *Phys. Rev. A*, 95:053421, May 2017.
- [81] Benjamin A Stickler, Birthe Papendell, Stefan Kuhn, Björn Schirnski, James Millen, Markus Arndt, and Klaus Hornberger. Probing macroscopic quantum superpositions with nanorotors. *New Journal of Physics*, 20(12):122001, dec 2018.
- [82] A. R. Edmonds. *Angular Momentum in Quantum Mechanics*. Princeton University Press, 2016.
- [83] René Reimann, Michael Doderer, Erik Hebestreit, Rozenn Diehl, Martin Frimmer, Dominik Windey, Felix Tebbenjohanns, and Lukas Novotny. Ghz rotation of an optically trapped nanoparticle in vacuum. *Phys. Rev. Lett.*, 121:033602, Jul 2018.
- [84] Yoshihiko Arita, Michael Mazilu, and Kishan Dholakia. Laser-induced rotation and cooling of a trapped microgyroscope in vacuum. *Nat. Commun.*, 4:2374, August 2013.
- [85] Paul S. Epstein. On the resistance experienced by spheres in their motion through gases. *Phys. Rev.*, 23:710–733, Jun 1924.

- [86] Tongcang Li and Mark G. Raizen. Brownian motion at short time scales. *Annalen der Physik*, 525(4):281–295, 2013.
- [87] Don S. Lemons and Anthony Gythiel. Paul langevin’s 1908 paper “on the theory of brownian motion” [“sur la théorie du mouvement brownien,” c. r. acad. sci. (paris) 146, 530–533 (1908)]. *Am. J. Phys*, 65(11):1079–1081, 1997.
- [88] L. Cohen. A review of brownian motion based solely on the langevin equation with white noise. In Tao Qian and Luigi G. Rodino, editors, *Mathematical Analysis, Probability and Applications – Plenary Lectures*, pages 1–35, Cham, 2016. Springer International Publishing.
- [89] S. A. Beresnev, V. G. Chernyak, and G. A. Fomyagin. Motion of a spherical particle in a rarefied gas. part 2. drag and thermal polarization. *Journal of Fluid Mechanics*, 219:405–421, 1990.
- [90] James Corson, George W. Mulholland, and Michael R. Zachariah. Calculating the rotational friction coefficient of fractal aerosol particles in the transition regime using extended kirkwood-riseman theory. *Phys. Rev. E*, 96:013110, Jul 2017.
- [91] Felix Tebbenjohanns, Martin Frimmer, Andrei Militaru, Vijay Jain, and Lukas Novotny. Cold damping of an optically levitated nanoparticle to microkelvin temperatures. *Phys. Rev. Lett.*, 122:223601, Jun 2019.
- [92] T. Seberson and F. Robicheaux. Distribution of laser shot-noise energy delivered to a levitated nanoparticle. *Phys. Rev. A*, 102:033505, Sep 2020.
- [93] Wayne M. Itano and D. J. Wineland. Laser cooling of ions stored in harmonic and penning traps. *Phys. Rev. A*, 25:35–54, Jan 1982.
- [94] Vijay Jain, Jan Gieseler, Clemens Moritz, Christoph Dellago, Romain Quidant, and Lukas Novotny. Direct measurement of photon recoil from a levitated nanoparticle. *Phys. Rev. Lett.*, 116:243601, Jun 2016.
- [95] B. Rodenburg, L. P. Neukirch, A. N. Vamivakas, and M. Bhattacharya. Quantum model of cooling and force sensing with an optically trapped nanoparticle. *Optica*, 3(3):318–323, Mar 2016.
- [96] A. Pontin, N. P. Bullier, M. Toroš, and P. F. Barker. Ultranarrow-linewidth levitated nano-oscillator for testing dissipative wave-function collapse. *Phys. Rev. Research*, 2:023349, Jun 2020.
- [97] B. Richards, E. Wolf, and Dennis Gabor. Electromagnetic diffraction in optical systems, ii. structure of the image field in an aplanatic system. *Proceedings of the Royal Society of London. Series A. Mathematical and Physical Sciences*, 253(1274):358–379, 1959.
- [98] Anika C. Pflanzner, Oriol Romero-Isart, and J. Ignacio Cirac. Master-equation approach to optomechanics with arbitrary dielectrics. *Phys. Rev. A*, 86:013802, Jul 2012.
- [99] Changchun Zhong and F. Robicheaux. Decoherence of rotational degrees of freedom. *Phys. Rev. A*, 94:052109, Nov 2016.

- [100] P. A. Maia Neto and H. M Nussenzveig. Theory of optical tweezers. *Europhysics Letters (EPL)*, 50(5):702–708, jun 2000.
- [101] Bruce T. Draine and Piotr J. Flatau. Discrete-dipole approximation for scattering calculations. *J. Opt. Soc. Am. A*, 11(4):1491–1499, Apr 1994.
- [102] Fons van der Laan, René Reimann, Andrei Militaru, Felix Tebbenjohanns, Dominik Windey, Martin Frimmer, and Lukas Novotny. Optically levitated rotor at its thermal limit of frequency stability. *Phys. Rev. A*, 102:013505, Jul 2020.
- [103] Yoshihiko Arita, Ewan M. Wright, and Kishan Dholakia. Optical binding of two cooled micro-gyroscopes levitated in vacuum. *Optica*, 5(8):910–917, Aug 2018.
- [104] Li Ge and Nan Zhao. Torsional cooling of a nanodiamond via the interaction with the electron spin of the embedded nitrogen-vacancy center. *Phys. Rev. A*, 98:043415, Oct 2018.
- [105] Gambhir Ranjit, Cris Montoya, and Andrew A. Geraci. Cold atoms as a coolant for levitated optomechanical systems. *Phys. Rev. A*, 91:013416, Jan 2015.
- [106] Daniel Goldwater, Benjamin A Stickler, Lukas Martinetz, Tracy E Northup, Klaus Hornberger, and James Millen. Levitated electromechanics: all-electrical cooling of charged nano- and micro-particles. *Quantum Science and Technology*, 4(2):024003, jan 2019.
- [107] Alexander D. Rider, Charles P. Blakemore, Akio Kawasaki, Nadav Priel, Sandip Roy, and Giorgio Gratta. Electrically driven, optically levitated microscopic rotors. *Phys. Rev. A*, 99:041802, Apr 2019.
- [108] Chris Timberlake, Marko Toroš, David Hempston, George Winstone, Mudassar Rashid, and Hendrik Ulbricht. Static force characterization with fano anti-resonance in levitated optomechanics. *Appl. Phys. Lett.*, 114(2):023104, 2019.
- [109] M. Iwasaki, T. Yotsuya, T. Naruki, Y. Matsuda, M. Yoneda, and K. Aikawa. Electric feedback cooling of single charged nanoparticles in an optical trap. *Phys. Rev. A*, 99:051401, May 2019.
- [110] Gerard P. Conangla, Francesco Ricci, Marc T. Cuairan, Andreas W. Schell, Nadine Meyer, and Romain Quidant. Optimal feedback cooling of a charged levitated nanoparticle with adaptive control. *Phys. Rev. Lett.*, 122:223602, Jun 2019.
- [111] Jen-Feng Hsu, Peng Ji, Charles W. Lewandowski, and Brian D’Urso. Cooling the motion of diamond nanocrystals in a magneto-gravitational trap in high vacuum. *Sci. Rep.*, 6:30125, July 2016.
- [112] C. C. Rusconi, V. Pöschhacker, K. Kustura, J. I. Cirac, and O. Romero-Isart. Quantum spin stabilized magnetic levitation. *Phys. Rev. Lett.*, 119:167202, Oct 2017.
- [113] Xufeng Zhang, Chang-Ling Zou, Liang Jiang, and Hong X. Tang. Cavity magnomechanics. *Science Advances*, 2(3), 2016.

- [114] Carlos Gonzalez-Ballester, Jan Gieseler, and Oriol Romero-Isart. Quantum acoustomechanics with a micromagnet. *Phys. Rev. Lett.*, 124:093602, Mar 2020.
- [115] Tao Wang, Sean Lourette, Sean R. O’Kelley, Metin Kayci, Y.B. Band, Derek F. Jackson Kimball, Alexander O. Sushkov, and Dmitry Budker. Dynamics of a ferromagnetic particle levitated over a superconductor. *Phys. Rev. Applied*, 11:044041, Apr 2019.
- [116] J Druge, C Jean, O Laurent, M-A Méasson, and I Favero. Damping and non-linearity of a levitating magnet in rotation above a superconductor. *New Journal of Physics*, 16(7):075011, jul 2014.
- [117] J Hofer and M Aspelmeyer. Analytic solutions to the maxwell–london equations and levitation force for a superconducting sphere in a quadrupole field. *Physica Scripta*, 94(12):125508, oct 2019.
- [118] T. Seberson and F. Robicheaux. Stability and dynamics of optically levitated dielectric disks in a gaussian standing wave beyond the harmonic approximation. *Phys. Rev. Research*, 2:033437, Sep 2020.
- [119] T. Seberson, Peng Ju, Jonghoon Ahn, Jaehoon Bang, Tongchang Li, and F. Robicheaux. Simulation of sympathetic cooling an optically levitated magnetic nanoparticle via coupling to a cold atomic gas. *J. Opt. Soc. Am. B*, 37(12):3714–3720, Dec 2020.
- [120] Vijay Jain. *Levitated optomechanics at the photon recoil limit*. PhD thesis, ETH Zurich, 2017.
- [121] C. Zhong, T. Li, and F. Robicheaux. Quantum calculation of feedback cooling a laser levitated nanoparticle in the shot-noise-dominant regime. *ArXiv e-prints*, August 2017.
- [122] Vijay Jain, Felix Tebbenjohanns, and Lukas Novotny. Microkelvin control of an optically levitated nanoparticle. In *Frontiers in Optics 2016*, page FF5B.2. Optical Society of America, 2016.
- [123] Stefan Kuhn, Benjamin A. Stickler, Alon Kosloff, Fernando Patolsky, Klaus Hornberger, Markus Arndt, and James Millen. Optically driven ultra-stable nanomechanical rotor. *Nature Communications*, 8(1):1670, November 2017.
- [124] Tongchang Li, Jonghoon Ahn, Zhujing Xu, and Jaehoon Bang. Optically levitated torque sensor and ultrafast nanomechanical rotor. In *Conference on Lasers and Electro-Optics*, page JF3B.3. Optical Society of America, 2018.
- [125] William H. Press, Saul A. Teukolsky, William T. Vetterling, and Brian P. Flannery. *Numerical Recipes 3rd Edition: The Art of Scientific Computing*. Cambridge University Press, New York, NY, USA, 3 edition, 2007.
- [126] T. Delord, P. Huillery, L. Nicolas, and G. Hétet. Spin-cooling of the motion of a trapped diamond. *Nature*, 580(7801):56–59, 2020.
- [127] Philipp Christoph, Tobias Wagner, Hai Zhong, Roland Wiesendanger, Klaus Sengstock, Alexander Schwarz, and Christoph Becker. Combined feedback and sympathetic cooling of a mechanical oscillator coupled to ultracold atoms. *New Journal of Physics*, 20(9):093020, sep 2018.

- [128] Andreas Jöckel, Aline Faber, Tobias Kampschulte, Maria Korppi, Matthew T. Rakher, and Philipp Treutlein. Sympathetic cooling of a membrane oscillator in a hybrid mechanical-atomic system. *Nature Nanotechnology*, 10(1):55–59, January 2015.
- [129] Stephan Camerer, Maria Korppi, Andreas Jöckel, David Hunger, Theodor W. Hänsch, and Philipp Treutlein. Realization of an optomechanical interface between ultracold atoms and a membrane. *Phys. Rev. Lett.*, 107:223001, Nov 2011.
- [130] B. Vogell, K. Stannigel, P. Zoller, K. Hammerer, M. T. Rakher, M. Korppi, A. Jöckel, and P. Treutlein. Cavity-enhanced long-distance coupling of an atomic ensemble to a micromechanical membrane. *Phys. Rev. A*, 87:023816, Feb 2013.
- [131] C. J. Foot. *Atomic physics*. Oxford University Press, Oxford :, reprinted edition, 2011.
- [132] K. L. Corwin, S. J. M. Kuppens, D. Cho, and C. E. Wieman. Spin-polarized atoms in a circularly polarized optical dipole trap. *Phys. Rev. Lett.*, 83:1311–1314, Aug 1999.
- [133] Rudolf Grimm, Matthias Weidemüller, and Yurii B. Ovchinnikov. Optical dipole traps for neutral atoms. volume 42 of *Advances In Atomic, Molecular, and Optical Physics*, pages 95 – 170. Academic Press, 2000.
- [134] Piet O. Schmidt, Sven Hensler, Jörg Werner, Thomas Binhammer, Axel Görlitz, and Tilman Pfau. Doppler cooling of an optically dense cloud of magnetically trapped atoms. *J. Opt. Soc. Am. B*, 20(5):960–967, May 2003.
- [135] Y. Castin, H. Wallis, and J. Dalibard. Limit of doppler cooling. *J. Opt. Soc. Am. B*, 6(11):2046–2057, Nov 1989.
- [136] S. H. Wemple, S. L. Blank, J. A. Seman, and W. A. Biolsi. Optical properties of epitaxial iron garnet thin films. *Phys. Rev. B*, 9:2134–2144, Mar 1974.
- [137] Makiyyu Abdullahi Musa, Raba’ah Syahidah Azis, Nurul Huda Osman, Jumiah Hassan, and Tasiu Zangina. Structural and magnetic properties of yttrium iron garnet (yig) and yttrium aluminum iron garnet (yalg) nanoferrite via sol-gel synthesis. *Results in Physics*, 7:1135 – 1142, 2017.
- [138] Vinay Sharma, Jitendra Saha, Satyabrata Patnaik, and Bijoy K. Kuanr. Synthesis and characterization of yttrium iron garnet (yig) nanoparticles - microwave material. *AIP Advances*, 7(5):056405, 2017.
- [139] A. Griesmaier, J. Stuhler, and T. Pfau. Production of a chromium bose–einstein condensate. *Appl. Phys. B*, 82(2):211–216, Feb 2006.
- [140] Mingwu Lu, Seo Ho Youn, and Benjamin L. Lev. Spectroscopy of a narrow-line laser-cooling transition in atomic dysprosium. *Phys. Rev. A*, 83:012510, Jan 2011.
- [141] L. Gabardos, S. Lepoutre, O. Gorceix, L. Vernac, and B. Laburthe-Tolra. Cooling all external degrees of freedom of optically trapped chromium atoms using gray molasses. *Phys. Rev. A*, 99:023607, Feb 2019.

- [142] Mingwu Lu, Nathaniel Q. Burdick, Seo Ho Youn, and Benjamin L. Lev. Strongly dipolar bose-einstein condensate of dysprosium. *Phys. Rev. Lett.*, 107:190401, Oct 2011.
- [143] Fernando Monteiro, Wenqiang Li, Gadi Afek, Chang-ling Li, Michael Mossman, and David C. Moore. Force and acceleration sensing with optically levitated nanogram masses at microkelvin temperatures. *Phys. Rev. A*, 101:053835, May 2020.
- [144] D E Chang, K-K Ni, O Painter, and H J Kimble. Ultrahigh-qmechanical oscillators through optical trapping. *New Journal of Physics*, 14(4):045002, apr 2012.
- [145] Zhengdong Cheng, Thomas G. Mason, and P. M. Chaikin. Periodic oscillation of a colloidal disk near a wall in an optical trap. *Phys. Rev. E*, 68:051404, Nov 2003.
- [146] Z. Cheng, P. M. Chaikin, and T. G. Mason. Light streak tracking of optically trapped thin microdisks. *Phys. Rev. Lett.*, 89:108303, Aug 2002.
- [147] J. Robert Johansson, Neill Lambert, Imran Mahboob, Hiroshi Yamaguchi, and Franco Nori. Entangled-state generation and bell inequality violations in nanomechanical resonators. *Phys. Rev. B*, 90:174307, Nov 2014.
- [148] K. Stannigel, P. Komar, S. J. M. Habraken, S. D. Bennett, M. D. Lukin, P. Zoller, and P. Rabl. Optomechanical quantum information processing with photons and phonons. *Phys. Rev. Lett.*, 109:013603, Jul 2012.
- [149] Alejandro Grine, Darwin Serkland, Michael Wood, and Justin Schultz. Private communication, August 2020.
- [150] Huiping Zhan, Gaoxiang Li, and Huatang Tan. Preparing macroscopic mechanical quantum superpositions via photon detection. *Phys. Rev. A*, 101:063834, Jun 2020.
- [151] M. Toroš, S. Bose, and P. F. Barker. Atom-nanoparticle schrödinger cats, 2020.
- [152] A. Hopper and P. F. Barker. A hybrid quantum system formed by trapping atoms in the near-field of a levitated nanosphere, 2020.
- [153] Chris Timberlake, Giulio Gasbarri, Andrea Vinante, Ashley Setter, and Hendrik Ulbricht. Acceleration sensing with magnetically levitated oscillators above a superconductor. *Applied Physics Letters*, 115(22):224101, 2019.
- [154] Yi Huang, Qihao Guo, Anda Xiong, Tongcang Li, and Zhang-qi Yin. Classical and quantum time crystals in a levitated nanoparticle without drive. *Phys. Rev. A*, 102:023113, Aug 2020.
- [155] Yue Ma, Kiran E. Khosla, Benjamin A. Stickler, and M. S. Kim. Quantum persistent tennis racket dynamics of nanorotors. *Phys. Rev. Lett.*, 125:053604, Jul 2020.
- [156] Uroš Delić, David Grass, Manuel Reisenbauer, Tobias Damm, Martin Weitz, Nikolai Kiesel, and Markus Aspelmeyer. Levitated cavity optomechanics in high vacuum. *Quantum Science and Technology*, 5(2):025006, mar 2020.

- [157] A. T. M. Anishur Rahman and P. F. Barker. Optical levitation using broadband light. *Optica*, 7(8):906–912, Aug 2020.
- [158] Filip Kiałka, Benjamin A. Stickler, and Klaus Hornberger. Orbital angular momentum interference of trapped matter waves. *Phys. Rev. Research*, 2:022030, May 2020.
- [159] Henning Rudolph, Klaus Hornberger, and Benjamin A. Stickler. Entangling levitated nanoparticles by coherent scattering. *Phys. Rev. A*, 101:011804, Jan 2020.

## PUBLICATIONS

**T. Seberson** and F. Robicheaux, Parametric feedback cooling of rigid body nanodumbbells in levitated optomechanics, *Physical Review A*, **99**, 013821 - Published 14 January 2019

**T. Seberson** and F. Robicheaux, Distribution of laser shot-noise energy delivered to a levitated nanoparticle, *Physical Review A*, **102**, 033505 - Published 8 September 2020

**T. Seberson** and F. Robicheaux, Stability and dynamics of optically levitated dielectric disks in a Gaussian standing wave beyond the harmonic approximation, *Physical Review Research*, **2**, 033437 - Published 17 September 2020

Jaehoon Bang, **T. Seberson**, Peng Ju, Jonghoon Ahn, Zhujing Xu, Xingyu Gao, F. Robicheaux, and Tongcang Li, Five-dimensional cooling and nonlinear dynamics of an optically levitated nanodumbbell, *Physical Review Research*, **2**, 043054 - Published 9 October 2020

**T. Seberson**, Peng Ju, Jaehoon Bang, Jonghoon Ahn, Tongcang Li, and F. Robicheaux, Simulation of sympathetic cooling an optically levitated magnetic nanoparticle via coupling to a cold atomic gas, *Journal of the Optical Society of America B*, **37**, 3714-3720 - Published 9 November 2020